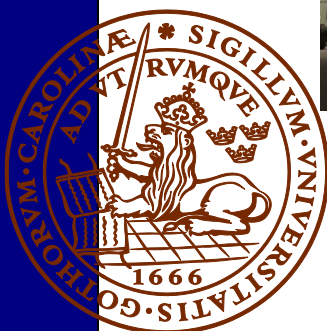


# Feasibility of Enhanced Geothermal Systems in the Precambrian crystalline basement in SW Scania, Sweden

***Hanna Kervall***

Dissertations in Geology at Lund University,  
Master's thesis, no 628  
(45 hp/ECTS credits)

---



Department of Geology  
Lund University  
2021



# **Feasibility of Enhanced Geothermal Systems in the Precam- brian crystalline basement in SW Scania, Sweden**

Master's thesis  
Hanna Kervall

Department of Geology  
Lund University  
2021

# Table of contents

<b>1 Introduction .....</b>	<b>7</b>
1.2 What is EGS?	7
1.3 Geological setting of SW Scania	9
<b>2 Data base.....</b>	<b>11</b>
2.1 Outcrops and cores from the Dalby quarry	11
2.2 The FFC-1 borehole (55.6°N 13.0°E)	13
2.2.1 Drilling operation of FFC-1	13
2.2.2 Geological well site work during drilling of FFC-1	14
<b>3 Methods .....</b>	<b>16</b>
3.1 Visual examination of cores	17
3.1.2 Microscopy	17
3.1.3 SEM-EDX	17
3.2 Thermal analysis	18
3.2.1 Dalby	18
3.2.2 FFC-1	18
3.3 Chemical analysis	18
3.3.1 FFC-1	18
<b>4 Results.....</b>	<b>18</b>
4.1 Dalby	18
4.1.1 Felsic granitoid rocks	18
4.1.2 Mafic rocks	24
4.2 FFC-1	30
4.2.1 Felsic granitoid rocks	30
4.2.2 Mafic rocks	35
<b>5 Discussion .....</b>	<b>39</b>
5.1 Bedrock composition	39
5.1.1 Minerology	39
5.1.2 Textures and bearing on strength	40
5.2 Fracturing	42
5.2.1 Interpretation and estimated ability to respond to EGS-stimulation	43
5.3 Stresses	44
5.4 Thermal properties	45
5.4.1 Geothermal gradient	45
5.4.2 Thermal conductivity and density	47
5.5 Assessment of a one cubic kilometre rock block at 6 km depth in SW Scania	48
<b>6 Conclusions.....</b>	<b>48</b>
<b>7 Acknowledgements .....</b>	<b>49</b>
<b>8 References.....</b>	<b>49</b>

# Feasibility of Enhanced Geothermal Systems in the Precambrian crystalline basement in SW Scania, Sweden

HANNA KERVALL

Kervall, H., 2021: Feasibility of Enhanced Geothermal Systems in the Precambrian crystalline basement in SW Scania, Sweden. *Dissertations in Geology at Lund University*, No. 628, 53 pp. 45 hp (45 ECTS credits)

**Abstract:** The ability to evaluate the geothermal potential at a depth of five to six kilometres in the crystalline bedrock is crucial for the EGS-technology to be utilized in the future. This work focuses primarily on presenting expected geological conditions at great depths in southwestern Scania. The study is based on information from E.ON's deep drilling FFC-1 in Malmö and data and investigations of the crystalline bedrock at Romeleåsen and in the Dalby Quarry. The work presents qualitative and quantitative analyses from optical microscopy, SEM-EDX analysis, chemical analyses, density measurements and analyses of the thermal properties of the bedrock. Geophysical information from borehole logging has been used to assess rock type distribution in the rock mass. The survey shows that the bedrock in FFC-1 is mineralogically and chemically comparable to the bedrock on Romeleåsen. Gneiss of different colors and with varying foliation and quartz content make up approx. 80% of the rock mass. The rest is dominated by mafic rocks such as amphibolite and metabasite. Mineralogy shows that the bedrock in FFC-1 was metamorphosed under amphibolite facies conditions, which is evident in a relative higher frequency of garnet in comparison with the bedrock in Dalby. The two dominated rock types show clear differences in density (2.67 respectively 2.98 g/cm<sup>3</sup>) and thermal conductivity (3.62 respectively 2.57 W/m K), which gives very different geothermal conditions. The bedrock is similar to Romeleåsen, strongly fractured with different types of fractures, open and closed and presenting corresponding fractures fillings. The predicted elevated fracture frequency of the FFC-1 bedrock at greater depths is explained by pressure relief that created horizontal fractures, and tectonics related to the Tornquist zone. The tectonics and metamorphic history of the Fennoscandian Border Zone also indicates a high prevalence of latent fracture systems with good prospects for hydrostatic stimulation and EGS.

**Keywords:** EGS, deep drilling, geothermal, petrology, petrophysical properties, Sveconorwegian

**Supervisor(s):** Mikael Erlström (Geological Survey of Sweden), Ulf Söderlund (Department of Geology, LU)

**Subject:** Bedrock Geology

*Hanna Kervall, Department of Geology, Lund University, Sölvegatan 12, SE-223 62 Lund, Sweden. E-mail: HannaKervall@hotmail.com*

# Genomförbarhet av Enhanced Geothermal Systems i den prekambrika kristallina berggrunden i sydvästra Skåne, Sverige

HANNA KERVALL

Kervall, H., 2021: Genomförbarhet av Enhanced Geothermal Systems i den prekambrika kristallina berggrunden i sydvästra Skåne, Sverige. *Examensarbeten i geologi vid Lunds universitet*, Nr. 628, 53 sid. 45 hp.

**Sammanfattning:** Att kunna bedöma den geotermiska potentialen på fem till sex kilometers djup i den kristallina berggrunden är avgörande för att EGS-tekniken ("Enhanced Geothermal Systems") ska kunna bli möjlig i framtiden. Det här arbetet fokuserar i första hand på att presentera förväntade berggrundsförhållanden på stora djup i sydvästra Skåne. Studien baseras på information från E.ONs djupborrning FFC-1 i Malmö och data och undersökningar av den kristallina berggrunden på Romeleåsen och i Dalby stenbrott. I arbetet presenteras kvalitativa och kvantitativa analyser från optisk mikroskopering, SEM-EDX-analys, kemiska analyser-, densitetsmätningar och analyser av berggrundens termiska egenskaper. Geofysisk information från borrhålsloggningar i FFC-1 har använts för bedömning av bergartsfördelningen i bergmassan. Undersökningen visar att berggrunden i FFC-1 är mineralogiskt och kemiskt jämförbar Romeleåsens. Gnejs med olika färg och med varierande foliation och kvartshalt utgör ca. 80% av bergmassan. Övrig andel domineras av mafiska bergarter såsom amfibolit och metabasit. Mineralogin visar att berggrunden i FFC-1 metamorfoserats under amfibolitfacies-förhållanden vilket visar sig i en relativt större förekomst av granater i jämförelse med berggrunden i Dalby. De två dominerade bergartsklasserna uppvisar tydliga skillnader i densitet (2,67 och 2,98 g/cm<sup>3</sup>) och termisk ledningsförmåga (3,62 och 2,57 W/m K) vilket ger mycket olika geotermiska förutsättningar. Berggrunden är, likt Romeleåsens, kraftigt uppsprucken med flera typer av sprickbildningar, öppna, och slutna och uppvisar överensstämmande sprickfyllningar. FFC-1:s berggrundens pre-dikerade förhöjda sprickfrekvens på större djup förklaras med tryckavlastning som skapat horisontella sprickor, samt tektonik relaterad till Tornquistzonen. Fennoskandiska Randzonens tektoniska och metamorfa historia indikerar även en hög förekomst av latent spricksystem med goda utsikter för hydrostatisk stimulering och EGS.

**Nyckelord:** EGS, djupborrning, geotermi, petrofysiska egenskaper, petrologi, Sveconorwegisk berggrund

**Handledare:** Mikael Erlström (Sveriges Geologiska Undersökning), Ulf Söderlund (Geologiska Institutionen, LU)

**Ämnesinriktning:** Berggrundsgeologi

*Hanna Kervall, Geologiska institutionen, Lunds Universitet, Sölvegatan 12, 223 62 Lund, Sverige. E-post: Hanna.Kervall@hotmail.com*

# 1 Introduction

An increasing demand for eco-friendly energy alternatives and new opportunities for Enhanced Geothermal Systems (EGS) have set the scene for many countries to start evaluating their geothermal resources. Sweden aims to be carbon neutral by 2045 (Statens Offentliga Utredningar 2020) and an annually expansion of 100 TWh renewable energy is forecasted by the Energy Agency until the year 2040 (Energimyndigheten 2018). EGS do not only meet these environmental requirements; they also fulfil the Swedish ambitions of reliability, near-by placement and small areal footprint (Energimyndigheten 2018; U.S. Department of Energy n.d.-a; from now on U.S. DOE). Furthermore Vattenfall, which is the largest power company in Sweden, has decided to phase out coal power from their portfolio by 2030, which further opens up for renewable alternatives such as EGS and overall accelerates the geoenery market in Sweden (Vattenfall 2020).

The sedimentary bedrock in SW Scania with several potential geothermal sandstone aquifers have been noticed in geothermal contexts since the 1970:s (Rosberg and Erlström 2019). Between 1983 and 1985, the geothermal potential outside Lund was investigated by the Faculty of Engineering (LTH, Lund University) and Lund Energy company. Their investigations resulted in the installation of a geothermal system where c. 22 °C warm water from the Cretaceous sandstone at 400–800 m depth is utilized via heat exchange in heat pumps for the Lund district heating system (Alm 1999; Aldenius 2017). Until recently the system has provided c. 25% of the heat to the district heating. Thus, the system has been running for more than 35 years but is now gradually faced out as the well integrity is failing and the temperature of the formation has decreased to 16 °C.

In 2000 an interest rose in exploring the possibilities to utilize potential resources of hot water at great depths in the fractured crystalline bedrock in the Romeleåsen Fault Zone. A 3701.8-m-deep exploration well, DGE-1, was in 2002–2003 drilled outside Lund, in connection to the Romeleåsen Fault Zone, entering the crystalline basement at 1946 m (Rosberg and Erlström 2019). This well gave a bottomhole temperature of 85.1 °C, which illustrated a relatively high temperature gradient in the crystalline basement of 22 °C/km (Rosberg and Erlström 2019). It was, however, found that the water productivity from the fractured rock mass was insufficient for building a full-scale geothermal plant (Wirtén 2016).

More or less simultaneously with the Lund project Sydkraft AB (now E.ON), drilled two wells (FFC-1 and FFC-2) in Malmö north harbour. The two wells reach the top of the basement at c. 2100 m. The initial target for these wells was the geothermal potential in the Mesozoic sandstone beds between 1600 and c. 2100 m depth. This project was, however, put on hold due to competition from other energy resources to the district heat in Malmö, primarily by surplus heat from a large waste incineration plant.

Later, in 2016 rejuvenated interest for investigating the potential of deep geothermal energy in Malmö rose at E.ON. This was primarily driven by the energy company St1's deep geothermal EGS project in Finland. E.ON's feasibility studies resulted in a deci-

sion to extend the existing vertical FFC-1 well in Malmö into the Precambrian crystalline basement. The aim was to reach at least one kilometre into the basement as to get reliable data on the thermal and physical properties. An optimal target was to reach four kilometres depth. The drilling started in June and the final depth reached was 3133 m in August 2020.

Overall, the geological assessment for an EGS is a challenging task as it concerns predictions of the composition of the bedrock at great depths. In order to forecast and model the design there is a need of information regarding the composition of the bedrock and it's thermal properties, rock stresses, degree of fracturing and hydraulic conditions. Today there are very few boreholes to greater depths than c. 1 km that give this information for the crystalline basement in the Fennoscandian Shield. Thus, the deep drilling in Malmö provides unique information on several of these important properties.

This master project aims to characterize the crystalline bedrock beneath Malmö, primarily based on geological data from the FFC-1 borehole. Furthermore, these results will be compared with a study on cores and outcrops from the Dalby quarry on the Romeleåsen horst as well as information from regional geological bedrock maps from the Geological Survey of Sweden and the DGE-1 deep drilling outside Lund. The study focuses mainly on characteristics that are important for assessing the EGS potential in southwestern Sweden and Scania such as main rock types, thermal properties, chemical composition, relative rock distribution, fracturing and fracture minerals.

The scope of the study had to be somewhat modified during the course of this project due to the Covid-19 pandemic and that E.ON paused the FFC-1 project. This led to that some of the planned E.ON surveys were not performed, i.e. coring and seismic survey. Therefore the study on the Dalby samples achieved a greater focus than originally planned. The following objectives have been investigated:

1. the overall physical properties of the rocks have been assessed using geophysical logs such as Spectral gamma ray, density, Sonic and Caliper from the FFC-1 well,
2. based on investigations using optical microscopy and SEM-EDS-analysis on thin sections the rock type, mineral composition, fractures and fracture fillings have been described,
3. for the different main rock types the chemical composition, density and thermal properties have been evaluated.

## 1.2 What is EGS?

EGS is an umbrella term used for artificially made reservoirs in tight or low permeable rocks, designed for district heating or electricity production. Conventional geothermal systems have been in use since the early 20th century, but the high demands placed on the geological conditions have limited the use to areas with sedimentary cover strata holding porous and permeable aquifers (Austin 1977; Breede et al. 2013). Already in 1940, experiments began with artificially

manipulating the bedrock conditions to open up relatively tight reservoirs. The oil- and gas industry introduced hydro-fracking as a method to artificially create fracture systems and thereby enabled larger withdrawals from the reservoir (Potter et al. 1974; Baker Hughes 2012).

Further development of the EGS-technology has now been going on for almost 50 years. The shearing method, which is applied on naturally fractured bedrock, has taken on a significant role since the 1980: s (MIT 2006; Jung 2013). The aim of both fracking and shearing is to artificially increase the permeability of the rock by letting the rock's compressive stress being exceeded by stress created by a hydrostatic pressure in the borehole surroundings. Fracking is applied to low- to impermeable rocks, with the aim of creating new fracture systems, enabled by exposure to a fast increased stress (MIT 2006; Dusseault 2016). During shearing the procedure is slow. Shearing is applied to medium/high permeable rock, under which pre-existing fractures tends to shear, i.e., open up more. The shearing method further distinguish by not requiring any chemicals and by the fractures being self-supported (Dusseault 2016; MIT 2006). Companies often uses different approaches in the creation of EGS reservoirs, this mainly applies to the choice of drilling technology, surveys and modeling programs. The basics, however, can be summarized in three phases (U.S. DOE 2016):

- 1) the bedrock system is characterized through different surveys, such as seismic mapping and test boreholes,
- 2) the reservoir is created i.e., production- and injection wells are drilled and stimulation of the bedrock is performed,
- 3) the maintenance of the reservoir and the operation of the production facility/power plant.

A typical EGS-system is illustrated in figure 1. This includes one injection and at least one production well. The wells are often also deviated as to get an optimal length contact with the created reservoir. A submersible pump is installed in the production well and the produced warm water is circulated via a heat exchange facility on the ground and back into the injection well. The water used can be both fluids from the bedrock but often in originally tight rocks this is fresh water added to the system. For electricity production a minimum temperature of c. 150°C in the production well is required (MIT 2006). For district heating, a temperature of 100°C in the production well is sufficient. However, an optimal direct connection to a district heat system requires temperatures between 115–120°C (MIT 2006; M. Erlström, personal communication, 2021).

In recent times research has begun into applying the EGS-technology at greater depths through deeper drilling, as this would significantly expand the field of application of the technology into other geological settings than the strict hotter parts of our planet. In this context, areas with relatively cold crystalline bedrock have become of interest, especially if it con-

nects to naturally fractured systems, such as batholiths, impact- or fault structures. Even greater potential is believed to be found in areas where the crystalline basement is concealed beneath thick layers of sedimentary bedrocks with relatively low thermal conductivity, thus isolating properties. This type of relationship is for instance found in the bedrock in southwestern Sweden.

Today there are no EGS plants in Scandinavia in operation since the EGS potential in Europe has so far focused on relatively hot areas for electricity production. The deepest of these are the Soultz-sous-Forêts, (c. 5000 m) and Rittershoffen (3196 m) in France and Insheim (3600 m) in Germany, all located in fractured granite (MIT 2006; Pfalzwerke 2019; Destress 2020). Since May 2012 there is also a two year-long EGS-project in progress in Cornwall County in south-western England (Eden geothermal 2021). The project aims to utilize the heat of the St Austell granite, part of a batholithic granite complex, to initially supply the Eden's Biomes with district heat. In a second step a 4.5 km deep well will be drilled to create a reservoir connected to a power plant. The aim is to provide Eden with renewable energy enough to make the area carbon-climate positive by 2023 (EGS Energy 2021).

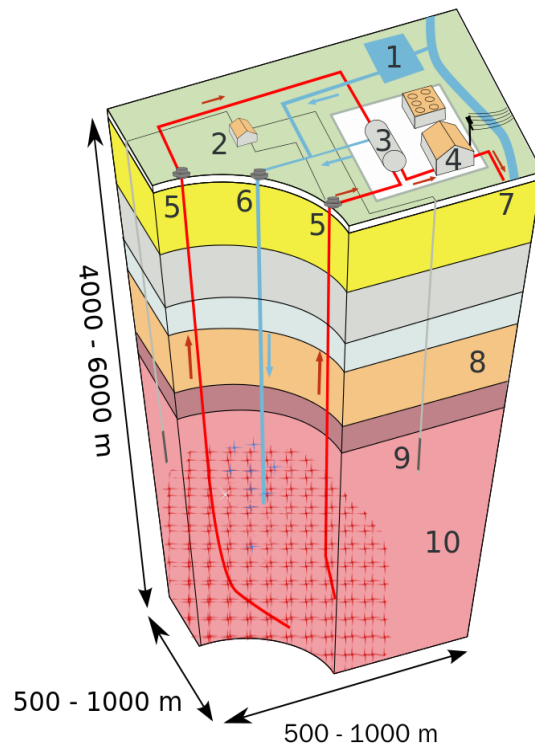


Fig. 1. Schematic illustration of an Enhanced Geothermal System: 1 reservoir, 2 pump house, 3 heat exchanger, 4 turbine hall, 5 production well, 6 injection well, 7 hot water to district heating, 8 porous sediments, 9 observation well, 10 crystalline bedrock. Figure modified from Wikimedia (2009), press content from Siemens, CC BY-SA 3.0.

Even though experience from both operating and abandoned plants, EGS-industry has, until recently, been lacking an international cooperation where knowledge can build-up and be exchanged between researchers. Serving this purpose, a 25 km<sup>2</sup> area in Utah was selected in 2018 for the FORGE project (Frontier Observatory for Research in Geothermal Energy), sponsored by the U.S. DOE. Here a highly fractured granitic pluton has been used for geothermal testing since the 1970-ties. The FORGE-project however, is an international underground field laboratory which shall serve, when fully implemented in 2020, for testing, developing and optimizing of the EGS technologies (U.S. DOE, n.d.-b). These types of projects are key-pillars in the road map for a wider application of the EGS-technology, especially concerning development of cost-effective deep drilling and establishing best applicable methodology for assessing EGS related properties of the bedrock at great depths.

Besides cost efficient drilling the bedrock has to have properties that facilitates the creation of a reservoir by hydro-shearing, which will give enough flow between the injection and production wells, and that the thermal properties (heat exchange) are satisfactory. The best case involves a homogeneously fractured rock mass with a temperature of at least 120° C. St1 and E.ON are aiming for systems that can generate between 10–50 MW heat, thus a flow in the ranges of up to 100 l/s. The geological evaluation of an EGS is based on various empirical data, which are of importance for the general assessment and the prediction models. The most important of these geological data involve information on:

- **structural rock conditions:** include textures, both effecting the frequency of fractures and most important when designing drilling program and correlation to seismic data,
- **rock type distribution:** relates to density, thermal conductivity, temperature and determines the drilling technique,
- **rock stresses:** crucial properties for hydraulic stimulation/shearing and orientation of the wells,
- **thermal properties:** determines the effective production of the plant and thereby the drilling depth. Gives the chemical effects on the plant during operation and constitute the basis for hydraulic modelling of the rock volume,
- **fractures:** frequency, type, orientation and distribution constitute the basis for the shearing operation,
- **hydraulic characteristics:** relates to permeability and chemical composition of formation fluid and gas,
- **seismic background data:** applied to characterize the rock mass, and also for monitor the effects of the hydraulic stimulation and

- **drillability:** based on several parameters, usually defined by the ROP (Rate Of Penetration). So far, no RDI (Rock Drillability Index) exist for percussion technique. Important to achieve knowledge on how the crystalline basement in Malmö can be drilled with the percussion technique.

### 1.3 Geological setting of SW Scania

The Precambrian bedrock in western Scania belongs to the Eastern Segment (ES) of the Sveconorwegian Province (Fig. 2). The rock is primarily made up of c. 1.7 Ga orthogneisses that underwent high grade metamorphism and ductile deformation during the Hallandian-, (c. 1.45 Ga) and especially the Sveconorwegian (1.1–0.9 Ga) orogens (Hubbard 1975; Möller et al. 2007; Bingen et al. 2008; Brander and Söderlund 2009; Ulmius et al. 2018). The Protogine Zone, PZ (Fig. 2) constitutes the eastern margin of the Sveconorwegian orogen (Bingen et al. 2008). It is displayed by several N–S trending, brittle and ductile deformation zones within a 10-20 km wide belt (Andréasson and Rodhe 1990). The metamorphic grade increases towards the west across the PZ; from greenschist- to upper amphibolite-facies conditions, displayed by high-pressure granulite, migmatite and eclogites in the ES west of the PZ (Möller et al. 2007; Bingen et al. 2008; Ulmius et al. 2018). East of the PZ the bedrock is dominated by the same protoliths, unaffected by the Sveconorwegian metamorphic event (Fig. 2) (Ulmius et al. 2018).

The structural framework of the bedrock in Scania today is largely the result of a several tectonic events in the Tornquist Zone (TZ), throughout Phanerozoic times. The TZ is north Europe's greatest deformation zone, which, 20–50 km wide intersects Scania in a NW–SE direction (Fig. 2) (Erlström et al. 1997; Sivhed et al. 1999). It is within the TZ the most intense inversion, brittle deformation and severe faulting have occurred within Scania. The tectonic history includes three major deformation events; the Caledonian, the Variscan, which are interpreted to have caused reactivation along older deformation zones, and the Alpine event that primarily overprint most of the previous tectonic structures.

The Alpine orogen includes the Kimmerian event in Triassic–Early Cretaceous, and the Laramide event in Late Cretaceous. Basaltic volcanism took place in central Scania during the Kimmerian event (Bergelin et al. 2011), but most distinct for this period are strike-slip movements that formed pull-apart-basins (Bergerat et al. 2007). The basins were, together with the Late Palaeozoic Variscan structures, inverted during the Laramide event, which resulted in significant uplift of the Tornquist Zone and subsidence of adjacent basins such as the marginal parts of the Danish Basin that involves SW Scania (Erlström 2020). The structures created during the Alpine tectonics are today displayed as the characteristic horsts and grabens in Scania. The horsts trending the same direction as the dykes, NW–SE, are actually ridges, built of tilted Precambrian bedrock blocks while the grabens constitute valleys holding up to km-thick Phanerozoic successions. (Bergerat et al. 2007; Erlström 2009). In figure 3, one of these horsts, Romeleåsen, is present-

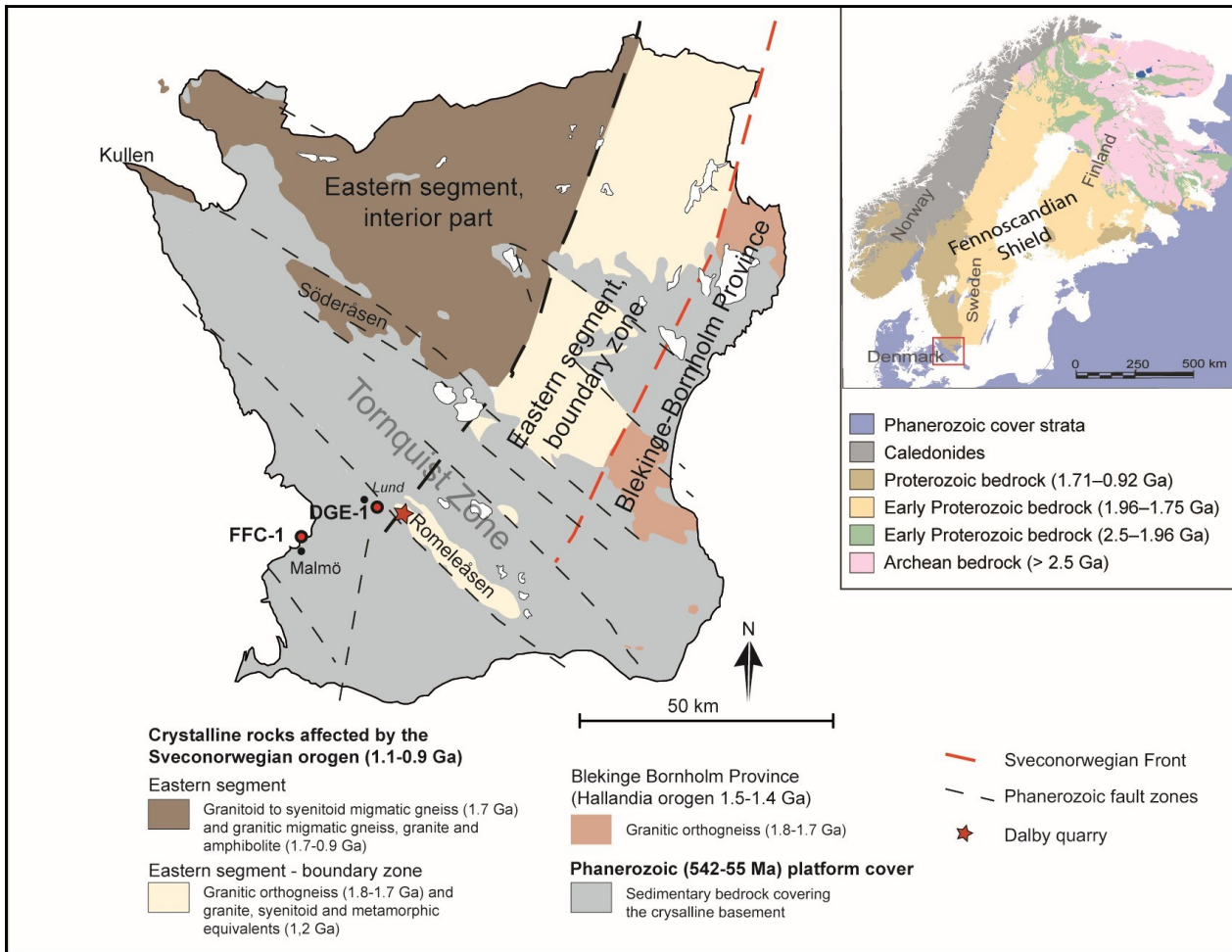


Fig. 2. Schematic map of Scania showing the main structural features and bedrock composition, as well as the location of the studied sites and boreholes. Figure modified from Erlström (2021).

ed. The Romeleåsen Fault Zone constitutes the SW boundary of the TZ as well as the SW boundary of the Romeleåsen horst with exposed and surficial uplifted Precambrian bedrock, exemplified in the Dalby quarry (Fig. 2). Corresponding crystalline bedrock is found on the footwall block to the SW at c. two kilometres depth, exemplified by the DGE-1 well (Rosberg and Erlström 2019).

The area where FFC-1 and DGE-1 are located, is often referred to as the Fennoscandian Shield Border Zone (Fig. 2). The area is defined as the by faults weakened southwestern margin of the Fennoscandian Shield. The area extends from north Jylland and north Kattegat, trough Scania, and ends towards southwest where the Fennoscandian bedrock disappears in north Germany (Erlström et al. 1997). The northern parts of the weakened shield margin include the regional Tornquist Zone (TZ) and the southwestern parts of the Kattegat-Skagerrak area (Fig. 2) (Bingen et al. 2008). This area has constituted a buffer-zone since the Late Palaeozoic because of its location between Fennoscandia and the more tectonically active regimes (Erlström 2020). Due to this it also displays a successively thinner crust to the SW in comparison to the inner parts of the shield (Erlström et al. 1997). The thickness of the crust varies from about 26 km on the Ringkøbing–Fyn High to 48 km for the inner parts of

the Fennoscandian Shield (Thybo 2000; Mogensen and Korstgård 2003). The thickness of the crust has been interpreted to be c.32 km in SW Scania. The crust thickness is of great interest as gradually thinner crust results in an increased heat flow and relatively higher thermal gradient (Balling 1995).

The crust of the Fennoscandian Shield margin has also been isostatically affected due to long periods of land-lowering and sediment accumulation that ended in Neogene time when the land started to rise, followed by heavy erosion, and land rise of 1–3 km (Japsen 1993; Jensen et al. 2003). It is reasonable to assume that the pressure release that followed the land rise created fractures several kilometres down in the bedrock (Balling 1995; Thybo 2000). The lithostratigraphic representation of the sedimentary succession is the result of blocks being exposed to both uplift and subsidence, as well as erosion and deposition during different periods. (Sivhed et al. 1999; Erlström 2009). The distribution of the various Phanerozoic strata is today well mapped, while the crystalline bedrock has mainly been studied on the exposed ridges (Fig. 2). The knowledge about the concealed crystalline basement in SW Scania is so far, before drilling of the FFC-1 well, based on few observations in oil and gas prospecting wells touching only the crystalline bedrock surface. We know that the orthogneisses repre-

sent reworked varieties of the Transscandinavian Igneous Belt (TIB) with mafic sheets of metabasite that follows the gneissic structure (Sivhed et al. 1999). From the Romeleåsen horst we know that at least two generations of mafic rocks, diabases, intersects the gneiss, whereas the younger c. 300 Ma old dykes cut the older (c. 1.2 Ga) (Fig. 3).

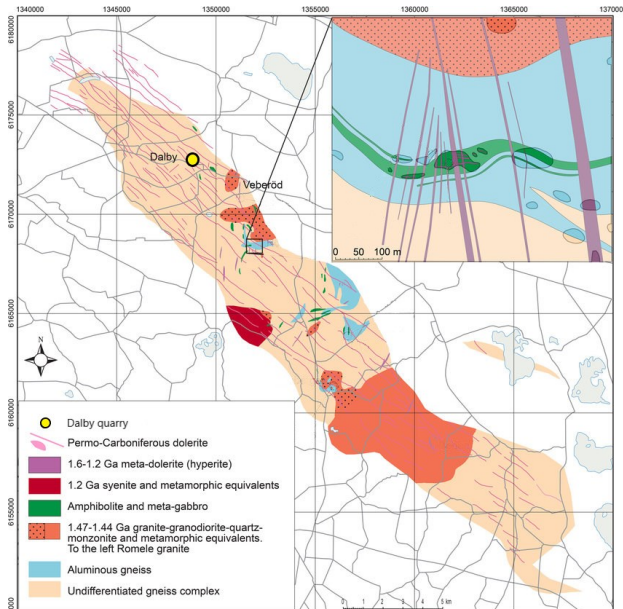


Fig. 3. Illustration of the main bedrock geology on the Romeleåsen horst. The location of the Dalby quarry is marked. Figure modified from Ulmius et al. (2015).

The structural framework of the sedimentary bedrock in SW Scania is relatively well outlined from seismic surveys performed during oil and gas prospecting in the 1970-ties. These data verify that there are several faults that penetrates the sedimentary succession in SW Scania. The major ones are the north-south oriented Svedala Fault that separates the Skurup Platform and the Höllviken Halfgraben. Other significant fault systems are the NNW oriented Amager and Öresund faults and the NW-oriented Foteviken and Vellinge faults (Erlström et al. 2018). All these have been active during the Triassic-Cretaceous. Older as well as less prominent faults in the basement are also likely present in SW Scania, though these are not possible to distinguish in the old seismic data with relatively low resolution and penetration depth.

Nevertheless, repeated tectonic events and reactivation of the fractures systems since the Cambrian is interpreted to have affected SW Scania in the same way as in the central parts of Scania. Thus, a severely fractured rock mass which includes both open and closed fractures (Erlström et al. 2004; Bergerat et al. 2007).

## 2 Data base

### 2.1 Outcrops and cores from the Dalby quarry

Dalby (Önneslöv) quarry (55.6° N, 13.4° E), is located in the western parts of the Romeleåsen horst and constitutes bedrock largely composed of crystalline bedrock (Fig. 3). The quarry was established in 1893 and industrial production of crushed rock started 20 years later. Today the quarry is operated by Sydsten AB that produces different rock materials for the construction



Fig. 4. Photograph showing the complex structure of the deformed gneiss in the Dalby quarry. The gneiss is characterized by ductile foliation, trending from lower left to upper right in the picture. The yellow-brownish impression given by the gneiss on the right side in the picture, is likely due to thin iron precipitations. Photo: H. Kervall (2021).

industry (Sydsten AB n.d.-a; Sydsten AB n.d.-b).

The bedrock is dominated by fine- to medium grained red-grey orthogneiss, often recrystallised and with varied frequency of veining (Sivhed et al. 1999; Persson and Göransson 2010). As illustrated in figures 4 and 5, the gneiss is intruded by numerous black mafic dykes that are more or less parallel to the gneissic foliation (Persson and Göransson 2010).

The metabasite dykes intruding the gneiss are interpreted to belong to a magmatic event, with dykes following the PZ further north. This event of dykes has been dated at c. 1.22 Ga (Söderlund and Ask 2006; Cederberg 2011). During the following Sveconorwegian orogeny the protoliths of the gneisses and the mafic dykes were jointly deformed and metamorphosed (Persson and Göransson 2010). The shared tectonic history is given by the metabasite dykes which are parallel to the gneissic fabric (Sivhed et al. 1999). The grey-black to greenish metabasite is gener-



*Fig. 5.* Photograph of the upper bench, facing north in Dalby quarry. The wall shows highly fractured gneiss with amphibolite veins and numerous metabasic dykes. Several orientations of the fractures can be observed in the picture. Note that the dominating orientation of the fracture planes coincide with the orientation of the gneiss foliation. Camera case on boulder centrally-left in lower part of picture for scale. Photo: H. Kervall

ally fine-grained. As a result of significant alteration, the metabasite veins have in places been transformed to chlorite.

A set of younger mafic dykes is associated with Permian–Carboniferous extension, around 300 Ma ago. During this event magma intruded and a swarm of NW–SE trending steeply dipping dolerite dykes formed. The up to c. 50 m wide dykes reflect an important period of extensional tectonics linked to the formation of horsts and grabens (Klingspor 1976; Bergerat et al. 2007; Malehmir et al. 2018). An example of an up to four-meter-wide sub-vertical dyke in the Dalby quarry is shown in figure 3. The dykes are associated with weakness zones in the host rock and fractures parallel to the dyke are commonly seen (Fig. 4). Other fracture directions, NE–SW and N–S also occurs, which relate mainly to E–W extension during periods of strike-slip movements along the main faults in the Fennoscandian Shield Border Zone (Persson and Göransson 2010).

In 2000 and 2002 Sydsten AB carried out 15 core drillings, adding 940 meters, to evaluate further mining in Dalby quarry. For this study Sydsten AB

offered access to cores and core documentation. The documented visual descriptions of the 15 cores, has been used for volume estimations of the rock types. During a visit to their core storage facility ten core pieces were selected from four of these cored boreholes. The borehole locations are shown in figure 6.

The selected cores represent different rock types with high fracture frequency. The aim was to both get representative samples of the various rock types and to get samples that illustrate the fracturing. Pieces with several generations of fractures were preferred. Six pieces of gneiss were chosen, whereas one exhibit the contact between gneiss and metabasite and one presenting the contact to a probable quartz vein. Three of the samples constitute different types of amphibolite and one sample is a diabase. From drill core number eight, seven levels have been sampled, which are presented, together with the core stratigraphy shown in figure 7. Drill cores six, seven and nine have only been sampled on one level each.

The sampled core pieces were polished for petrographic analyses with respect to mineralogy, texture, fracture frequency and fracture orientation. From the selected ten core pieces 11 thin sections were produced (Table 1). Seven additional rock samples were collected from the quarry wall during a second field visit to the quarry. These were c. 20\*20 cm in size and used for thermal conductivity and density analyses. These samples were taken from quarry benches 4 and 1 (72 m and 18 m depth respectively, below ground level). The samples were furthermore selected on the basis to be representative for the bedrock as well as



*Fig. 6.* Aerial view of the Dalby quarry with locations of the sampled core drillings No:6-9. The picture is from a 3D-model, produced by Schakt & transport for Sydsten AB.

not being too fractured, as thermal analyses must be performed on unfractured rock. Of the selected samples, five samples constitute three different types of gneiss and two samples of amphibolite. A presentation of the Dalby samples and performed analyses is given in Tables 2 and 3.

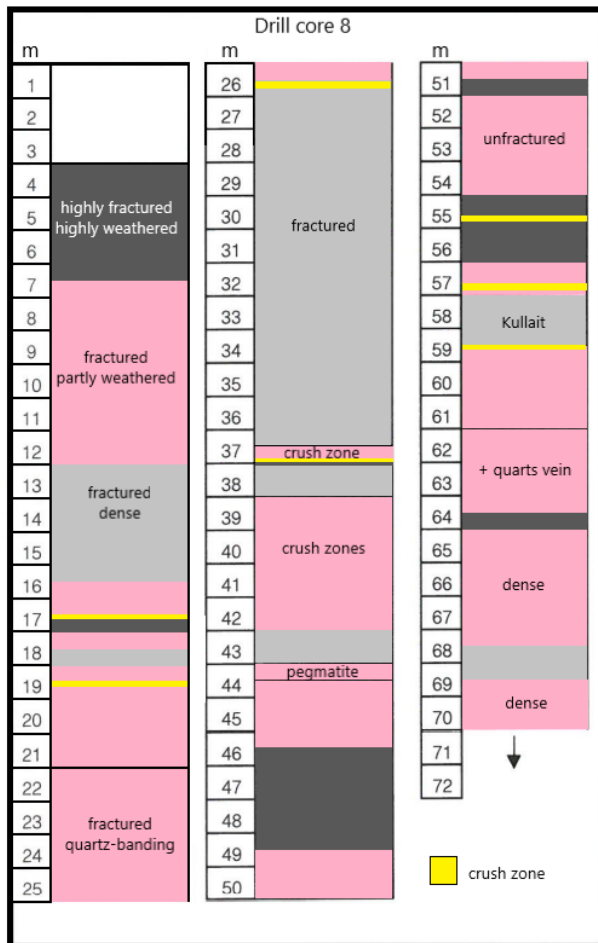


Fig. 7. Stratigraphy of drill core no. 8 from Dalby, marked with sampled levels, and characteristics of the rock types and fracture characteristics. The stratigraphy is based on core documentations from Sydsten.

## 2.2 The FFC-1 borehole

FFC-1 (55.6° N, 13.0° E) is located at Flintrännans Fjärrvärmecentral (FFC) in the north harbour, approximately 2.5 km from Malmö city centre (Fig. 8). The area is built on land fill sediments which have been deposited periodically since before the first drillings in 2002 and 2003. The top of the Precambrian crystalline bedrock is located at 2112 m depth, and subcrops a sedimentary bedrock succession which, down to 1600 m is mainly composed of Upper Cretaceous limestone. Between 1600 and 2100 m the sedimentary succession is composed of an alternating sequence of Lower Cretaceous, Jurassic and Triassic sandstone and claystone beds. The sedimentary succession is general poorly consolidated and includes several highly permeable sandstone aquifers. When the drilling resumed in the summer of 2020 the FFC-1 well, was extended to 3133 m depth, thus reaching more than one kilometer into the underlying crystalline basement.

### 2.2.1 Drilling operation of FFC-1

The drilling started with placing a liner inside the old well down to 2142 m to seal off and secure the existing well. From there on the drilling started with ham-



Fig. 8. Aerial view of Malmö north harbour with the location of FFC-1. Modified from Lantmäteriet © (2021). Small picture to the right modified from <https://opendataimpactmap.org/> (2021).

Table 1. Summary of samples from Dalby quarry. The table gives information on drill core id no, core box (Sydsten AB id no) and depth/depth interval, rock type and sample code of the polished core and thin section.

Drill core no.	Box no.	Depth (m)	Rock type	Polished core	Thin section
6	4	25.3	<i>Amphibolite fine-grained, foliated</i>	D1A	D1B
8	2	16	<i>Gneiss pale pink. Metabasite dark</i>	D2A	D2B
8	3	18.4	<i>Gneiss light red</i>	D3A	D3B
8	4	26.5-26.7	<i>Diabase aphanitic, dark</i>	D4A	D4B
8	6	37	<i>Gneiss light red (crush zone)</i>	D5A/D6A	D5B, D6B*
8	8	54.7	<i>Amphibolite heavily metamorphosed</i>	D7A	D7B
8	9	56.7	<i>Gneiss medium red</i>	D8A	D8B
8	9	58.5	<i>Gneiss red-grey gneiss, rich in darker minerals</i>	D9A	D9B
7	9	58.5-58.8	<i>Garnet-amphibolite</i>	D10A	D10B
9	6	37.15	<i>Gneiss deep red</i>	D11A	D11B

\* Two thin sections were produced from one core

mer drilling with a 170 mm hammer. After time-consuming efforts to handle large volumes of water coming into the well from the severely fractured upper part of the bedrock E.ON decided to drill the remaining part of the well from 2242 m with conventional 6 1/2" and 6 1/8" rotary drilling. Numerous bits were tested but still the penetration rate did not exceed 5 m/hr, which is considerably slower in comparison to the hammer technique if that had worked. However, the rotary drilling was successful in the sense that water inflow to the well could be controlled and a depth of 3133 m could be reached within the scheduled time frame for the drilling.

### 2.2.2 Geological well site work during drilling of FFC-1

The main tasks were to sample, describe and monitor the geology during the drilling. The drilled rock was described primarily regarding: rock type, color, texture and grain size, main minerals and trace components/minerals, frequency of fractures and fracture minerals and shape of the cuttings. Coring was originally intended to be performed for scattered intervals but this operation was abandoned due to time and cost related issues. The sampled cuttings constitute, thus, the basis of the geological descriptions. About 300 grams (50g + 250g as reference) of cuttings were collected for every two meters interval. For some intervals several fractions were collected to ensure representative samples since the relative occurrence of the rocks varied with grain size. The drilling as well as the well site geological operations went on around-the-clock. This was possible since five people worked in shifts of 12 hours during the whole drilling operation. Three mud-loggers were responsible for collecting, cleaning, drying and bagging the cuttings. During the hammer drilling in the upper part (2150–2242 m) the sampling took

place under a cyclone. The sampling during this interval was generally problematic, the cutting size and amounts were overall small and depth correlation difficult. During the rotary drilling operation, 2242–3133m, the samples were gathered from the shale shakers. These consist of a set of screens that separate the cuttings from the drilling fluid (mud) coming from the borehole. Wooden planks were placed along the shaker's outlet for the cuttings to build-up on. The planks were then scraped clean after each sampling so that representative samples could be obtained for respective interval. During the rotary drilling drilling-mud additives aggravated the cleaning of the samples, the sampling was otherwise satisfactory both regarding cutting size, quantities of cuttings and depth correlations.

The operation geologist had the overall responsibility for the geological work. The geological description was carried out by two well-site geologists, based on microscopy and monitoring of the drill technical parameters such as rate of penetration (ROP), rotation force (Torque), weight on the drill bit (WOB) and rotation of the drill string in rounds per minute (RPM). The monitoring was enabled by GeoDATA's real-time well data visualisation system which purpose was to facilitate correlations between observed operational changes in drillability with shifts in the bedrock composition. However, the frequent change of borehole assemblies (drill bits, turbine etc) often aggravated this correlation. The drilling parameter data was delivered digitally to E.ON in LAS-format by GeoDATA and incorporated in the well site mudlog using the Logplot Ver 8 software from RockWare Inc.

The geological observations were summarized in daily geological reports, DGR:s, by the well-site geologist after each completed day of geological work. An example of the DGR is shown in figure 9.

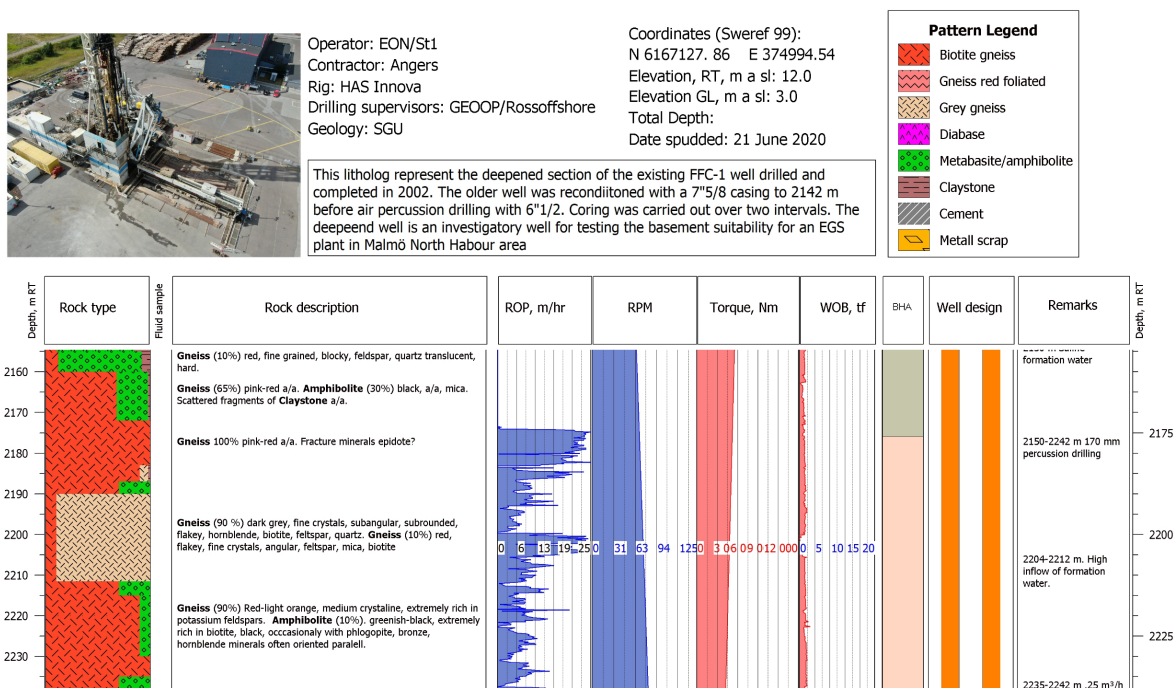


Fig. 9. Excerpt from the mudlog compiled at the well site at FFC-1. The log presents the rock types in percent, based on examination of cuttings, rock description and remarks. The drilling related properties of ROP, Torque, WOB and RPM are illustrated as graphs.

The DGR contained, besides geological information, drilling technical data, photo documentation and a visual graphic mud log for the drilled section. The mudlog graphically present geological, geotechnical and geophysical data. The columns are presented side by side to easily trace relationships between geo-

physical changes and the composition of the bedrock. A comprehensive description of the geological work during the drilling operation is given in a report by E.ON (2020). Figure 10 shows the final interpretations log, conducted by Rosberg and Erlström (2021)

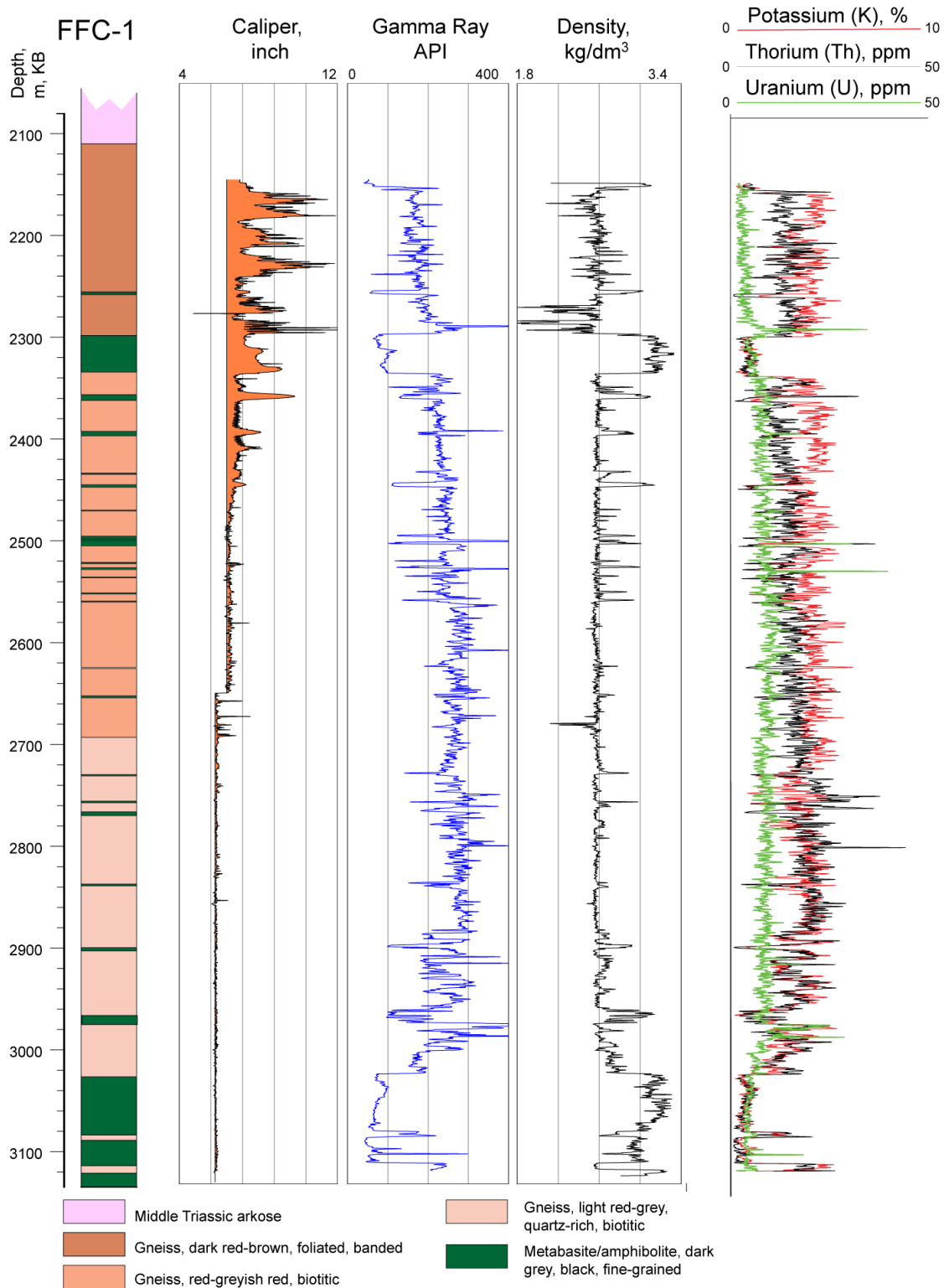


Fig. 10. Showing a compiled interpretation based on cuttings and geophysical data from the FFC-1 drilling. Columns from left to right gives: Bedrock composition with rock legend, Caliper (gives the diameter of the well), Gamma Ray (presenting naturally occurring radioactive isotopes in the bedrock), Density gives the overall density of the rock. In the last column the radioactive isotopes from the spectral gamma are shown as separate curves. The log and interpretations have been done by Mikael Erlström.

Table 2. List of rock samples D1-D11 from Dalby quarry. The samples are presented with the number of the drill core it was taken from and the depth/depth interval, in meters below surface. Analyses performed on each sample is stated in the three columns to the right. For location of the core drillings see figure 6.

Sample	Rock type	Analyses		
		Petrography		SEM-EDS
		Polished core	Thin section	
D1	<i>Amphibolite fine-grained, foliated</i>	D1A	D1B	yes
D2	<i>Gneiss pale pink. Metabasite dark</i>	D2A	D2B	yes
D3	<i>Gneiss light red</i>	D3A	D3B	yes
D4	<i>Diabase aphanitic, dark</i>	D4A	D4B	yes
D5	<i>Gneiss light red (crush zone)</i>	D5A/D6A	D5B	yes
D6	<i>Gneiss light red (crush zone)</i>	D5A/D6A	D6B	no
D7	<i>Amphibolite heavily metamorphosed</i>	D7A	D7B	no
D8	<i>Gneiss medium red</i>	D8A	D8B	no
D9	<i>Gneiss red-grey gneiss, rich in darker minerals</i>	D9A	D9B	yes
D10	<i>Garnet-amphibolite</i>	D10A	D10B	yes
D11	<i>Gneiss deep red</i>	D11A	D11B	yes

Table 3. List of outcrop samples D19-D36 from Dalby quarry. Analyses performed on each sample are given in the two columns to the right.

Sample	Rock type	Analyses	
		Density	Thermal conductivity
D19	<i>Gneiss red, fine-grained, foliated</i>	D19D	D1T
D20	<i>Gneiss red, massive, fine-grained, granitic</i>	D20D	D2T
D21	<i>Gneiss red, medium foliated, biotitic</i>	D21D	D3T
D22	<i>Gneiss light red-grey, fine-grained</i>	D22D	D4T
D23	<i>Gneiss red, medium/weakly foliated</i>	D23D	D5T
D24	<i>Amphibolite/Metabasite</i>	D24D	
D25	<i>Amphibolite/Metabasite</i>	D25D	
D26	<i>Amphibolite/Metabasite</i>	D26D	D8T
D27	<i>Amphibolite/Metabasite</i>	D27D	
D28	<i>Gneiss</i>	D28D	
D29	<i>Gneiss</i>	D29D	
D30	<i>Gneiss</i>	D30D	
D31	<i>Amphibolite/Metabasite</i>	D31D	
D32	<i>Amphibolite-gneiss</i>	D32D	
D33	<i>Diabase dark grey, microcrystalline</i>	D33D	
D34	<i>Amphibolite/Metabasite</i>	D34D	D16T
D35	<i>Gneiss</i>	D35D	
D36	<i>Gneiss</i>	D36D	

that later was compiled and added to the FFC-1 drilling report. The data in the log is besides the mud log data based on results from the geophysical wire line logging.

All analyses and thin sections produced from FFC-1 are based on cuttings. Cuttings have been hand-picked and collected from several coherent depth intervals to obtain representative samples for each rock type. All together 32 samples have been included in this study, 16 for thin section preparation, 10 for chemical analyses and five for analysis of the thermal conductivity (Table 4).

Fourteen of the thin sections represent depth intervals of four meters, one thin section contains cuttings gathered from a six m interval, and two represent eight meters intervals. From ten of these intervals another 25 grams was gathered for chemical analyses. The chemical analyses constitute of eight samples selected from one–four meters depth intervals and two samples was carried out from intervals of six respect

tively eight meters. In addition to the chemical analyses of the bedrock composition an assumed fracture mineral, frequently occurring during the drilling of the test hole, was analysed. This mineral was selected from a four meters interval. For the thermal conductivity analysis 0.5 litres of cuttings were gathered per sample. These samples were collected from intervals of 3, 2, 10, 2 and 2 meters respectively.

### 3 Methods

Primarily the methods applied were chosen with the aim to find out whether the rock types documented on the Romeleåsen horst, exemplified with the samples from the Dalby quarry, are similar to the ones found at great depth in the FFC-1 borehole. This has involved visual examination of cores and cuttings, microscopy, SEM-EDX, thermal- and chemical analyses. A summary of the methods used, and samples investigated from Dalby quarry and FFC-1 is presented in Tables 2–4)

### 3.1 Visual examination of cores

The core pieces from Dalby quarry were sawed lengthwise and polished. The polished samples (D1B–D11B) varied in lengths between 9 and 19 cm. The pieces were polished using a Struers Roto Pol-25 with Struers Waterproof Silicon Carbide paper P, #220 C to #1200 C (coarser sandpaper was used initially and as the work proceeded, finer grinded paper was used until visible scratches were removed). Each core piece was thereafter scanned using an Epson Perfection V300 Photo scanner at high resolution (300 dpi). Photographs were taken with a Canon EOS 550D and for the macro photographs an USB digital microscope, 50–1000–X, 8 HD-LED-endoscope camera was used.

#### 3.1.2 Microscopy

##### *Dalby*

Petrographic microscopy was performed for identification and quantification of minerals, fractures and other characteristic features. The core samples were cut into smaller pieces, using a Steinadler AR-750 rock saw. In total 13 thin sections (28·48 mm), standard thickness (25–30 µm) were prepared by Piotr Krzemiński at Abcahead, Warsaw, Poland. The thin sections, D1A–D11A (Table 2) were cast without cover glass, to enable both petrographic microscopy and SEM-analysis. The petrographic analysis was performed using a LRI Olympus microscope, and Plan N, zooming 2x, 4x, 10x and 40x objectives. For photomicrographs the software ImageView was used.

The modal quantification based on point counting was performed on plain polarized light (PPL) and cross-polarized light (XPL) photomicrographs in the

software J Micro Vison. Point counting was performed on eight thin sections. On these 800 points were counted each. The classification of the igneous rocks was conducted through plotting in QAP-ternary diagrams. The metamorphic rocks were primarily classified based on the IUGS-SCMR flowchart and glossary.

##### *FFC-1*

For petrographic microscopy and SEM-analysis 17 thin sections, (29·44 mm), standard thickness (25–30 µm), were prepared by ThinSectionLab, France (Table 4). Each thin section was made from 20g of cuttings casted in epoxy. As for the samples from Dalby the FFC-1 thin sections were scanned using an Epson Perfection V850 Pro, 6400 dpi, with polarization filter on scanner glass (simple for PPL and double crossed 90° for XPL).

#### 3.1.3 SEM-EDX

SEM-EDS analysis have been performed on the thin sections from Dalby (Table 2). The aim of SEM-analysis was to produce images and study the structures of the rocks on a detailed level. The purpose of the EDX-analysis was to complement the microscopy, to support/dismiss interpretations made from the microscopy through chemical element indications. To avoid non-conductive samples from charging during analysis, the thin sections were sputter-coated with a 10–15nm thick coal layer under a 150 Am/bar vacuum, using an Agar auto carbon coater. The samples were then placed in a TESCAN Mira3 scanning electron microscope (SEM). In the SEM an electron beam

*Table 4.* List of investigated cutting samples from the FFC-1 well in Malmö north harbour. Rock classification is based on modal composition, presented with depth/depth interval from which the sample represent. Analyses performed on each sample are given in the three columns to the right.

Sample	Rock type	Depth (m)	Analyses			
			Petrography Thin section	Chemistry	Thermal conductivity	Density
M1	<i>Gneiss deep red</i>	2186-2187	M1TS	M6C		
M2	<i>Gneiss deep red</i>	2215	M2TS			
M3	<i>Amphibolite black</i>	2215	M3TS	M4C		
M4	<i>Gneiss red-grey</i>	2434-2435	M4TS	M11C		
	<i>Gneiss quartz-rich</i>	2771-2774			M1T	M1D
	<i>possible fracture filling</i>	2771-2774		M5C		
M5	<i>Gneiss red-grey</i>	2853-2857	M5TS			
M6	<i>Gneiss grey, quartz-rich</i>	2853-2857	M6TS	M8C		
	<i>Gneiss</i>	2873-2875			M2T	M2D
M7	<i>Gneiss red</i>	2944-2952	M7TS	M7C		
M8	<i>Gneiss grey, quartz-rich</i>	2948-2952	M8TS	M9C		
M9	<i>Gneiss, red-grey</i>	2950-2952	M9TS	M10C		
M10	<i>Amphibolite grey-black</i>	2950-2952	M10TS	M3C		
	<i>Gneiss/Granodiorite</i>	2954-2965			M3T	M3D
M11	<i>Amphibolite black</i>	3060-3062	M11TS			
M12	<i>Gneiss deep red</i>	3060-3068	M12TS			
M13	<i>Gneiss grey</i>	3060-3062	M13TS	M2C		
M14	<i>Gneiss red-grey</i>	3060-3062	M14TS			
	<i>Amphibolite/Metabasite</i>	3098-3100			M4T	M4D
	<i>Amphibolite/Metabasite</i>	3104-3106			M5T	M5D
M16	<i>Gneiss red-grey</i>	3129-3132	M16TS			
M17	<i>Amphibolite, black</i>	3129-3132	M17TS	M1C		

is scanned on the sample surface, resulting in different types of emitted electrons that can be detected. For obtaining high-magnification images with topographic information SE (secondary electrons) are detected. For images presenting compositional information, BSE (back-scattered electron), which penetrate the surface, are detected (Egerton and Springerlink 2016).

The SEM-analysis was operated through the software programme Tescan Mira. During the analysis the acceleration voltage was set to 15 kV and a work distance of minimum 10nm was used. The SE- and BSE-images were then used when interpreting where the spot-analyses in the EDS (Energy Dispersive X-ray Spectroscopy) would be performed. When spots were selected the EDS measured the energy of the X-rays and converted it into qualitative and quantitative element data (Russ 1984). The data was then operated through the software program Aztec. Three to five spot analyses were conducted on each mineral. Preparatory work and analyses were performed in the SEM-laboratory at Geocentrum, Lund university. In total 68 SEM-EDX analysis have been conducted.

## 3.2 Thermal analysis

### 3.2.1 Dalby

The larger rock samples from Dalby quarry were sawed into a suitable cubic size of c. 1 dm<sup>3</sup>, thus, sides around 10 cm. The analyses were thereafter performed by the Geological Survey of Sweden in Uppsala using a Thermal Conductivity Scanner (TCS). The equipment used is manufactured by Lippmann and Rauhen GbR in Germany. The TCS measures the thermal conductivity (TC) and thermal diffusivity (TD) with 3% accuracy, by applying optical scanning technology of plane or cylindrical surfaces (along the cylinder axis) of rock or core specimens, using infrared temperature sensors in combination with a mobile, focused, and continuously operated heat source. The sample temperature is measured by the sensors before and after heating. Typically, two reference probes with known thermal properties are analysed together with the sample (Popov et al. 1999).

### 3.2.2 FFC-1

Five samples á 0.5 litres of cuttings were analysed regarding the thermal conductivity of the material, using the transient line source method. The cuttings were initially processed and reduced so that they do not contain any coarse or sharp-edged parts larger than approx. 1 mm. The measure principle is based on the replacement of air between the grains, with a fluid of known thermal conductivity. The method requires a non-dissolvent fluid, which does not react chemically with the sample, normally fresh water. The thermal conductivity of the mixture (cuttings + water) is then measured using a TK04 conductivity meter. By subtracting the known thermal conductivity of the fluid from the test results, the thermal conductivity of the solid material can be determined (Thermophysical Instruments Geothermal Investigation 2021). Analysis and the matrix thermal conductivity calculations was performed by RWTH Aachen University (Klitzsch and Ahrensmeier 2021).

## 3.3 Chemical analysis

### 3.3.1 FFC-1

Corresponding cuttings prepared for the FFC-1 thin sections were also used for a chemical analysis. Eleven samples of 25 g cuttings were analysed (Table 4). In addition to the bedrock analyses an assumed fracture mineral, frequently occurring during the drilling of the test hole, was analysed. Material from this mineral was selected from a 4 meters interval.

The bedrock samples were analysed by ICP-AES (Inductive Coupled Plasma-Atomic Emission Spectroscopy) and ICP-MS (Inductive Coupled Plasma-Mass Spectroscopy) by ALS Chemicals, using same analytical standards as SGU (Sveriges Geologiska Undersökning) does for their rock samples. The fracture mineral was analysed using an X-ray diffractometer (XRD) with respect to total mineral content in non-oriented total sample ("WR") and clay mineral content in oriented sample ("OR") of therefore separated fine fraction. Five analytical treatments and XRD analyses were performed on the sample at SGU's mineralogical laboratory in Uppsala.

## 4 Results

The performed investigations give a comprehensive description of dominating rock types in the Precambrian basement of southwest Scania. The results in the following text start with the study of the samples from the Dalby quarry, followed by the descriptions of the cuttings from FFC-1. The focus lies on description of the mineralogical, textural and physical properties of the rocks, which direct and indirectly are of importance for an assessment of deep geothermal energy systems in SW Scania.

### 4.1 Dalby quarry

The investigated cores and rock samples from the quarry display two main rock groups, i.e., 1) felsic granitoid rocks (primarily gneiss), 2) mafic rocks of a) amphibolite and metabasite and b) diabase. The following text focus on describing the main characteristics, exemplified by a selection of photographs and illustrations.

#### 4.1.1 Felsic granitoid rocks

The following description is based on the seven polished core samples (Fig. 11), seven thin sections and SEM-EDX analyses.

#### *Minerology and texture*

The gneisses are by far the most common rock type in the Dalby quarry. The dominantly fine-grained gneisses vary from pale pink to light red, medium red, deep red and red-grey (Fig. 11). In general, the redder types include more alkali while the light-coloured varieties are comparatively rich in quartz and the darker variants contain higher amount of mafic minerals. All the samples have been given a descriptive name, presented under rock type in Table 5. Results from point-counting on five of the samples form the basis for modal classification, which is based on observed minerology (Fig. 12). These results are summarized in Table 5, which also gives the mineral composition of each sample in percent. Strong deformation has made



*Fig. 11.* Polished core slabs of felsic core samples from Dalby. (A): sample D3A; dark-banded gneiss (B): sample D5A/D6A, light red granite (upper part- D5A) and light red gneiss (lower part- D6A) (C): sample D8A weakly banded gneiss (D): sample D9A gneiss rich in darker mineral (E): sample D11A; gneiss from a crush-zone (F): sample D2A (upper part) pale-coloured granite. Photo: H. Kervall.

Table 5. Summary of the point-counting results of the felsic core samples from Dalby. The mineral composition is given in percent by the three most dominant minerals. Accessory minerals constituting < 1%, are only noticed by name. Note also that the point counting represents the thin section, and not necessarily the whole core.

Sample	Rock type (defined by texture)	Quartz (%)	Feldspars		Modal classification (defined by mineralogy)	Assessory minerals
			K-Fsp (%)	Plag (%)		
D2A	Granite, pale-coloured	17	no obs.	75	Quartz diorite	biotite (6%), opaque (1%), titanite
D3A	Gneiss, dark banded	30	23	42	Granite	biotite, zirconium
D5A	Granite, light red	25	25	45	Granite	biotite, opaque (2%)
D6A	Gneiss, light red	33		65	Tonalite	biotite (2%)
D8A	Gneiss, weakly banded	64	9	25	Granitoid, quartz-rich	biotite
D9A	Gneiss, rich in darker minerals	x	x	x	-	biotite, garnet, iron oxide-hydroxide or hematite
D11A	Gneiss, crush-zone		x	x	-	biotite

mineral identification difficult for two of the samples. These samples (D9A and D11A) have therefore only been given a metamorphic descriptive classification, based on texture and composition. In figure 13A the most common minerals identified are displayed in a photomicrograph.

The point counting results, i.e., the modal classification, indicate that the rocks have a quartz-diorite, granite, tonalite or quartz-rich granitoid composition. The results are illustrated by the ternary plot in figure 12. The point counting results display a rather high variation of the quartz content, between 17% in sample D8A, to 64% in sample D2A. Except sample D5A/D6A and D11A, all the samples contain a few percentages of biotite, which often appears as elongated plastically deformed mineral aggregates (Fig. 13B).

Microphotographs showing examples of the mineralogy of the felsic rocks in Dalby are displayed in the figures 13A–F. Sample D9B contains <2mm euhedral diamond-shaped megacrysts, which distinguish by their larger grain size than surrounding matrix (Figs. 13C and 15A). The EDX-analysis gives that these are either hematite (Fe<sub>2</sub>O<sub>3</sub>), magnetite (Fe<sub>3</sub>O<sub>4</sub>), or/and iron oxide-hydroxide (FeOOH). Further acces-

sory minerals found are zircon (ZrSiO<sub>4</sub>) in D3A, and titanite/sphene (CaTiSiO<sub>5</sub>) in D2A. Titanite is displayed in figure 13D, where the crystals form a ductile band at the contact between two rocks in sample D2A. Skeletal shaped, incomplete formed crystal of garnet are present in sample D9A (Fig. 13C).

All samples display a tight texture with interlocking crystals (Figs. 13A and 13E). More than half of the samples show highly variable mineral composition within the sample. A majority of the samples are anisotropic, meaning that the mineral grains display a preferred orientation (Fig. 13B). Sample D2A, is homogenous and isotropic, thus illustrates a uniform composition and randomly oriented grains (Fig. 13D). D6A and D9A is also homogenous but anisotropic. The other samples display a heterogenous and anisotropic texture.

All samples except D11A display extensive saussuritization of the plagioclase grains. This gives the plagioclase grains a fine-grained dusty appearance (Fig. 13A). Tartan and/or albite twinning is observed in all samples. Tartan twinning displaying a cross-hatched pattern, in the potassium-feldspar microcline (Fig. 13A) whereas albite twinning gives striped laminae in plagioclase grains. The EDX-analyses gives that some of the plagioclase feldspars are calcium-rich anorthite, but the dominating feldspar is sodium-rich albite. In sample D3A sodium-rich feldspars show a perthite texture (Fig. 13E). The texture gives the grain a typical “tiger-striped” pattern due to potassium-feldspar intergrown. Plastic deformation, giving the mineral grains and structures a distorted bended appearance, is commonly observed in all the samples. The deformation is mainly displayed by grains of calcite, feldspar, quartz and biotite, exemplified by distorted grains of biotite in sample D9A (Fig. 13B). Plastic deformation is furthermore seen by boudinage structure in sample in D5A (Fig. 15B), and a deformed calcite fracture in sample D2A (Fig. 15C). In sample D2A (Fig. 13D) there is a ductile band of secondary formed titanite crystals between two rock contacts. Foliation is displayed in samples D3A, D9A, D11A and indicated in D5A/D6A. The deformation is also

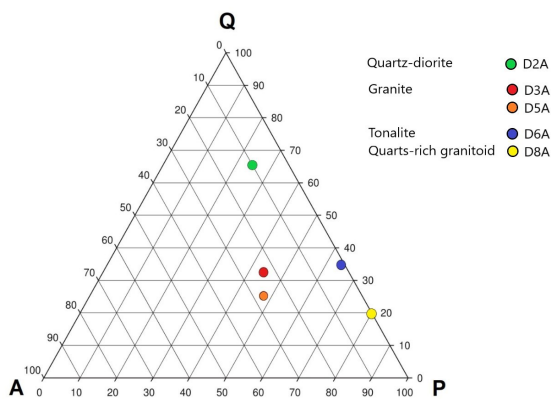


Fig. 12. Ternary diagram showing the composition of the felsic samples. Q (quartz), P (plagioclase), A (alkali-feldspars).

present on a smaller scale, as seen in sample D8A where minerals have started to form at grain boundaries of other minerals (Fig. 13F)

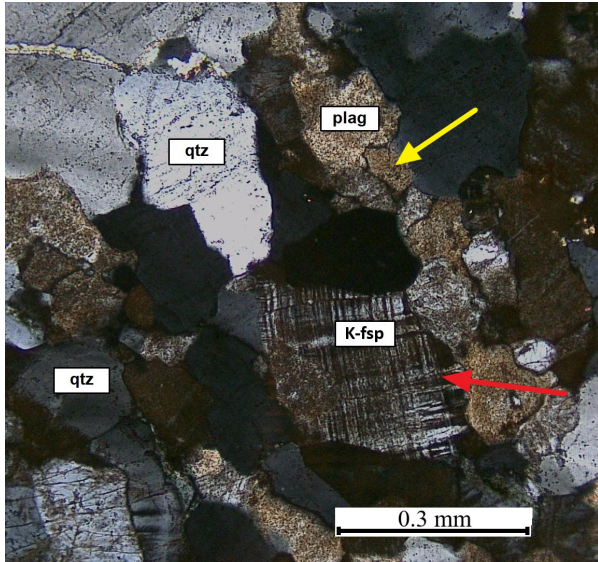


Fig. 13A. Microphotograph of sample D5B with plagioclase (plag), K-feldspar (K-fsp) and quartz (qtz). Saussuritization texture on the plagioclase grains, giving them a brownish griny appearance (yellow arrow). Tartan twinning in K-fsp (red arrow) PPL-image, 10x.

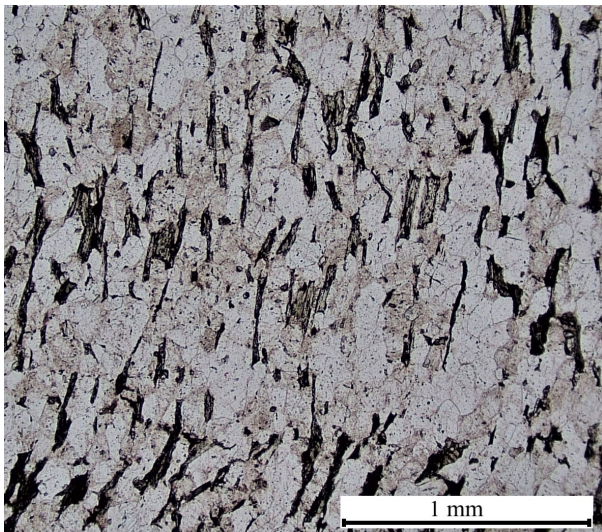


Fig. 13B. Anisotropic fabric. Crystallographic orientation of elongated and distorted biotite grains (dark in the picture). Microphotograph of sample D9B, in PPL-light, 10x.

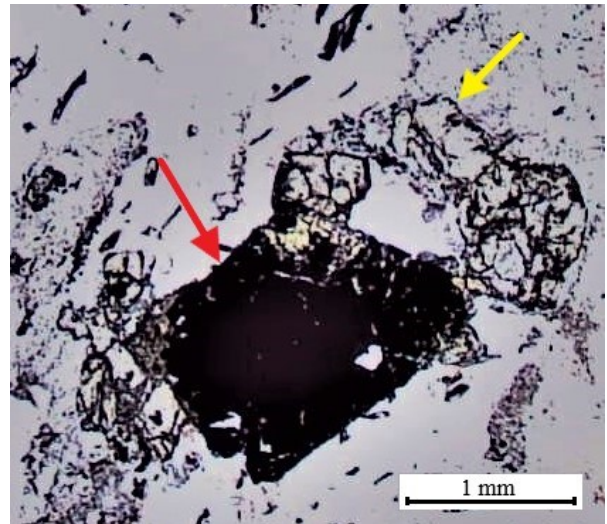


Fig. 13C. Microphotograph of sample D9B showing hematite,  $Fe_2O_3$  (red arrow) and skeletal garnet (yellow arrow), PPL-image, 10x.

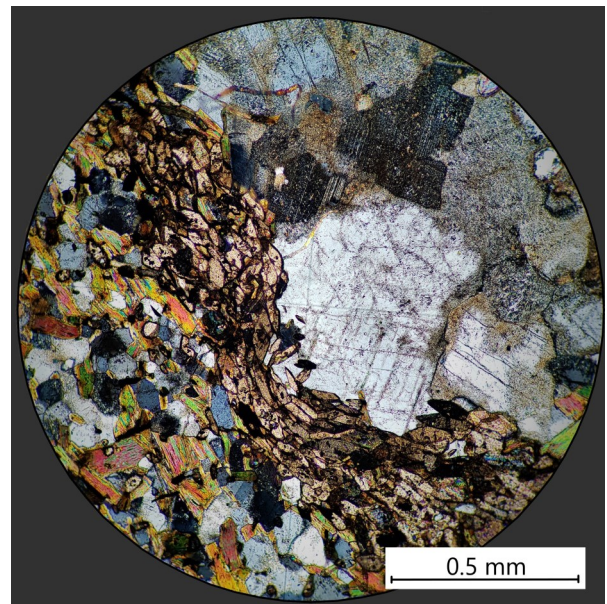


Fig. 13D. Microphotograph of sample D2B showing the ductile contact, composed of titanite crystal, between gneiss and anisotropic metabasite, where the grains are oriented aligned with the ductile band (lower left). The upper right part constitutes of isotropic granite, with no preferred orientation of the grains. XPL-image, 4x.

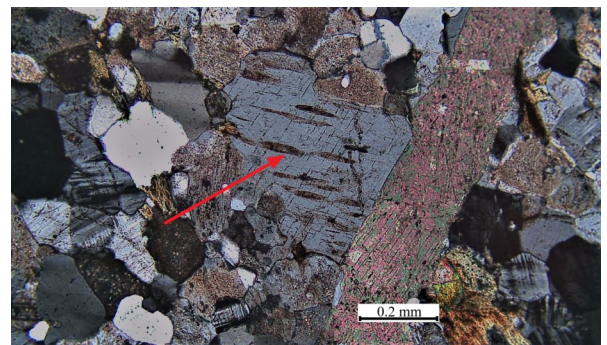


Fig. 13E. Microphotograph of sample D3B shows an albite grain with exsolution lamellae of orthoclase (red arrow), so called perthite texture. XPL-image, 10x.

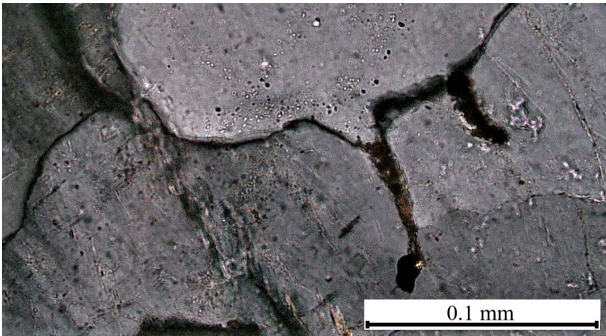


Fig. 13F. Microphotograph of minerals that have started to form at the grain boundaries, sample D8B, XPL-image, 40x.

### Fractures

The following description of fractures is based on the orientation of the principal stresses the rock has been exposed to, subdivision by Fossen (2010). The three types of main fractures displayed; extension fractures; divided in extension- and contraction-, and shear fractures as well as the result of ductile deformation are illustrated in figure 14. Table 6 summarizes the fractures observed in the felsic cores.

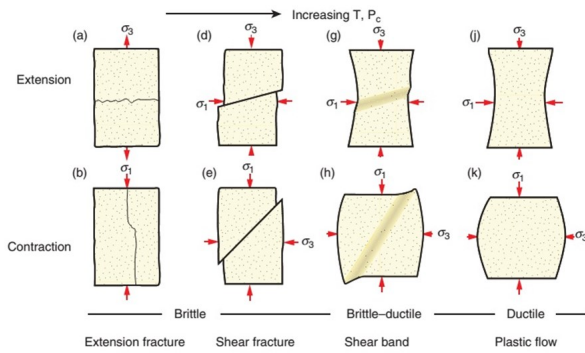


Fig. 14. Illustration of the main types of deformation structures that develop under extension and contraction. Modified from Fossen (2010).

Table 6. Summary of fracture types and fillings that occur in fractures >0.2mm and <2 mm in the Dalby felsic cores. The first column state if several generations of fractures have been identified. All observed fractures >0.2mm wide contain fracture filling. For fractures <2 mm wide, fracture fillings are presented as well as occurrence of empty fractures. For fracture types that display more than one type of fracture, the types have been ranked in the order they occur, from the most, to the least abundant type. The same ranking system have been applied to the fracture filling minerals.

Sample	Several generations of fractures	Larger fractures (>0.2mm)			Minor fractures (<0.2mm)		
		Fracture type	Fracture filling	Open fractures	Fractures undefined	Fractures filling	Open fractures
D2A	only intragranular	shear, contraction	calcite	no	yes	quartz. calcite. dark unidentified mineral	yes
D3A	no	extension	calcite	no	yes	calcite	no
D5A	yes	shear, contraction	quartz, calcite, FeOOH/hematite	no	yes	quartz. calcite. FeOOH/hematite	yes
D6A	yes	extension, shear, contraction	black unidentified non-carbonific. calcite. epidote	no	yes	quartz	no
D8A	yes	contraction, shear, extension	quartz. calcite	no	yes	quartz	yes
D9A	yes	contraction	calcite	no	no	grey carbonific unidentified. light yellow unidentified	no
D11A	yes	contraction, shear, extension	All non-calcareous: epidote. yellow, black, grey, orange, white minerals	no	yes	epidot. quartz. black, white, yellow and grey unidentified mineral, all non-carbonific	yes

The investigated core samples all contain >0.2 mm wide fractures, while 85% of them also contains <0.2 mm wide microfractures (Table 6). The microfractures are generally < 0.1 mm wide and less than ten millimetres long.

In figures 15A–G microphotographs showing examples of fracture types and fracture fillings observed in Dalby are displayed. The smallest fractures are intragranular, meaning they occur within singular mineral grains (Figs. 15D and 15E). In figure 15D five generations of intergranular fractures are presented. Most of the samples display several generations of fractures, indicated by intersecting fractures and different fracture minerals (Figs. 15A–B)

Approximately 50% of the transparent to milky, off-white, and grey fracture fillings react to acid, indicating that they belong to the carbonate group. SEM-EDS analysis verify that most of these carbonates are calcite, often enriched in manganese (Mn) and iron (Fe). Among the non-carbonate fracture minerals, the turquoise mineral epidote is relatively common (Figs. 15D–E). Yellow and grey-blackish non-carbonate fracture minerals are also noted, coexisting in most of the plastically deformed samples, D9A and D11A. White, grey and orange non-carbonate fracture minerals of unknown affinity is observed in D11A.

Three fractures types are found in the granitoid samples (Table 6). Contraction fractures are represented by longitudinal splitting, shown by b in figure 14, and well displayed in core samples D9A and D5A (Fig. 11). The brittle shearing processes are represented by shear fractures (Figs. 15E–F). In sample D11B turquoise and light green epidote constitute the filling in wing-cracks (Fig. 15G). Figure 15G displays how wing/edge-cracks (yellow arrow), has formed on the edge of the fractures and created a secondary fractured zone along the main fractures. Brittle-ductile shearing is observed by the boudinage structure in sample D5B (Fig. 15B) and as bands in sample D2B (Fig. 15C).



*Fig. 15A.* Sample D9A shows a ductile-brittle shear band (white arrows) and one larger branching fracture (yellow arrow). The hematite grains have formed after both the plastic and the brittle deformation (red arrow).

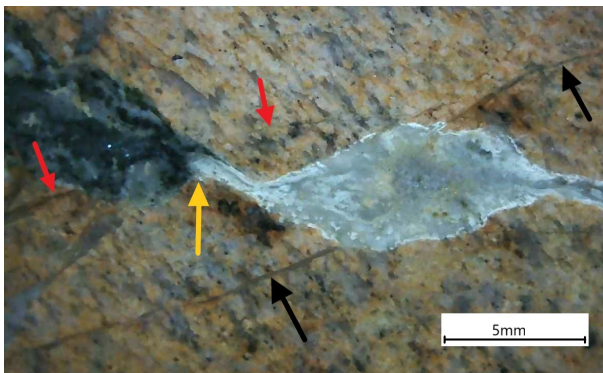


*Fig. 15B.* Three generations of fractures in sample D5A. First generation is a quartz-filled fracture (black arrows), intersected by the second generation, the boudinage structure (yellow arrow). The third generation intersects the boudinage structure in upper left corner (red arrows).

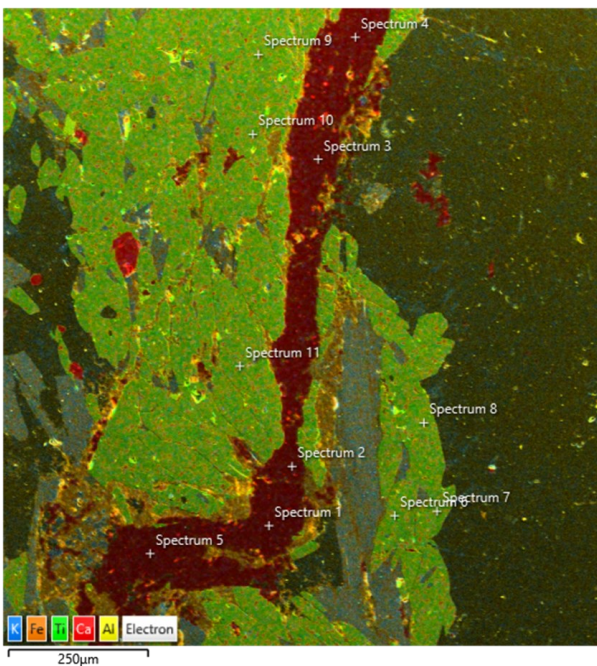


*Fig. 15C.* EDS-layered image of a plastically deformed calcite filled fracture (red) surrounded by titanite crystals (light green) in sample D2B.

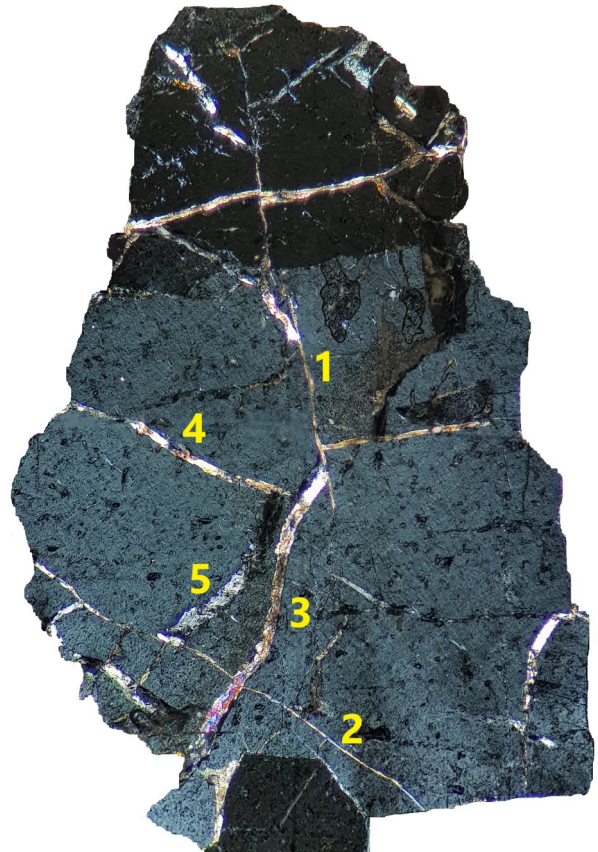


*Fig. 15D.* Microphotograph showing five generations of intragranular microfractures are marked by digits in sample D2B. The first generation, number one is the oldest fracture and number five is the youngest. The microfractures are filled by Mn-rich calcite. XPL-image, 10x.

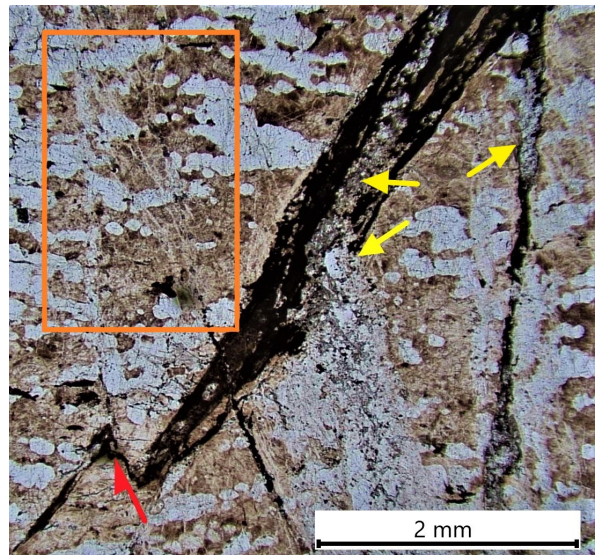


*Fig. 15E.* Microphotograph of secondary formed fractures intersecting the large dark filled fracture displayed in sample D6B. Red arrow marks a shear fracture. The yellow arrows point out secondary formed filling material. Within the orange square unfilled intragranular microfractures are branching from the filled fracture below.

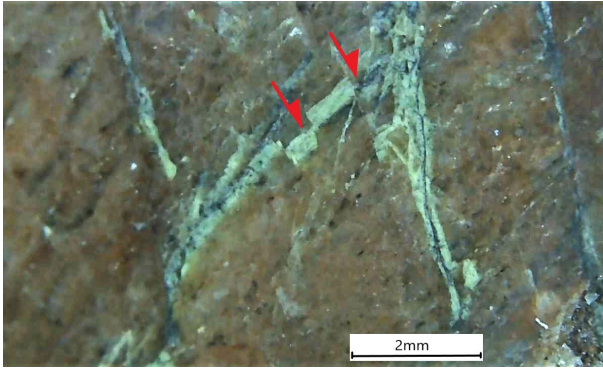


Fig. 15F. Conjugative shear fractures in sample D11A. The red arrows mark two sheared planes.

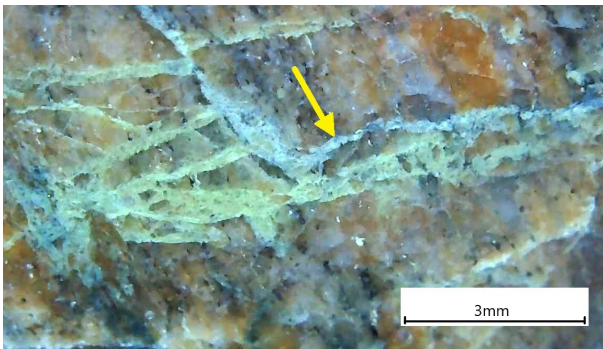


Fig. 15G. Wing-cracks (yellow arrow) in sample D11A.

#### Density and thermal conductivity

The density on the analysed gneiss samples from Dalby varies between 2.58g/cm<sup>3</sup> (sample D30D) and 2.67g/cm<sup>3</sup> (sample D23D). The average density for gneiss is 2.61g/cm<sup>3</sup> (Table 7). This relates well with data from the property database at SGU for comparable felsic rock on the Romeleåsen horst.

Felsic rocks usually present a higher conductivity than mafic rocks. This is mainly related to the higher content of quartz which have a higher thermal conductivity in comparison to the mafic minerals such as

Table 7. Compilation of the density for three different rock types from Dalby quarry. The density is given in kg/m<sup>3</sup>. The analysis has been performed by the Geological Survey of Sweden.

Sample	Rock type	P (g)	Volume (cm <sup>3</sup> )	Density (kg/m <sup>3</sup> )
D19D	Gneiss	685.1	261.77	2617.17
D20D	Gneiss	490.69	187.1	2622.55
D21D	Gneiss	802.1	306.23	2619.25
D22D	Gneiss	789.4	301.77	2615.87
D23D	Gneiss	1253.2	469.64	2668.43
D24D	Amphibolite	1197.5	401.1	2985.52
D25D	Amphibolite	671.7	228.8	2935.78
D26D	Amphibolite	953.2	326.55	2918.97
D27D	Amphibolite	539.83	186.24	2898.53
D28D	Gneiss	394.44	151.85	2597.5
D29D	Gneiss	330.98	127.13	2603.39
D30D	Gneiss	557.1	215.93	2579.98
D31D	Amphibolite	365.51	123.87	2950.81
D32D	Amphibolite-gneiss	273.17	98.37	2777.06
D33D	Diabase	442.91	147.42	3004.31
D34D	Amphibolite	650.3	219.64	2960.76
D35D	Gneiss	192.42	74.42	2585.64
D36D	Gneiss	293.2	112.79	2599.62

hornblende. The thermal conductivity for gneiss varies between 3.23 and 3.58 W/mK, giving an average of 3.47 W/mK (Table 8).

Table 8. Thermal conductivity data on outcrop rocks from Dalby quarry, given in (W/m K). The samples are collected from wall A-G in the quarry. The analysis has been performed by the Geological Survey of Sweden.

Sample	Rock type	Thermal conductivity (W/mK)
D1T	Gneiss red, fine, foliated	3.55 ± 0.10
D2T	Gneiss red, massive, fine, granitic	3.23 ± 0.10
D3T	Gneiss red, medium foliated, biotitic	3.46 ± 0.10
D4T	Gneiss light red-grey, fine	3.58 ± 0.10
D5T	Gneiss red, medium-weakly foliated	3.52 ± 0.10
D8T	Amphibolite/Metabasite	2.16 ± 0.10
D16T	Amphibolite/Metabasite	2.38 ± 0.10

#### 4.1.2 Mafic rocks

The mafic rocks are divided in two sections; a) metabasite/amphibolite b) diabase. The subdivision of amphibolite and metabasite is based on color and composition. The amphibolites are black and rich in hornblende and garnet. The metabasite classification applies to less black mafic rocks, rich in feldspar, poor in hornblende and lacking garnet.

##### a) Metabasite/amphibolite

The following description is based on four polished core samples (Fig. 16), four thin sections and SEM-EDX analyses. The cores D1A, D7A and D10A are classified as amphibolite since they are dominated by hornblende and plagioclase while core D2A is classified as a metabasite. Metabasite is commonly used as a collective term when the mineralogy and original texture is lost due to recrystallisation. Figures 17A-H microphotographs exemplifies the mineralogy of the mafic amphibolite and metabasite from Dalby.

#### Mineralogy and texture

The grey to blackish amphibolite/metabasite rocks are dominantly fine-grained, one sample, D7A, is very fine-grained. All samples are melanocratic/mafic, with colour index varying from M=70 to 85. Feldspars, amphibole and biotite dominate the mineral composition (Table 9). The mineral composition, i.e., the modal composition, of the investigated samples is calculated in percent based on results from the point counting. The amphibolite mineral composition of sample D7A is exemplified in figure 17A. The feldspar consists mainly of plagioclase however, K-feldspars are observed in samples D1A and D10A. The biotite and amphibolite content in the metabasite sample D2A hasn't been possible to calculate due to high degree of recrystallization (Fig. 17B), which has made it impossible to distinguish the minerals by optical microscopy merely.

Diamond-shaped titanite/sphene crystals occurring scattered in the groundmass are observed in sample D2A. The brown-black titanite constitute approximately 1% of the minerals in this sample. The D1A sample also contain titanite aggregates are also found

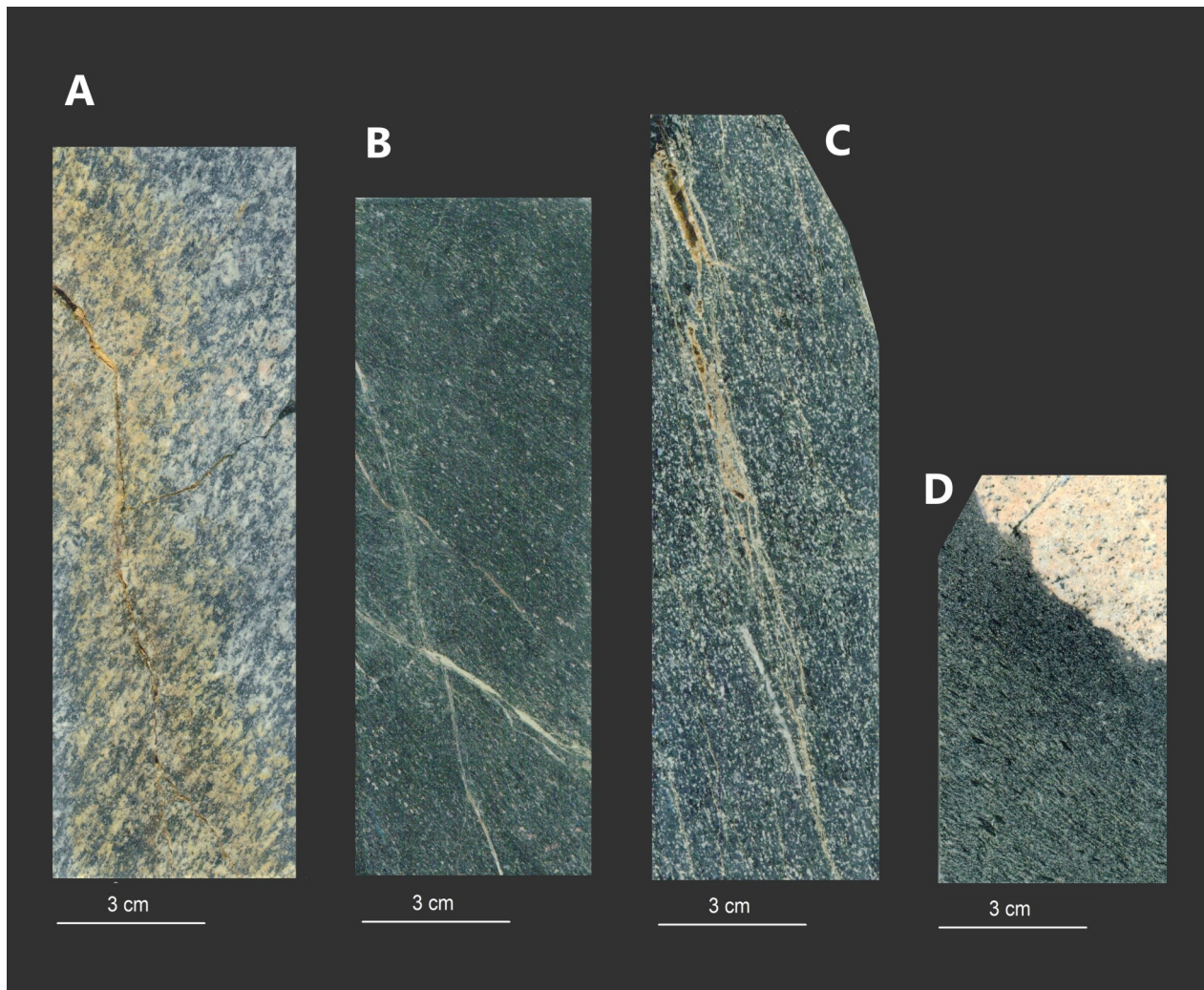


Fig. 16. Photographs of polished core slabs of amphibolite core samples from Dalby quarry. (A): sample D1A; fine-grained amphibolite. (B): sample D7A, a very fine-grained amphibolite. (C): sample D10A is a fine-grained garnet amphibolite. (D): lower part of sample D2A is a fine-grained metabasite core. Photo: H. Kervall.

in the D1A sample associated to opaque minerals and vugs. A few percent of opaque unidentified phases are observed in samples D1A, D2A and D7A. Sample D1A and D10A contains quartz (Table 9). Small crystals of garnet are found as accessory mineral in sample D10A, which also holds < 2 mm-sized hematite/magnetite and traces of pyrite and chalcopyrite. The chemical signature of D1A indicates presence of the phosphate flour apatite and ilmenite, both minerals appearing as anhedral crystals (Figs. 17C-D). In sample D10S pyrite is present, indicated by the SEM-layered image (Fig. 17E).

All mafic samples contain fine-grained interlocking crystals. The amphibolite sample D1A shows recrystallisation, of pyroxene into amphibole (Fig. 17F) and well-developed saussuritization texture (Fig. 17C). Sample D1A also contains zonations around mafic lenses, expressed by colour variation from core to rim (Fig. 17G). Sample D1A and D10A display a foliated fabric with continuous cleavage, defined by elongated biotite and hornblende and a light-colored Fe-rich mineral (Fig. 17H). D1A display a combined foliation, whereas the sample D10A is anisotropic. Sample D7A displays a mylonitic foliation, characterized by distinct grain size reduction (Fig. 16B), and

thin foliation banding and porphyroclasts (Fig. 18A).

The metabasite sample is characterized by recrystallization (Fig. 17B). The metabasite is furthermore foliated, giving a mylonitic appearance (Fig. 16D). The foliation is isotropic, but anisotropic by the contact to the granite, where the orientation of the crystals coincides with the transition angle between the two rocks. The foliation is generally expressed by biotite streaks.

#### Fractures

The amphibolite samples display a wide range of fracture widths (Table 10). In figures 18A–G several photo illustrations of fracture types and fracture fillings observed in the Dalby mafic rocks amphibolite and metabasite are displayed.

The largest fracture with an aperture (width) of < 3 mm is a partly open fracture in the garnet-amphibolite sample D10A (Fig. 18B). Most fractures are filled, independent of size. However, it is not uncommon, that filled, unfilled and partly unfilled fractures are displayed together (Fig. 18C). Branching fractures are also common independent of fracture size (Figs. 16B and 18C).

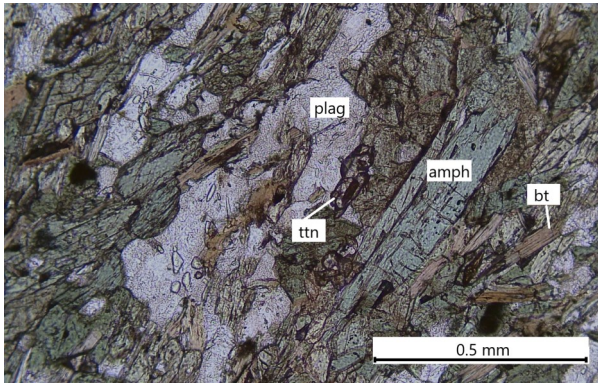


Fig. 17A. Microphotograph of mineral composition of amphibolite, sample D7B. Plagioclase (plag), biotite (bt), amphibole (amph) and titanite (ttn). PPL-image, 10x

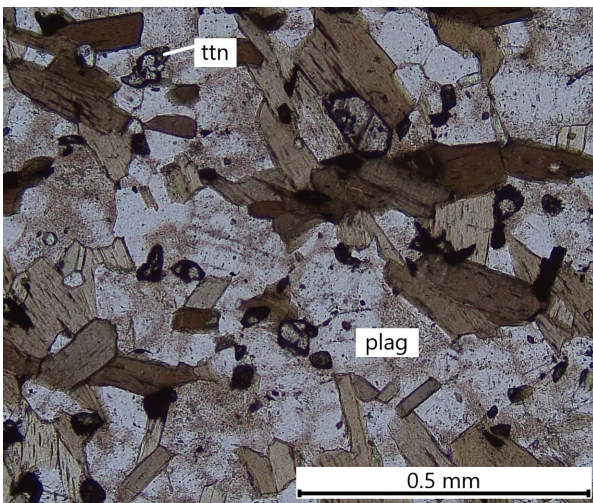


Fig. 17B. Microphotograph showing mineral composition of metabasite, sample D2B in PPL, 10x. Titanite (ttn) crystals are scattered in a groundmass of altered plagioclase showing saussurization texture. The brownish minerals represent biotite and amphibole.

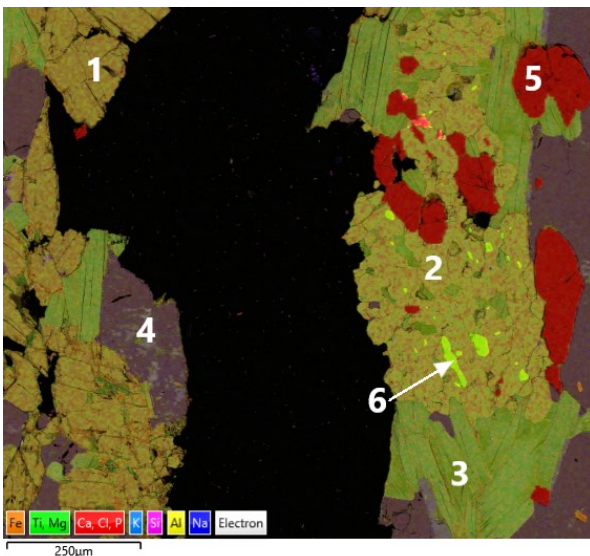


Fig. 17C. EDS-layered image, sample D1B. The coloured minerals around the vug have the chemical signature of: hornblende (1), titanite (2), biotite (3), plagioclase (4) fluorapatite (5), ilmenite (6).

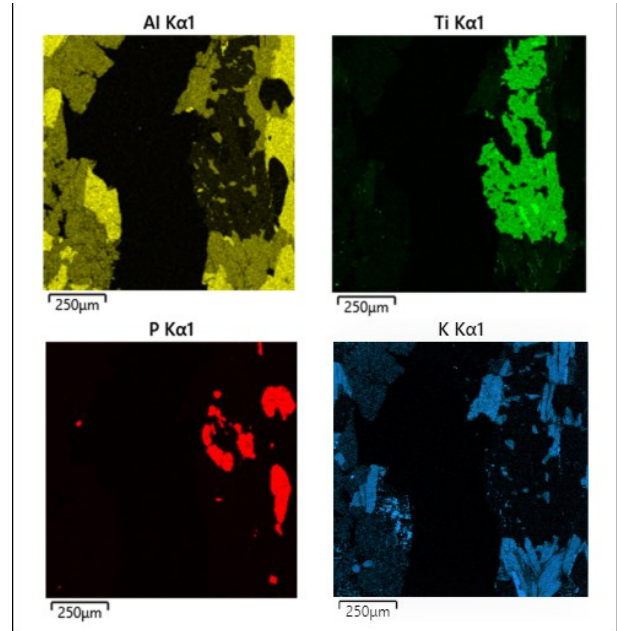


Fig. 17D. Element maps of sample D1B displaying the titanium (Ti) content in ilmenite and titanite. Potassium (K) is visualised mainly in the feldspar. Apatite is the only phosphorus-containing mineral in the image.

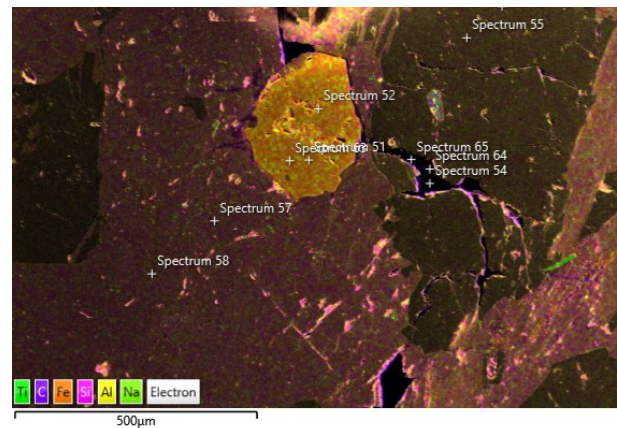


Fig. 17E. SEM-layered image. Pyrite surrounded by hornblende (pink) and bytownite, plag. (beige). Sample D10B.

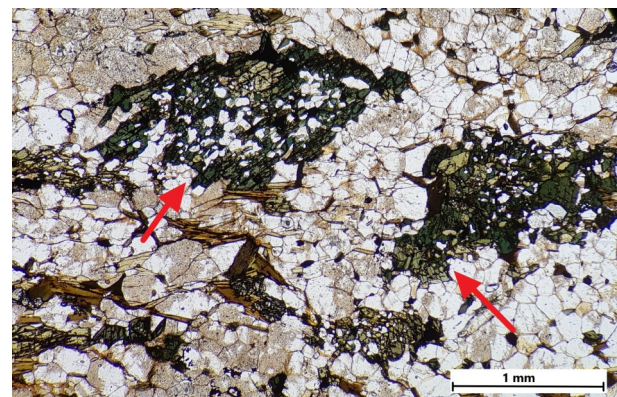


Fig. 17F. Microphotograph of recrystallised fabric in sample D1B. Deep green areas (red arrows) remains of a large pyroxene crystal. Within the crystal parts have been replaced by amphibole, light green colour (yellow arrow). PPL-image, 4x.

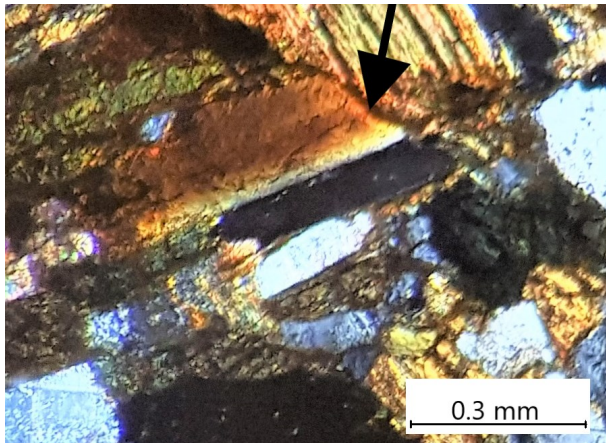


Fig. 17G. Microphotograph presenting a zoned mafic mineral (black arrow) in sample D1B.

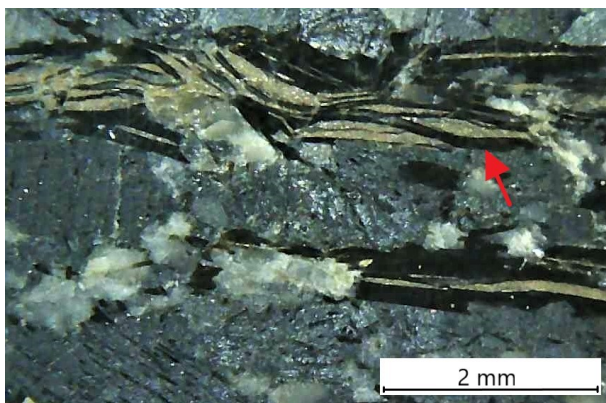


Fig. 17H. Plastically deformed hornblende grains (red arrow) in sample D10A.

All three fracture types are displayed in the amphibolite samples. Contraction is displayed by the vertical fractures seen in D1A (Fig. 16A) and D10A (Fig. 16D). Shearing is displayed in sample D7A and in D10A as wing-cracks. One type of shearing, where two sheared planes are displayed, forming a wedge between the contacts is seen in sample D10A (Fig. 18D). No fractures have been identified in the metabasite, sample D2A (Fig. 16C).

The chemical signature of the fracture fillings varies greatly in the samples, both within each sample and between samples (Table 10). This chemical variation is also displayed between fillings in bigger and smaller fractures as well as, between different generations of fractures (Figs. 18C and 18E). In sample D10A biotite is abundant in the whole rock, but seems to be enriched around the fractures, embedded by a Fe-rich mineral (Fig. 18B). Besides quartz, sample D10A contains unidentified fillings, some of the Cl-rich indicated by the SEM-EDX. In sample D7A all larger fractures have a light yellowish, pink and white carbonate filling, while the microfractures contain micro-/cryptocrystalline quartz and a dark unidentified mineral. In sample D1A the observed microfractures are filled with chlorite and Fe-rich components (Fig. 18C), a white coloured mineral, and a rosette-forming glassy and translucent brown and greenish mineral (Fig. 18F). The latter is giving a chemical signature of chlorite on both green and brown parts by the SEM-EDS. Sample D1A shows a dark red to black coloured mineral in and around the grain boundaries (Fig. 18G). The filling/precipitation has an Fe-reddish color and might be filled microfractures (L. Johansson, personal communication May, 2021).

Table 9. Summary of the point-counting results of the mafic core samples from Dalby. The mineral composition is given in percent by the three most dominant minerals. Accessory minerals constituting < 1%, are only noticed by name, so are the trace components. Note also that the point counting represents the thin section, and not necessarily the whole core.

Sample	Rock type (defined by texture)	Colour-index (M)	Fsp (%)	Bt (%)	Amp (%)	Accessory minerals	Trace components
D1A	Amphibolite	70	65	7	25	quartz, titanite, opaque (<1%)	flourapatite, ilmenite
D2A	Metabasite	80-85	45	yes	yes	opaque (<4%) titanite	apatite
D7A	Amphibolite	85	26	14	55	opaque (4%)	no
D10A	Garnet-amphibolite	80	30	16	54	quartz, garnet	pyrite/chalcopyrite, hematite/magnetite

Table 10. Display fracture types and fillings that occur in fracture >0.2mm and <2 mm in the Dalby mafic cores. The first column state if several generations of fractures have been identified. Fracture fillings are presented as well as occurrence of open fractures. For fracture types that display more than one type of fracture, the types have been ranked in the order they occur, from the most, to the least abundant type. The same ranking system have been applied to the fracture filling minerals.

Sample	Several generations of fractures	Larger fractures (>0.2mm)			Minor fractures (<0.2mm)		
		Fracture type	Fracture filling	Open fractures	Fractures undefined	Fractures filling	Open fractures
D1A	yes	contraction, extension	chlorite. Unidentified yellow, white, dark	yes	yes	iron hydroxide (FeOOH)/hematite, Mn-oxide. chlorite. white unidentified	yes
D2A	no	-	-	no	no	-	no
D7A	yes	shear	calcite, light yellow, white, pinkish- all calcareous	no	yes	quartz. dark unidentified	no
D10A	yes	shear, contraction	quartz; white-yellowish	yes	yes	unidentified Cl-rich	no

The precipitation seems to occur along grain boundaries, as well as intersecting single grains (intragranular) and several grains, (transgranular) (Fig. 18G).

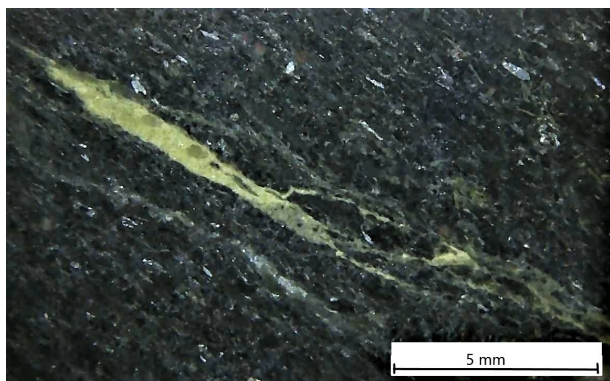


Fig. 18A. Mylonitisation, presented by a light yellow coloured calcareous foliation in sample D7A.



Fig. 18B. Open fracture in sample D10A with secondary formed quartz (yellow arrows).

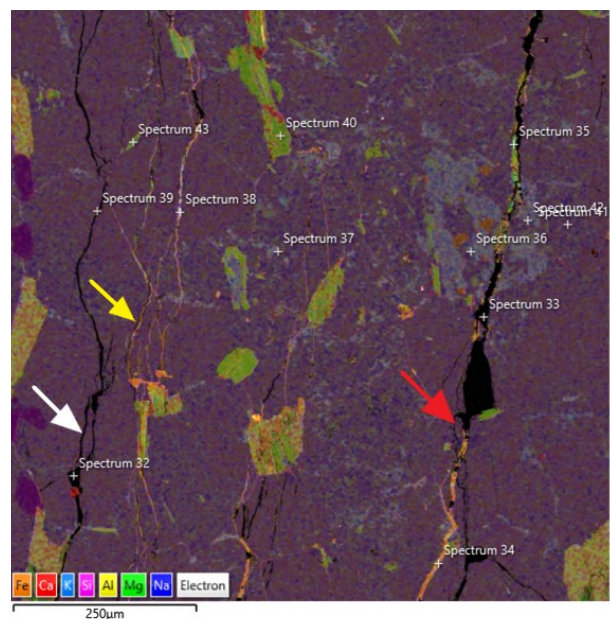


Fig. 18C. EDS-layered image from sample D1B presenting branching appearance of unfilled- (white arrow), filled- (yellow arrow) and partly filled microfractures (red arrow).

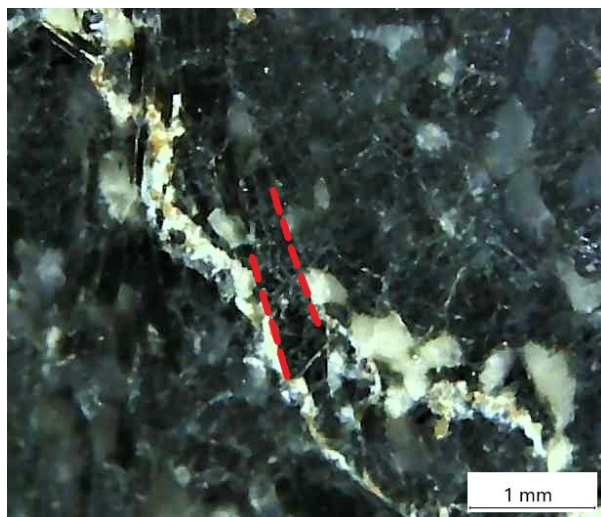


Fig. 18D. Filled fracture in sample D10A. Two red lines are plotted in the image where sheared planes are forming a wedge that has been pushed down between the contact surfaces.



Fig. 18E. Microphotograph of deformed fracture in sample D7B, where two different fillings run parallel to each other (red and white arrow). Upper filling (yellow arrow) and middle filling (red arrow) are both calcite.

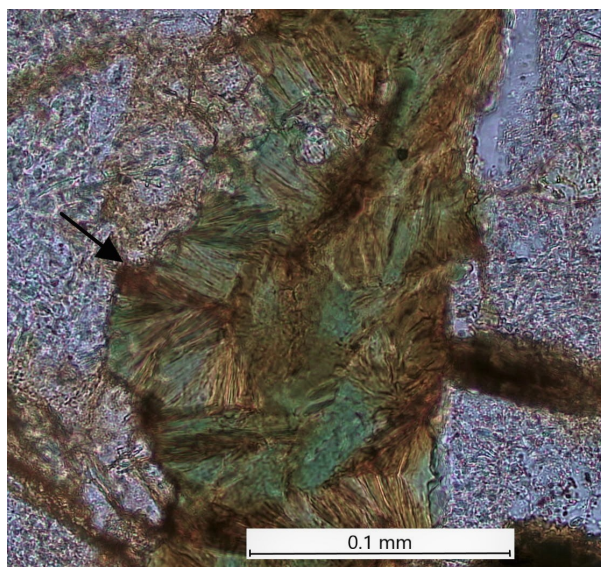


Fig. 18F. Microphotograph of rosette-like crystals in sample D1B with at chemical similarity of chlorite. PPL-image, 40x.

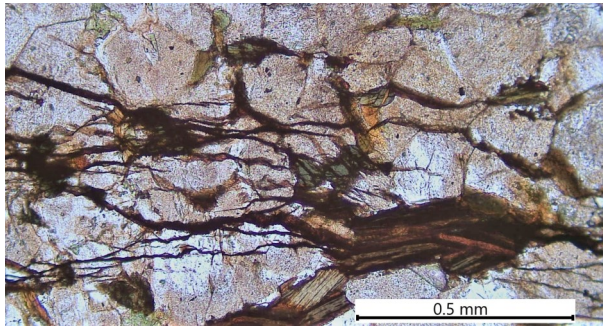


Fig. 18G. Microphotograph of sample D1B display what is likely to be foliation or filled microfractures.

#### Density and thermal conductivity

Data from the density and thermal conductivity analysis on the mafic cores from Dalby are presented in the felsic granitoid rock section. Density analysis have been performed on seven samples; six amphibolite samples and one amphibolite-gneiss sample. The data is presented in Table 7. The density of amphibolite varies between 2.89 g/cm<sup>3</sup> (sample D27D) and 2.98 g/cm<sup>3</sup> (sample D24D), giving an average of 2.94 g/cm<sup>3</sup>.

Thermal analysis has been performed on two amphibolite samples. The amphibolite/metabasite thermal conductivity varies between 2.16 W/mK (sample D8T) and 2.38 (sample D16T) W/mK (Table 8), giving an average thermal conductivity of 2.27 W/mK.

#### b) Diabase

The following description is based on the polished core sample D4A (Fig. 19), one thin section and SEM-EDX analyses.



Fig. 19. Polished core slab of a microcrystalline dark diabase. Dalby core sample D4A. Photo: H. Kervall.

#### Mineralogy and texture

Diabase is the less abundant rock in Dalby, only occurring as intrusions. The dark grey aphanitic rock is compact, microcrystalline and melanocratic/mafic with a colour index of M=75 (Fig. 19). The rock is composed of interlocking crystals of >50% plagioclase, c. 40% pyroxene and <10% opaque minerals (Fig. 20A). Ilmenite (FeTiO<sub>3</sub>), as indicated by SEM-EDS analysis, is commonly occurring as scattered minerals in the matrix of the rock.

The rock is homogenous and isotropic, meaning that the mineral composition is the same all through the rock and no preferred orientation of the minerals can be observed (Fig. 20A).

The texture is typically ophitic, with anhedral crystals of pyroxenes filling up the gap between the euhedral plagioclase needle-like crystals (Fig. 20A). Zonation projected from rim to the centre is displayed in figure 20B. Polysynthetic lamellar twinning (albite twin law) as well as simple twinning; penetration twinning in orthoclase or possibly contact twinning in the K-feldspar, are observed. Simple twinning is displayed in figure 20B. Some of the feldspar grains present intergrowth, i.e., perthite or antiperthite texture.

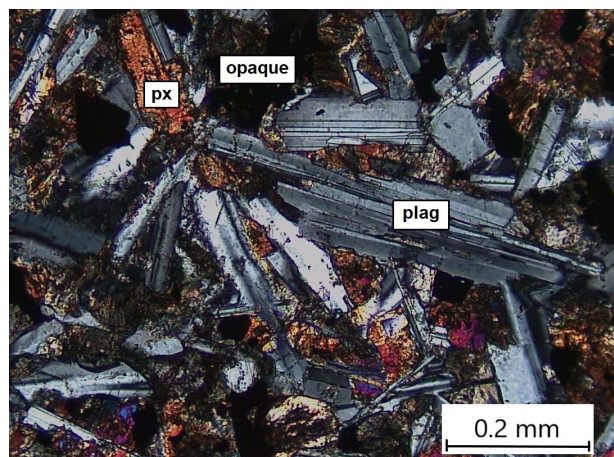


Fig. 20A. Microphotograph of the diabase composition, given by plagioclase (plag), pyroxene (px) and an unidentified opaque phase. Note the randomly oriented crystals and the ophitic texture. Sample D4B.

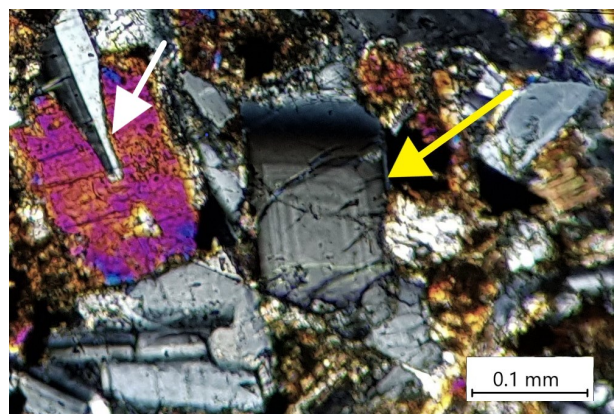


Fig. 20B. Microphotograph of zoned mineral in sample D4B. Zonation projected from rim to the centre (yellow arrow). White arrow marks an orthoclase grain displaying simple twinning.

### Fractures

The sample displays several types of fractures. Four primary fractures cut through the core at a 45-degree angle and from these, secondary fractures branch out (Fig. 19). All the fractures observed to the naked eye are judged to be formed by brittle deformation. The fractures are variably filled with fracture minerals. Parts of the fractures are also open. The fillings are predominantly composed of different types of carbonate minerals. A carbonate zonation of a fracture is exemplified in figures 21A and 21B. The zonations run characteristically parallel to the fracture plane. However, in figure 21B shearing features in the form of sigmoidal features in the brownish zonation are displayed within the fracture filling. The fracture fillings are assessed to consist mainly of calcite and magnesium-iron rich pyroxene (Fig. 21B). The fracture also contains black mineralisation, most likely organic matter (Fig. 21A).

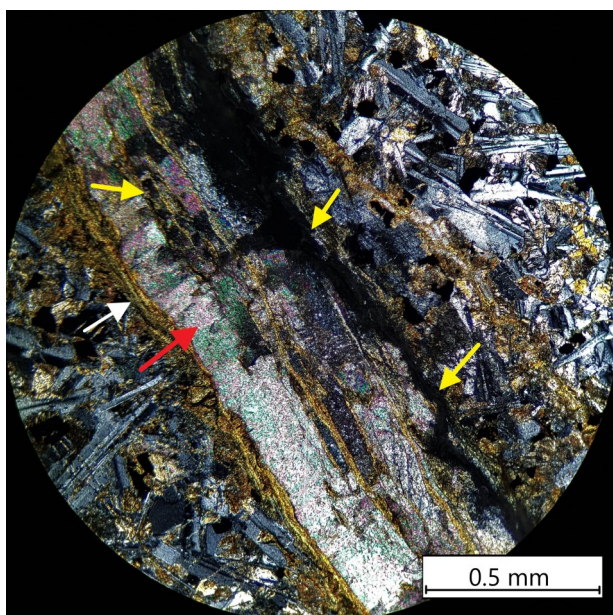


Fig. 21A. Microphotograph of banded fracture in sample D4B. The golden banding (white arrow) is rich in magnesium and iron, giving a chemical indication of pyroxene by the EDS-analysis. The white-pastel coloured filling is calcite (red arrow). The black precipitation is most likely organic matter (yellow arrows).

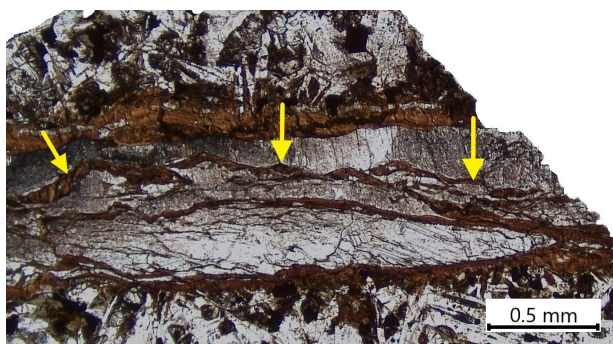


Fig. 22B. Microphotograph of banded fracture filling in D4B. Yellow arrows marks sigmoidal deformation features. The brown banding corresponds to the golden filling in figure 21 A. Fracture width measure 0,6mm. PPL-image, 4x.

### Density and thermal conductivity

Data from the density analysis on the mafic cores from Dalby are found in the felsic granitoid rock section. The density analysis on only one sample (sample D33D) gives a value of  $3.0 \text{ g/cm}^3$  which is in the same density range as for the amphibolites. No thermal analysis was performed on the diabase sample due to that the core was not large enough for an analysis.

## 4.2 FFC-1

The investigated cuttings from E.ON:s FFC-1 borehole display the same type of dominant rock groups as in Dalby i.e., 1) felsic granitoid rocks (primarily gneiss), 2) mafic rocks (amphibolite and metabasite). No diabase was encountered in the FFC-1 borehole. The following text focuses on describing the main characteristics, exemplified by a selection of photographs and illustrations. For the mineralogy- and texture descriptions focus have been placed on the cutting samples and their respective thin sections, presented in Table 4. The fracture description for the FFC-1 rock suites is less comprehensive since the observations are merely based on cuttings material.

### 4.2.1 Felsic granitoid rocks

The following description is based on detailed description and analysis of 12 cuttings samples representing different felsic rocks and depths in the FFC-1 borehole (Fig. 22). In figures 23A–H photo illustrations of the mineralogy observed in the felsic cuttings from FFC-1 is presented.

### Mineralogy, texture and chemistry

Just as in Dalby quarry, various types of gneisses are the most common rock type in FFC-1. These deep red and red to red-grey and grey rocks are predominantly fine-grained with varying gneissic texture (Fig. 22). The rock is mainly composed of interlocking crystals of potassium feldspar, plagioclase and quartz (Fig. 23A). The deep red varieties generally show a higher amount of potassium feldspar, while the greyish types are usually richer in biotite and plagioclase and the light-coloured varieties have a higher amount of quartz. Sample M6TS (Fig. 22L) present a specifically high amount of quartz, of 30–40%. Other minerals found in the gneisses are biotite and muscovite. Biotite, which is present in all but two of the deep red samples (M1TS and M2TS) occurs scattered, or defining banding. The muscovite occurs as scattered grains and as larger flakes. A muscovite-rich gneiss section is found at 2626–2649 m depth, with a peaking muscovite-content of 25% at 2629–2632m depth (Fig. 23B). Unidentified opaque phases are observed in half of the samples. In sample M8 and M9 anhedral and skeletal 0.1–0.5 mm large crystals of garnet are present, distinguished by the mineral's high relief (Fig. 23C). In sample M1TS magnetite and Fe-oxyhydroxides occurs as trace components.

The samples show mainly anisotropic texture, however isotropic textures are occasionally found in some of the samples. It is impossible to determine whether the cuttings represent a homo- or heterogenous rock due to the small cuttings size.

Ten out of twelve samples show a perthitic/



*Fig. 22.* Illustration exemplifying different types of felsic cuttings material in FFC-1(A): sample M1TS deep red gneiss, 2186–2187m. (B): sample M2TS deep red gneiss, 2215m. (C): sample M12TS deep red gneiss, 3060–3068m. (D): sample M7TS red gneiss, 2944–2952m. (E): sample M4TS red-grey gneiss, 2434–2435m. (F): sample M5TS red-grey gneiss, 2853–2857m. (G): sample M9TS red-grey gneiss, 2950–2952m. (H): sample M14TS red-grey gneiss, 3060–3062m. (I): M16TS red-grey gneiss, 3129–3132m. (J): sample M13TS grey gneiss, 3060–3062m. (K): sample M8TS quartz-rich grey gneiss, 2948–2952m. (L): sample M6TS quartz-rich grey gneiss, 2853–2857m. Photo: H. Kervall.

antiperthitic texture displayed as lamellae (Fig. 23D) and blebs (Fig. 23E). Saussuritization as well as simple twinning of plagioclase is found in all samples, except M14TS (Fig. 23D). Potassium feldspar cross-hatched twinning, so called tartan twinning, is present in 75% of the samples (Fig. 23F).

A moderate grade of deformation is dominating the samples. In sample M4TS a higher grade of recrystallisation is presented, shown as remnants of mafic minerals, i.e., skeletal grains, from which quartz have started to form (Fig. 23G). Both brittle- and plastic deformation is observed. The plastic deformation is presented as banding on cuttings and by ductile fractures (Fig. 23H).

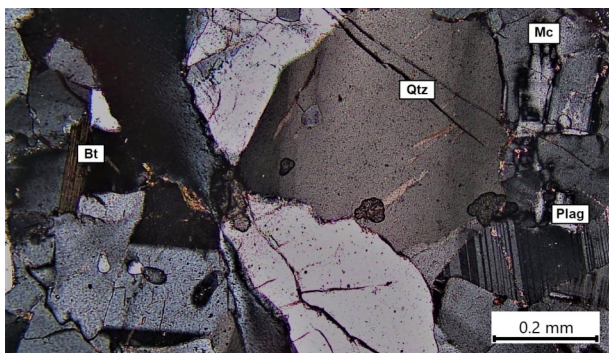


Fig. 23A. Microphotograph of mineral composition of sample M4TS; quartz (qtz), plagioclase (plag), biotite (bt), microcline (mc).



Fig. 23B. Muscovite flakes from depth 2629-2632 m.

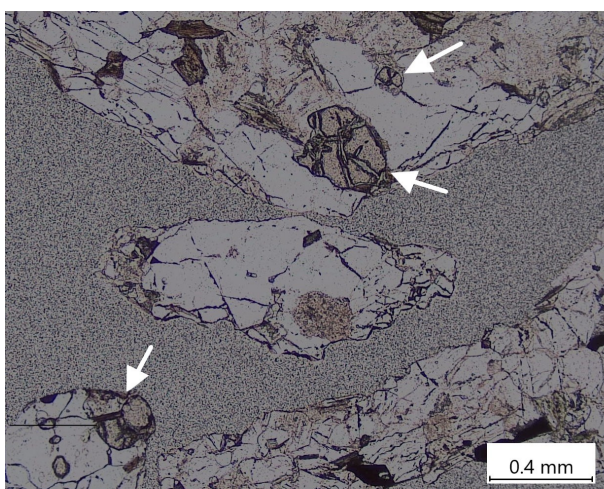


Fig. 23C. Three anhedral garnet crystals are displayed in the microphotograph, marked by the white arrows. PPL-image 4x of sample M9TS.

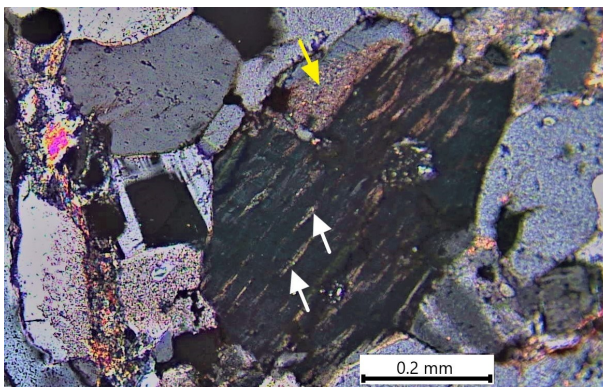


Fig. 23D Microphotograph of perthite/antiperthite in sample M1TS. White arrows mark the intergrowing exsolution lamellae. Yellow arrow marks saussuritization texture. XPL-image 10x.

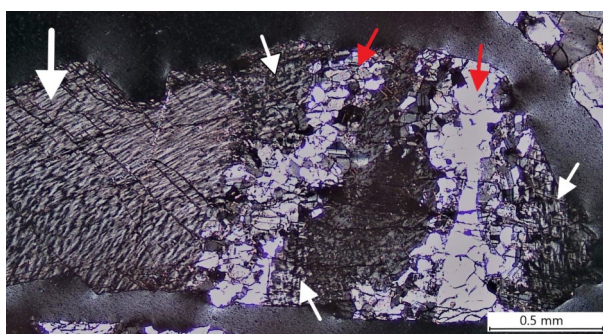


Fig. 23E. Microphotograph of perthite/antiperthite displayed in the shape of blebs in sample M12TS (white arrows). The red arrows marks quartz-filled fractures. XPL-image, 4x.

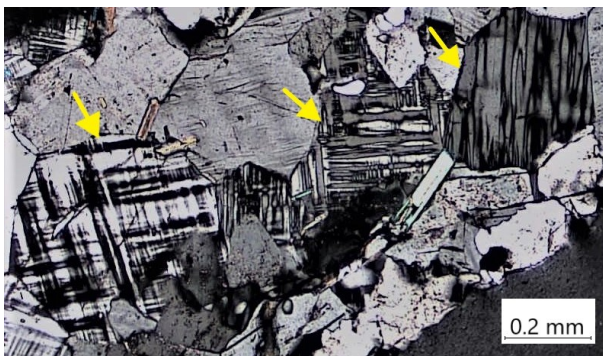


Fig. 23F. Microphotograph displays characteristic microcline tartan twinning (yellow arrows). XPL-image of sample M5TS, 4x.

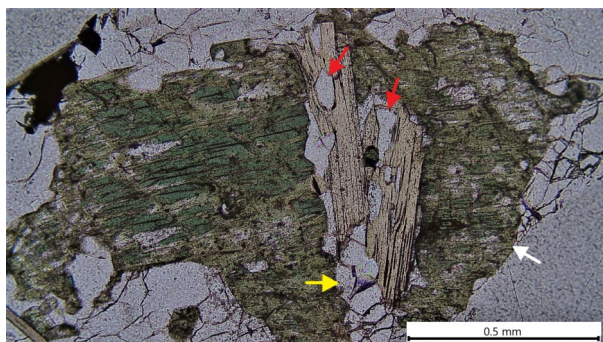


Fig. 23G. Microphotograph of recrystallisation in sample M4TS. White and red arrow marks remnants of mafic minerals. Yellow arrow marks quartz that has started to form.



*Fig. 23H.* Banding in felsic cutting, defined by dark elongated minerals and quartz.

### Fractures

Fractures, both larger and smaller than 0.2 mm wide, are present in the gneiss samples. In figures 24A–N fractures and fracture fillings observed in the FFC-1 felsic rock cuttings are presented. Fracture fillings seem to be more frequently occurring in larger fractures, but also some microfractures seem to be, at least partly, filled (Fig. 24A).

Cuttings from sample M7TS, M12TS and M14TS display fractures with light green-blue minerals (Figs. 24B–D). Other fracture mineral observed is an off-white, translucent or milky white material (Figs. 24E–F). Some of these minerals and materials are identified as calcite, but quartz seem to constitute the dominating filling mineral. The quartz is generally translucent or milky white, but also yellowish and light green variants are observed (Fig. 24G). Figure 24I illustrate a micro fracture filled with quartz. Both calcite and quartz also appear as larger euhedral crystals in the samples (Fig. 24G), free or attached to the wall of the vug where they have grown (Fig. 24H). A black fracture filling, or possibly foliation of elongated minerals, occurs parallel to other fracture fillings on scattered cuttings (Fig. 24E).

Transgranular as well as intergranular microfractures are also observed (Fig. 24J). In figure 24K two quartz grains display intragranular fractures, whereas one of the fractures partly contains fracture filling.

In figure 24L a ductile fracture is displayed. Several generations of fractures have not been observed in the samples. Sample M1TS and M12TS display a reddish precipitation, most likely iron-rich. It's presence is displayed as inter- and intra-granular pattern (Fig. 24M) as well as constituting the matrix in some cuttings (Fig. 24N).



*Fig. 24A.* filled fracture plane (white arrow) running through a cutting of gneiss.



*Fig. 24B.* Cutting from 2788 meters depth presenting a fracture plane coated by rather thick light blue-green mineral.



*Fig. 24C.* Cutting from 2702-2705 meters depth presenting a fracture plane where a blue-green mineral has formed.

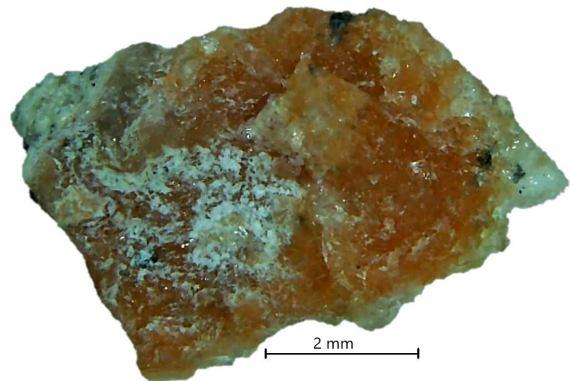


*Fig. 24D.* Cutting from 2702-2705 meters depth presenting a light green-blue mineral scattered over a part of the upper side.



*Fig. 24E.* Deformation of fracture displayed by elongated minerals in cutting.

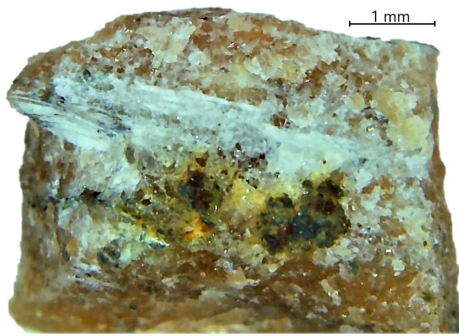


Fig. 24F. Off-white fracture filling intersects gneiss cutting. The yellowish color is a result of iron precipitation.



Fig. 24G. Yellow-greenish quartz grain from felsic sample.



Fig. 24H. Quartz grain formed in cavity. From sampled cuttings 2702-2705 m.

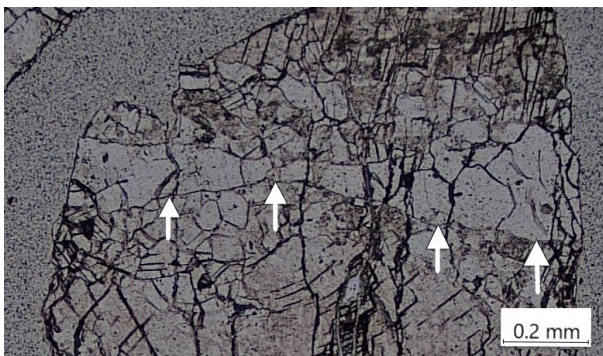


Fig. 24I. Microphotograph of quartz-filled fracture (white arrows) running through cuttings in sample M12TS, PPL-image, 4x.

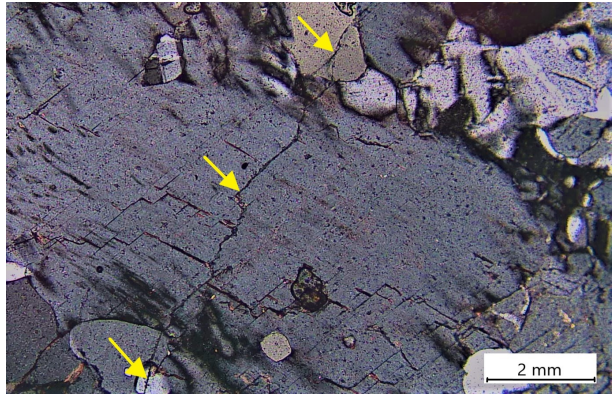


Fig. 24J. Microphotograph of transgranular microfracture (yellow arrows) in sample M2TS. XPL-image, 10x.

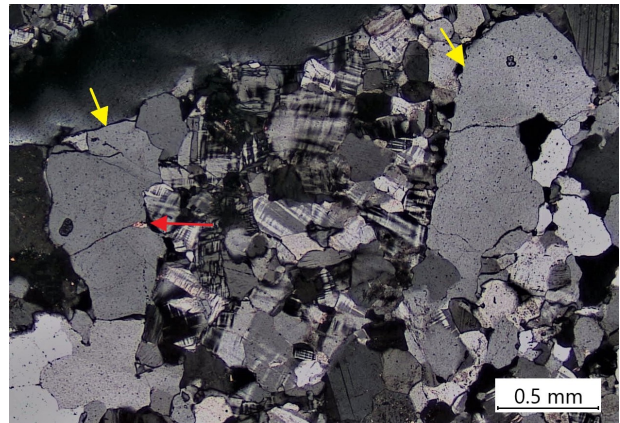


Fig. 24K. Microphotograph of two quartz-grain (yellow arrows) displaying several intra granular microfractures. Red arrow marks fracture filling. Sample M2TS, XPL-image, 4x.

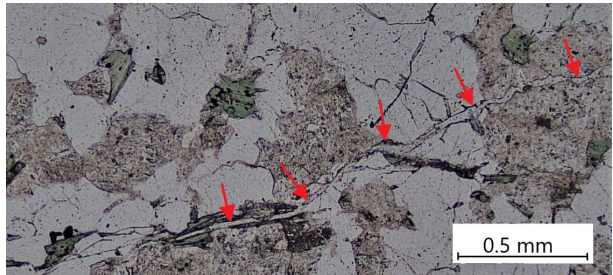


Fig. 24L. Microphotograph of partly filled and plastically deformed microfracture (red arrows) in sample M9TS PPL-image, 4x.

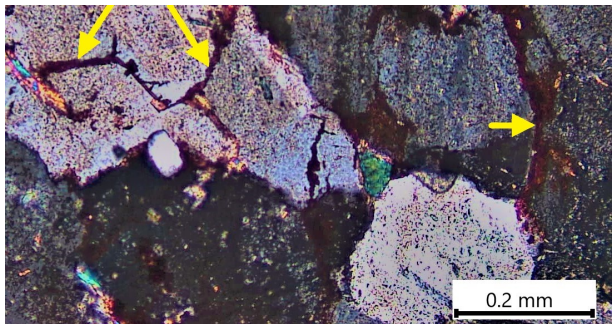


Fig. 24M. Microphotograph of dark red coloured precipitation located along grain boundaries, and intersecting the grains (yellow arrows). Sample M1TS. PPL-image, 10 x.

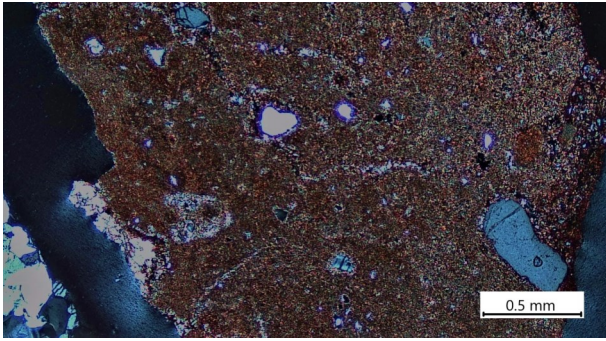


Fig. 24N. Microphotograph of sample M12TS iron-rich matrix. XPL-image, 4x.

### Geophysical log

The geophysical logs are important tools in characterising the bedrock (Fig. 10). The Caliper log physically measure the diameter of the borehole, and can therefore also assist in identifying fractures and weakness zones (MIT 2006). As displayed in the Caliper log (Fig. 10) the upper part of the crystalline bedrock down to c. 2450 m depth of FFC-1 is highly fractured.

Felsic and mafic rocks are distinguished as indirect reflections the SiO<sub>2</sub> content in the gamma ray log. In the spectral gamma ray log the signatures is separately displayed for the elements potassium (K), thorium (Th) and uranium (U). High signatures of potassium are related to higher amounts of potassium feldspar in the felsic rocks. Lower potassium feldspar signatures can be observed from c. 3000 m depth, where amphibolite dominates (Fig. 10). The density log is useful when interpreting rock, as mafic rocks usually present a higher density than felsic rock. This is displayed by the high-density values over the amphibolite-rich interval between 2300 m and 2330 m, and also deeper than 3025 m (Fig. 10). The density and the gamma ray log usually counteract each other as higher density rocks are usually low in quartz and vice versa.

Table 11. Table of density analysis performed on FFC-1 cuttings. Analysis performed by Klitzsch & Ahrensmeirs (2021).

Sample	Depth (m)	Rock Type	Matrix Density (AccuPyc) (g/cm <sup>3</sup> )	Matrix Density (TC samples) (g/cm <sup>3</sup> )	Density mean (g/cm <sup>3</sup> )
M1D	2771-2774	Gneiss quartz-rich	2.657 ± 0.002	2.57 ± 0.02	2.614
M2D	2873-2875	Gneiss	2.656 ± 0.002	2.59 ± 0.02	2.623
M3D	2954-2965	Gneiss/Granodiorite	2.694 ± 0.003	2.40 ± 0.02	2.547
M4D	3098-3100	Amphibolite/Metabasite	2.994 ± 0.003	2.92 ± 0.02	2.957
M5D	3104-3106	Amphibolite/Metabasite	2.969 ± 0.002	2.97 ± 0.03	2.970

Table 12. Presents thermal conductivity analysis (W/m K) of the FFC-1 cutting samples. Analysis performed by Klitzsch & Ahrensmeier (2021).

Sample	Depth (m)	Rock type	TC Matrix (W/m K)	@Temp. (°C)
M1T	2771-2774	Gneiss quartz-rich	3.85 ± 0.05	16.6
M2T	2873-2875	Gneiss	3.91 ± 0.06	16.8
M3T	2954-2965	Gneiss/Granodiorite	3.10 ± 0.03	17.2
M4T	3098-3100	Amphibolite/Metabasite	2.54 ± 0.02	16.4
M5T	3104-3106	Amphibolite/Metabasite	2.59 ± 0.02	18.7

### Density and thermal conductivity

Density- and thermal conductivity analyses have been performed on three gneiss samples from the FFC-1. As displayed in Table 11 the AccuPyc density method gives the best result regarding uncertainties, generally ten times smaller than the analysis performed on thin sections. The density (AccuPyc) displays very similar values for the three samples, with an average value of 2.67 g/cm<sup>3</sup>.

The results from the thermal conductivity are displayed in Table 12. The uncertainties vary between the samples (Table 12). The values also display a distinct variance; a difference of 0.81 W/mK, between the lowest value, displayed by sample M3T, and the highest value, displayed by sample M2T (Table 12). The average thermal conductivity value is 3.62 +/- 0.05 W/mK.

### Chemical composition

Chemical analysis was performed on seven gneiss samples, displayed in Table 13. The highest SiO<sub>2</sub>-value is 76.3%, given by the quartz-rich sample M4C, the lowest is 53.7%, given by M2C. The average difference between felsic and mafic samples in SiO<sub>2</sub> is 8,4%. Average values for the gneiss samples, given in weight % follows; SiO<sub>2</sub>: 70.2%, Al<sub>2</sub>O<sub>3</sub>: 14.43%, Fe<sub>2</sub>O<sub>3</sub>: 3.63%, CaO: 2.04%, MgO: 0.95%, Na<sub>2</sub>O: 3.2%, K<sub>2</sub>O: 4.48%, TiO<sub>2</sub>: 0.44%, MnO: 0.07%, P<sub>2</sub>O<sub>5</sub>: 0.08%.

### 4.2.2 Mafic rocks

The following description is based on amphibolite/metabasite cuttings from the E.ON FFC-1 borehole, with focus on four cuttings samples (Fig. 25), and corresponding thin sections. Figures 26A–G present photo illustrations of the mineralogy observed in the mafic amphibolite/metabasite cuttings.

Table 13. Compilation of the results from the chemical analysis of the main elements, (expressed as oxides in weight % of FFC-1 cuttings Analysis performed by ALS Geochemical AB Öjebyn.

Sample	Rock type	SiO <sub>2</sub>	Al <sub>2</sub> O <sub>3</sub>	Fe <sub>2</sub> O <sub>3</sub>	CaO	MgO	Na <sub>2</sub> O	K <sub>2</sub> O	TiO <sub>2</sub>	MnO	P <sub>2</sub> O <sub>5</sub>
M1C	<i>Amphibolite black</i>	49	15.7	13.6	8.26	5.86	2.39	1.13	1.85	0.18	0.26
M2C	<i>Gneiss grey</i>	53.7	16.25	11.3	6.41	4.33	2.46	1.61	1.54	0.16	0.25
M3C	<i>Amphibolite grey-black</i>	60.1	15.75	6.51	2.93	3.21	2.87	3.57	0.65	0.17	0.09
M4C	<i>Amphiolite black</i>	76.3	13.05	1.75	1.04	0.23	3.04	4.79	0.23	0.04	0.04
M6C	<i>Gneiss deep red</i>	73.7	13.85	2.18	1.06	0.22	3.91	4.69	0.25	0.02	0.04
M7C	<i>Gneiss red</i>	72	15.45	1.38	0.77	0.09	2.82	8.04	0.07	0.04	0.05
M8C	<i>Gneiss grey, quartz-rich</i>	77.8	12.4	1.49	0.71	0.1	3.11	4.93	0.11	0.02	0.02
M9C	<i>Gneiss grey, quartz-rich</i>	76.3	13	2.02	1.33	0.31	3.03	3.68	0.26	0.05	0.04
M10C	<i>Gneiss red-grey</i>	66.7	15.75	4.51	2.62	1.28	3.33	3.07	0.58	0.11	0.1
M11C	<i>Gneiss red-grey</i>	71.2	14.3	2.56	1.36	0.29	3.91	5.36	0.3	0.06	0.05

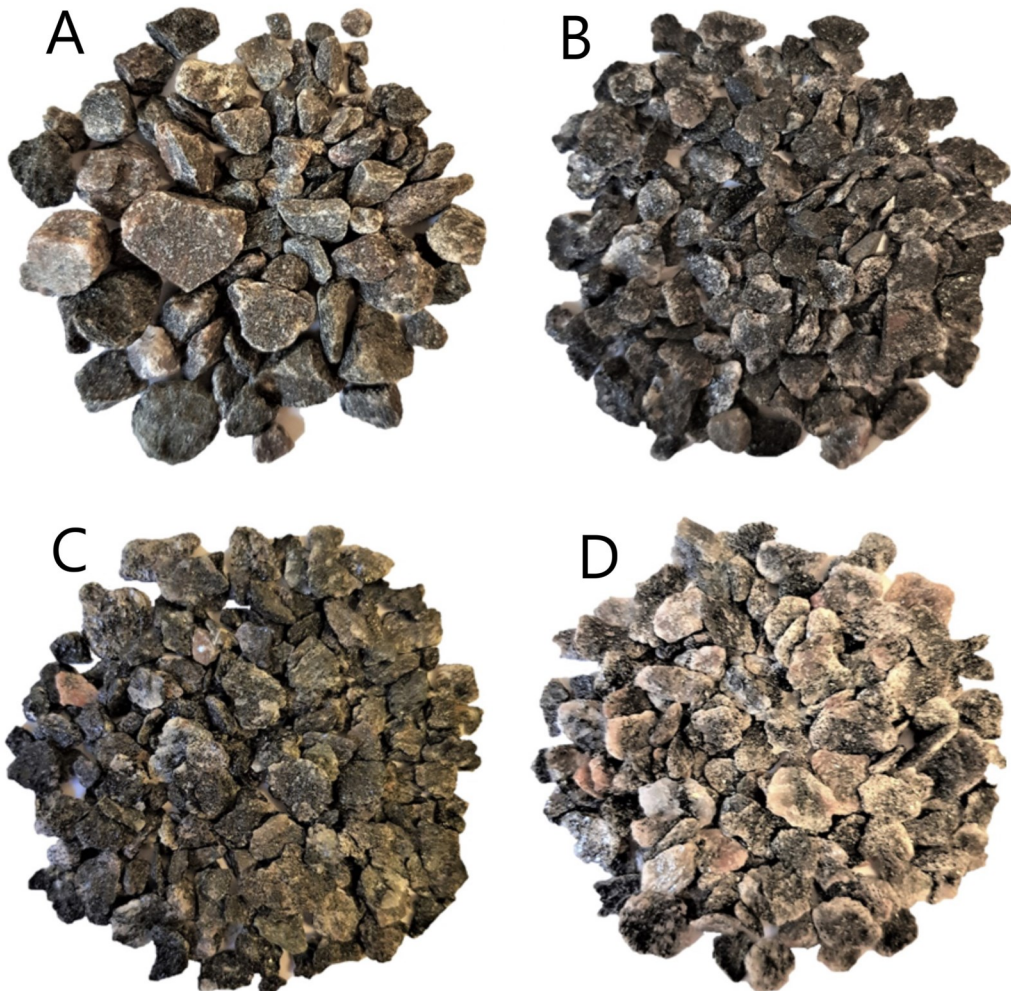


Fig. 25. Photographs exemplifying the FFC-1 mafic cutting samples. (A): sample M3TS black amphibolite, 2215m.. (B): sample M11TS black amphibolite, 3060–3062m. (C): sample M17TS black amphibolite, 3129–3132m. (D): sample M10TS grey-black amphibolite, 2950–2952m. Photo H. Kervall.

### Mineralogy and texture

The dark grey and blackish amphibolite/metabasite is dominantly very fine-grained, but both aphanitic and fine-grained cuttings are observed (Fig. 26A). Sample M3TS, M11TS and M17TS are melanocratic/mafic, with a colour index of approximately  $M=80$ . Sample M10TS has a colour index around  $M=65$  i.e., between mesocratic and melanocratic, still within the mafic area though. The rocks are characterized by interlocking crystals of feldspars, amphibole and biotite (Fig. 26A). Quartz is observed in all samples, except in sample M10TS where the content of quartz is significant (Fig. 26B). The feldspars almost exclusively consist of plagioclase. Merely a few potassium feldspar crystals have been observed in sample M3TS. All samples contain 0.1–0.8 mm sub- to anhedral garnet crystals (Fig. 26C). Small fragments of garnet crystals are also frequently observed. Sample M8TS is especially rich in garnet. Opaque phases are furthermore observed in all samples. Garnet and the opaque phases often occur together. Muscovite and galena are observed in M11TS. In sample M17 scattered crystals of calcite are displayed, giving the rock a speckled appearance. Garnet is also found to occasionally occur together with a green mineral, possibly clinopyroxene (Fig 26D).

Saussuritization of plagioclase is observed in all samples (Figs. 26B and 26E). In some of the cuttings of sample M11TS and M17TS the plagioclase occurs in needle shape (Fig. 26F). Single twinning on plagioclase grains is seen in all samples but M3TS, which is the only mafic sample displaying perthite/antiperthite texture (Fig. 26B) and tartan twinning. Plagioclase grains with zoned rims are present in M3TS and M10TS (Fig. 26E). Skeletal grains are observed in sample M11TS (Fig. 26G). The grade of deformation varies between the cuttings in the same sample, as can be seen when comparing the different cuttings displayed in figure 26A. The material also displays a variation on the homogeneity/heterogeneity as well as the isotropic/anisotropic texture. Oriented mineral grains of biotite and amphibole are observed in all samples (Fig. 26A).

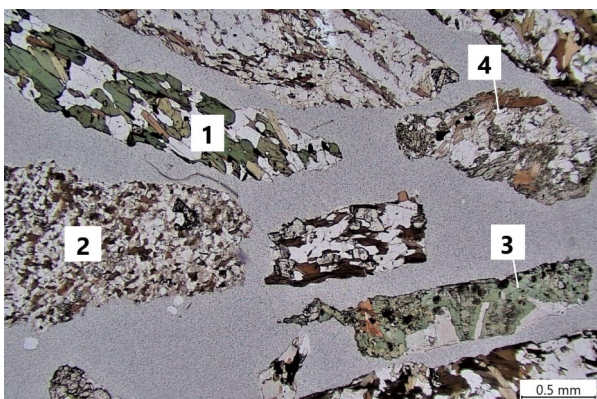


Fig. 26A. Microphotograph of cuttings from sample M17TS. Cutting no. 1 display very fine grained grainsize. The grains in cutting no. 2 are almost aphanitic ( $< 0.05$  mm). Cutting no. 3 presenting anhedral grains. The white/beige minerals are generally feldspar and the brown needle-like minerals are biotite. Cutting no. 2 display a homogenous texture. In cutting no. 4 heterogeneity is presented, PPL-image, 2x.

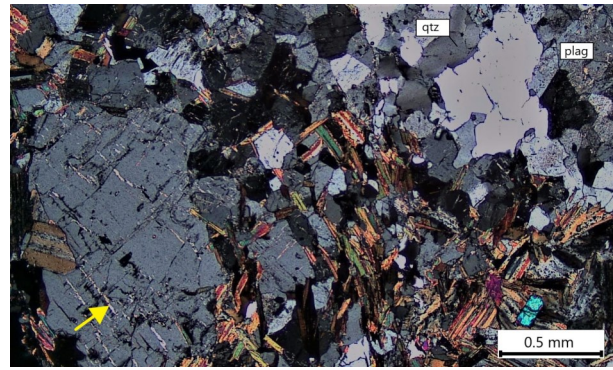


Fig. 26B. Microphotograph of composition in sample M3TS. Plagioclase (plag), quartz (qtz). The colourful minerals in the lower centre of the picture are most likely altered amphibole and biotite. The yellow arrow marks perthite/antiperthite texture. XPL-image, 4x.

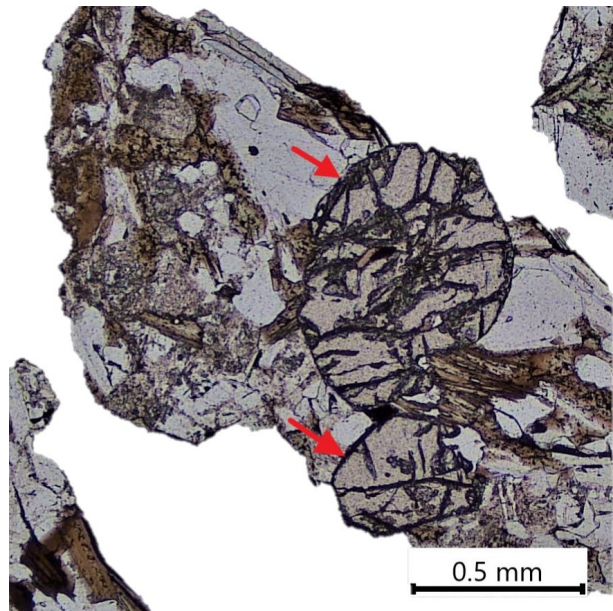


Fig. 26C. Microphotograph of subhedral garnet crystals (red arrows) in sample M10TS, PPL-image, 4x.



Fig. 26D. Cuttings from 2654-2660 m depth showing a green mineral rich in tiny dark red garnets (black arrow).

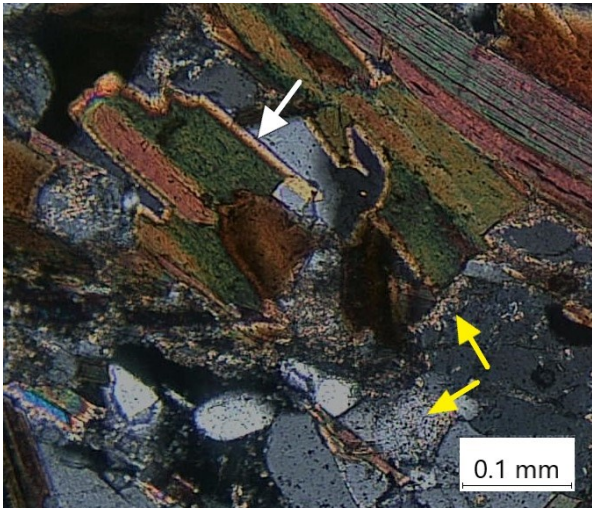


Fig. 26E. Microphotograph showing prominent margin zoning on mafic lens (white arrow). Yellow arrows show saussuritization texture on plagioclase. Sample M10TS. XPL-image, 2x.

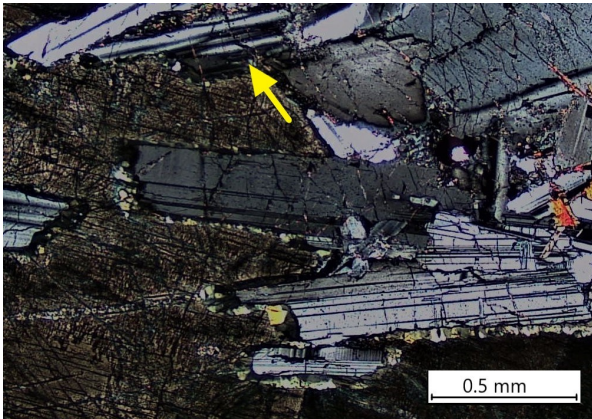


Fig. 26F. Microphotograph of plagioclase needles (yellow arrows) in sample M11TS. XPL-image, 4x.

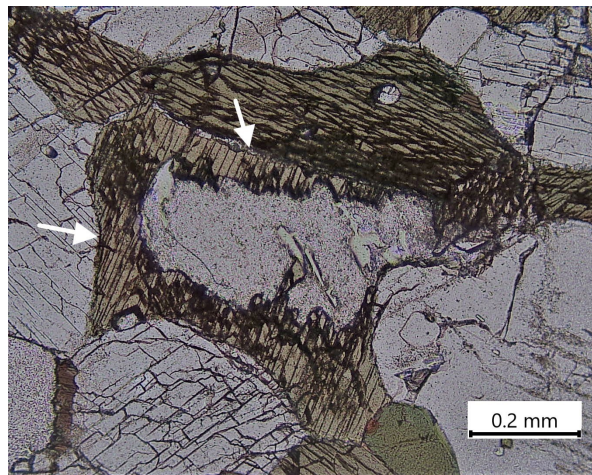


Fig. 26G. Microphotograph of sample M11TS. Recrystallization in skeletal grain. White arrows mark what is left of the rim. Note also the grain localised centrally in the upper part of the picture where initial recrystallization have started in a small hole.

### Fractures

No fractures are to be observed in the thin sections. However, sample M17TS contains a rather distinctive amount of scattered calcite crystals, not unlikely originating from a calcite fracture. On cuttings collected from other depths, fracture planes with fracture filling are frequently observed. Figures 27A–E display photographs on these cuttings exemplifying different fracture fillings observed in the FFC-1 mafic rocks. The fillings are light yellow or white, forming larger crystals as illustrated in figure 27A, or having a microgranular texture (Fig. 27B). It is not uncommon that the cuttings display a rusty colour due to iron precipitation, and then miscolouring the filling mineral. In figure 27C–E the contact between amphibolite and quartz veins are shown. In figure 27D it is further well displayed how a fracture in the quartz runs parallel to the contact.



Fig. 27A. Cutting of amphibolite from 2160 m depth. Red arrows mark light yellow crystals that have formed on the fracture plane. Compare with the clean freshly cut surface on the lower side of the yellow dashed line.



Fig. 27B. Light yellow microgranular mineral on a fracture plane on a cutting from 2210-2240m depth.



Fig. 27C. Two cuttings from 2946-2952m showing parts of a quartz vein.



Fig. 27D. Cutting from 2950-2952m showing the contact between amphibolite and a quartz vein. Note the fracture in the quartz (red arrow), that runs parallel to the contact.



Fig. 27E. Quartz veins running through amphibolite cuttings, from 2788 and 3060m depth.

#### Density and thermal conductivity

Data from density analysis on the mafic cuttings from FFC-1 are found in the felsic granitoid rock section (Table 11). Density analysis has been performed on two amphibolite samples and the results are similar; sample M4D, giving a density value of 2.99 g/cm<sup>3</sup> and M5D a value of 2.97 g/cm<sup>3</sup> (Table 11).

Thermal analysis on the same samples gives a thermal conductivity of 2.54 W/mK for M4T a value of 2.59 W/mK for M5T (Table 12).

#### Chemical composition

The chemical analysis of the three amphibolite samples gives a high SiO<sub>2</sub> of 77.8% for sample M8C, and a low of 49%, for the MIC sample. Average values for the amphibolite samples given in weight % follows; SiO<sub>2</sub>: 61.8%, Al<sub>2</sub>O<sub>3</sub>: 14.83 %, Fe<sub>2</sub>O<sub>3</sub>: 7.29%, CaO: 4.08%, MgO: 3.1%, Na<sub>2</sub>O: 2.77%, K<sub>2</sub>O: 3.16%, TiO<sub>2</sub>: 0.91%, MnO: 0.13%, P<sub>2</sub>O<sub>5</sub>: 0.13%.

## 5 Discussion

Based on results and descriptions presented in the previous chapter, the following text will be connecting to

a simulated construction of a deep-thermal plant in the crystalline basement and its geological prerequisites in SW Scania.

## 5.1 Bedrock composition

### 5.1.1 Minerology

The crystalline basement in FFC-1 is predominately composed of two type of rocks, felsic gneiss and mafic amphibolite/metabasite. This has been assessed based on the cutting descriptions, and further supported by the spectral gamma ray log, density and chemical analysis. In Table 15 the relative abundance of the rock types in DGE-1 and FFC-1, presented by Rosberg and Erlström (2021) has been compared with volume estimation based on descriptions of cores from the Dalby quarry. Values have been normalized as 3.7% of the DGE-1 cores was unidentified due to weathering and fracturing. What mainly differs is that diabase is present in the Precambrian basement on the Romeleåsen horst, but not in FFC-1 (Table 15). The high-volume estimations of 23% diabase, given by the Dalby cores (Table 15) might be misleading. The cores have been produced by Sydsten AB in a diabase prospecting context, and does not display the actual average of the Romeleåsen area. If we extrapolate the FFC-1 conditions on the Dalby quarry and exclude diabase, we get at gneiss content of 86.4% and 13.6% of amphibole. If we then take into account that a fair amount of the amphibolite-gneiss samples of DGE-1 and FFC-1 constitutes of gneiss, the crystalline basement in the three localities display a concordance in distribution of gneiss and amphibolite.

Table 15. Relative distribution of the various rock types in the Dalby quarry, DGE-1 and FFC-1, given in volume percent.

Rock type	Dalby quarry <sup>a</sup> * (%)	DGE-1 <sup>b</sup> (%)	FFC-1 <sup>b</sup> (%)
Felsic gneissic	63.3	80	80.6
Diabase	23.1	3.8	-
Amphibolite	9.9		
Amphibolite-gneiss		16.2	19.4

\* Values have been normalized as 3.7% of the DGE-1 cores was unidentified due to weathering and fracturing.

<sup>a</sup> performed by Hanna (2021)

<sup>b</sup> Erlström and Rosberg (2021)

The metamorphism can be enhanced by the presence of hydrothermal fluids and this is indicated by the presence, both in FFC-1 and Dalby, by hydrated silicate minerals such as amphibole, biotite and the sulphides pyrite and galena.

Carbonate fracture fillings and the presence of hematite, magnetite and chalcopyrite are also a result of transport and precipitation of fluids, displayed in both localities. According to a study by Halling (2015)

on fracture minerals in Dalby, many of these minerals are indicators of low pressure/temperature conditions, i.e., minerals formed under zeolitfacies/sub-greenschist and amphibolite facies. Other fracture minerals seem to be dominating in certain rocks, such as epidote in felsic samples. To place the different generations of fracture fillings in time further investigations are required (Halling 2015).

There are minor discrepancies between the FFC-1 and the Dalby samples regarding the grade of metamorphism. Plagioclase is similarly distributed, but the amount of Na-rich plagioclase is significantly lower in the FFC-1 samples. It is known that the amount of Ca-rich plagioclase increases by intensified metamorphism during amphibolite facies (Klein and Philpotts 2012). High amounts of Ca-plagioclase in the FFC-1 could thereby indicate a higher degree of metamorphism in FFC-1 than in Dalby. This postulates that the higher Ca-content given by the FFC-1 amphibolites can be correlated to plagioclase in the chemical analysis (Table 13).

Garnet can form over a wide range of temperature and pressure but it typically forms during metamorphism at relatively high pressures and temperatures. Garnet is found in both felsic and mafic rocks in FFC-1 and Dalby. A significant observation is that the amphibolites in FFC-1 are relatively garnet-rich, in comparison to the Dalby amphibolite and metabasite which is rather poor in garnet. From the FFC-1 cuttings, (2654–2660m depth) (Fig. 26D) small grains of a green mineral, possibly green pyroxene, very rich in garnet also have been observed.

The mineralogy is of great importance as it relates to the thermal properties of the rock. Quartz is by all means the most significant conductor among the minerals and therefore, when present, the most important mineral for estimating the conductivity (Sundberg 1991). Typically felsic rock, gives hence, the best prerequisites regarding the thermal exchange between the rock and the circulation fluid and EGS reservoir. Mafic rocks, which are rich in iron, magnesium and calcium, and with a comparatively low SiO<sub>2</sub> content of 45-53%, are thus less favourable. Even though the FFC-1 crystalline rock has a mafic origin and the SiO<sub>2</sub>-content for orthogneiss and amphibolite therefore can be expected lower than if the origin was felsic, the SiO<sub>2</sub>-content is relatively high.

Based on the chemical analysis performed on FFC-1 samples the average SiO<sub>2</sub> content for the felsic rocks has been estimated to 70 wt.% and for the mafic to 62 wt.%. The results have been compared with data from chemical analysis presented by Sivhed et al. (1999) on samples from Dalby quarry (Table 16). It appears that the FFC-1 bedrock displays a 13 weight % higher SiO<sub>2</sub> content than the DGE-1 bedrock, this regarding both gneiss and amphibolite (Table 16).

On the samples used for the Dalby chemical analysis, conducted by Sivhed et al (1999), modal analysis was also performed. These values, differs with a few percent by volume when compared to the values from the modal analysis on the Dalby cores performed here. Based on the general agreement between the two modal analyses (Table 17) and the correlative results from DGE-1 chemical analysis, FFC-1 corresponds to a quartz content of approximately 37%

for the felsic rocks and 4% for amphibolite. The value is rather normal for granites, which lies between 20% and 60% quartz by volume. The FFC-1 volume is 3% higher than the estimated values in DGE-1, which is a clear benefit. Unfortunately, no SiO<sub>2</sub>-analysis have been conducted on the granitoid rocks at the St1 drilling in Espoo for comparison (A. Karjalainen, personal communication, august 30, 2021)

Table 16. Chemical analysis of average SiO<sub>2</sub>- content in FFC-1 and DGE-1.

	Rock type	SiO <sub>2</sub> (weight %)
FFC-1 <sup>a</sup>	Felsic gneissic	70
	Amphibolite	62
Dalby <sup>b</sup>	Felsic gneissic	57
	Amphibolite	49

<sup>a</sup> performed by ALS Chemicals (2021)

<sup>b</sup> Sivhed et al. (1999)

Table 17. Modal analyses of average quartz content in the Dalby samples given in % per volume.

	Rock type	Quartz (volume %)
Dalby	Felsic gneissic <sup>a</sup>	34
	Felsic gneissic <sup>b</sup>	30
	Amphibolite <sup>a</sup>	0
	Amphibolite <sup>b</sup>	3

<sup>a</sup> performed by Kervall (2021)

<sup>b</sup> Sivhed et al. (1999)

The high quartz content presented by the amphibolite is rather uncommon. Based on the absent/low amount of quartz in the thin sections (Table 17), and an assumed mafic origin of the amphibolite, it is reasonable to assume that the high SiO<sub>2</sub> given by the chemical analysis, is the result of secondary formed quartz i.e., silicification. Hydrothermal activity can promote quartz growth in vugs and fractures within the rock. These are features displayed both in Dalby (Figs 11C, 17H and 18B) and the FFC-1 samples (Figs. 24H, 27C and 27D). Single quartz grains were also frequently occurring in the cuttings when drilling amphibolite-rich intervals at the FFC-1, which support this theory.

### 5.1.2 Textures and bearing on strength

The texture of a rock is its physical appearance on a grain size level. Properties such as size, shape and orientation of the crystals, as well as how they are put together differs based on the rock's origin and history.

Textures can therefore be used in understanding the processes the rock has been exposed to, but also turn handy when determine the rock's physical properties. The texture of the rock also plays a significant role in the feasibility to shear and create an EGS reservoir.

The primary textures of igneous rocks reflect the conditions under crystallization while secondary textures mainly form during cooling processes. Secondary textures reflect chemical changes during the primary conditions and are not to be regarded as metamorphic. If the solid rock is exposed to a metamorphic event the rock develops new secondary textures (Winter 2014).

The term texture is often used and defined differently. In this work the term will refer to textures as penetrative small-scale features. In the EGS-context the most prominent of these are grain-size, interlocking crystals, homogeneity/heterogeneity, anisotropy/isotropy and foliation.

The rocks from FFC-1 and Dalby are all fine-grained, except one of the Dalby amphibolites, which is very-fine grained. The grain-size is of importance when it comes to the rock's bearing on strength, which increases with decreased grain-size. Rocks usually fracture along the grain boundaries as the bounds here are weaker. Small grains have a larger area over volume. If the area, (grain boundary) increases in relation to the volume, so will the force that holds the grains together and counteract fracturing. In an EGS-context; fractures in a rock with smaller grain-size would be easier to maintain, but harder to expand.

All samples also show an interlocking texture. When crystals are interlocked the rock is both harder and less porous than rocks with round grains. Low porosity usually equals higher density and higher thermal conductivity, but also lower heat capacity, which is typical for crystalline rocks (Sundberg et al. 2009). Homo- and heterogeneity is especially to be considered in assessing EGS thermal estimations and models. Estimations on heterogeneous rocks risk to be less accurate, if surveys are not comprehensive and conducted over large volumes. Gneiss is by nature considered heterogeneous, which is displayed both in FFC- and Dalby. The deviating homogeneity of 43%, displayed by the Dalby felsic samples is consistent with the Dalby core descriptions. The deviation is probably irrelevant as the small scale displayed in cores and thin sections not likely represent the whole rock in gneiss. However, this does not deny that Dalby might display a notable amount of single homogeneous blocks.

All Dalby metabasite and amphibolite samples show homogeneity, and thereby differ from the felsic samples. Due to lack of cores no separate results are presented for the FFC-1 mafic rocks. When comparing the FFC-1 samples with each other they show a variation, mainly pronounced by the quartz content, which is acknowledged both in cuttings, in the gamma ray log (2300–2325 m and 3025–3133 m depth) and indicated by the chemical analysis (Table 13). As discussed in the mineralogy section, the quartz is secondary formed, and the peaks in the gamma ray log might therefor represent quartz veins or interbedded gneiss layers rather than heterogeneity of the rock. It is therefore likely to assume that the amphibolite in FFC-1 is homogenous. Adding the amphibolite's relative high

density to this, it is likely that the rock is less naturally fractured than gneiss. This is something to have in mind if, under possible future surveys, the amount of amphibolite is increasing with depth.

Metamorphic rock usually displays anisotropy in varied degree and just like with heterogeneity, anisotropy can aggravate the EGS thermal estimations and modelling. The reason for this is that anisotropic rocks are often layered and, based on mineralogy, -can give anisotropic thermal properties. The heat conduction can therefore either be enhanced or impoverished in the direction of the layering. There is a general assumed relation between anisotropy and low thermal conductivity. The heat capacity, however, is not affected by anisotropy since the potential to store heat is not dependent on the orientation (Sundberg et al. 2009). Regarding anisotropy and its impact on rock strength, it is easy to assume that anisotropy weakens the rock. It is not impossible though that one could benefit from the conditions if the anisotropy is well understood. This is, for example, if a dominant orientation of the layering can be distinguished, or if the rock has fractured favourably due to the anisotropy. The results from Dalby and FFC-1 both indicate a highly anisotropic bedrock. Highly anisotropic conditions have also been displayed in the 2200 m deep borehole RHB70 of Forsmark, Sweden (Svensk kärnbränslehantering 2009-a). The Forsmark area's intrusive felsic rock is intersected by ductile amphibolite belts, just as FFC-1. The bedrock in Forsmark belongs, together with the bedrock of Finnish Espoo, to the Svecokarelian province (Stephens and Wahlgren 2020). Future study comparisons of anisotropic conditions with Forsmark and Espoo can therefore be relevant. For more detailed geological descriptions on Forsmark, see SKB -rapport R-10-04 (Svensk kärnbränslehantering 2009-b).

Foliation is the result of deformation and heat combined, often related to orogenesis (Winter 2014). The texture is observed in samples both from Dalby and FFC-1. The foliation is assessed as more or less horizontal in the CXD and SCMI logs from FFC-1 (Rosberg and Erlström 2021), which also resembles of the interior parts of ES (Wikman et al. 1993; Ulmius et al. 2018). Foliation is more or less characteristic in gneiss and indicates medium to high metamorphism. The foliation is generally less frequent in the mafic rocks and due to lack of cores, no results can therefore be presented from FFC-1 mafic samples. In the mafic Dalby samples, however, all samples display foliation.

The metabasite sample D2A (Fig. 16D) and one of the amphibolite samples; D7A (Fig. 16B) further present mylonite development, which is an indicator of very high strain. Mylonite form in shear-zones where they can be exposed to "softening"/ "strain-softening", which tend to fracture the rock more easily. The likelihood of softening is higher if old minerals are replaced by softer variants, such as muscovite (Mitra 1978; White et al. 1980; Hippertt and Hongn 1998), or if the minerals are placed in a lattice-preferred orientation which facilitates dislocation glide (Ji et al. 2004). The process is also related to development of shear bands (Ji et al. 2004). Gneisses tends to fracture along the foliation planes (Van Der Pluijm and Marshak 2004). This necessarily doesn't mean that the bearing strength

is less in a gneiss in comparison to granite. Even rocks with typical gneissic appearance, and with clear foliation can act as homogenous rock when exposed to high stress i.e., not fracturing along the foliation as expected (Best 2002).

The secondary non-metamorphic textures observed in Dalby and FFC-1 are all, except saussuritization and perthite/antiperthite, deuteric alterations i.e., water influenced (Winter 2014). The processes identified are; uraltization, which is alteration of pyroxene to amphibole. Indications of this is observed in Dalby (Fig. 17F), but more frequent in the FFC-1. Chloritization, which is alteration of mafic minerals to form chlorite is common the Dalby samples, especially associated to the amphibolite layers. The occurrence in Dalby have been confirmed by Halling (2015), and similar observations have been made in FFC-1. Biotitization is the alteration of hornblende or pyroxene to biotite, with epidote as a possible biproduct. Epidote occurs commonly as fracture fillings in the felsic rocks from both Dalby and FFC-1 (Figs. 14C-D and 23B-D). The occurrence of epidote in Dalby is further described by Halling (2015).

Saussuritization texture indicates alteration of Na-rich plagioclase to form epidote minerals. The texture, which is the initial stage of the alteration have been confirmed in the EDS-SEM analysis and is verified in 86% of the samples in Dalby and all of the FFC-1 samples. Perthite/antiperthite, textures that display changing potassium/sodium conditions during cooling (Winter 2014) is also frequently occurring, especially in the felsic Dalby samples.

All non-metamorphic textures mentioned above, implies an alteration where one mineral is consumed by the formation of a new mineral phase. The change in the physical rock properties is related to the grade of the alteration as well as the characteristics of the new mineral formed. In general, it is assessed that these features weaken the rock.

## 5.2 Fracturing

When a rock is exposed to metamorphism, the existing fracture system changes to a variable extent. An example of this is the fracturing of granite and gneiss. Granite is homogenous so when fracturing the fractures tends to be arranged in a relative uniform polygon-shaped framework (Tunemar 2006). When exposed to metamorphism the typical heterogenous gneiss texture develops, and fracturing tends to orient along the foliations (Van Der Pluijm and Marshak 2004). However, both the pre-metamorphic fracturing and the subsequent fracturing of the metamorphic rock can occur in a rock.

Within the oil industry, the fractures are simply divided into initial and secondary. Fractures that are induced by drilling (DIF:s) or hydraulic stimulation are referred to as secondary, while all others are regarded as initial. For a comprehensive understanding of the fracture system, subdivision of the initial fractures needs to be performed. This is because different tectonics creates different fractures (Sorkhabi 2014) and stress orientations varies over the geological time scale.

We know that fracture frequency generally decreases gradually with depth (MIT 2006). At shallower

depth the fractures generally extend up to ten meters and are at least partially open (MIT 2006). The fractures at greater depth are often closed due to pressure. However, micro fractures still constitute the dominating pore space in a crystalline rock (Sundberg et al. 2009).

Extensive very large and hydraulically active singular fractures are usually not desired as they can disturb the heat flow (Juhlin et al. 1998; Sundberg et al. 2009). These may cause less good thermal exchange in the reservoir as the flow would be concentrated to these and not spread over a larger rock volume via smaller undulating and connected fractures, which yield a more favourable thermal exchange. Greater fracture systems are also harder to handle and can result in less control and water leakage, similarly to what happened in the Soultz-project (Wallrot 1994; MIT 2006). Smaller fractures, on the other hand, are of most importance as an effective water heating is achieved by a large contact area between the bedrock wall and the water flowing through the EGS-system.

Large-scale fracture systems are best mapped using seismic surveys, which gives a possibility to map their dimension and orientation to 5–6 kilometres depth (MIT 2006). One way to do this is letting the seismic equipment register the rock mass from a borehole. Detailed fracture information in the borehole wall is also possible to describe from results obtained by geophysical wire-line logging. Sorkhabi (2014) lists ten characteristics that should be included in a comprehensive fracture survey, these are:

- type of fracture and filling
- association of fracture with particular lithology, structure etc.
- fractures set
- fracture length
- fracture frequency
- aperture (width)
- spacing of fractures
- strike and dip
- asperities (fracture walls roughness and irregularities)
- fracture stiffness

At FFC-1 the first seven of these were acquired. Unfortunately, no reliable data exist from the upper most highly fractured 400 meters i.e., down to c. 2400 m depth (Rosberg and Erlström 2021; Ciuperca et al. 2021). Nevertheless, reliable data have successfully been obtained below this depth.

Great water flows, dramatic changes in the drilling parameters and high frequency of fracture filling materials all coincided with, what was later confirmed in Weatherford's report, increased fracturing that occur between 2562 m and 2695 m depth (Badulescu and Ciuperca 2021). This zone is also con-

firmed by geothermal gradient variations presented by Rosberg and Erlström (2021), and a total of 329 fractures identified over the 133 m thick fractured zone. The fracture frequency corresponds to an average volumetric fracture density of 3.39 m<sup>2</sup>/m<sup>3</sup> and a linear fracture frequency of 2.49 fractures/meter (Rosberg and Erlström 2021). The average fractures/meter above the zone is calculated to 1.62 and 0.85 below the zone. The fracture frequency is however not evenly distributed within the zones, but display thinner intervals with higher values.

Swedish Nuclear Fuel and Waste Management Company (SKB) has in c. 1000 m deep boreholes, performed fracture investigations similar to the ones in FFC-1. Their results display an open fracture frequency generally below 3 fractures/m and fracture densities has been assessed between 1.4 and 4.6 m<sup>2</sup>/m<sup>3</sup>, which are in the same range as the values in FFC-1 (La pointe et al. 2008; SKB 2009-c). From 2000–5000 meters depth, in boreholes in Switzerland’s Basil, UK:s Rosmanowes and the French Soultz-project, display unanimous fracture frequencies below c. 1 fracture/meter (MEET 2020). In the paragneiss-amphibolite shear zone of the KBT borehole, <0.28 fractures/m have been reported between 6900 and 7135 m depth (Zimmerman et al. 2000). At the Espoo-project in Finland a highly fractured and hydraulically conductive zone was encountered in ONT 2B between 4800 and 5500 m and, according to A. Karjalainen, (personal communication, august 30, 2021) only rough estimations on the fracture frequency have been performed, indicated 17% fractured rock in the ONT 2B. The fracture frequency needs to be depth interval-based for useful comparisons, preferably in the fracture/meter.

Furthermore, the fracture mapping presented by Ciuperca et al. (2021), shows that within the 2562–2695 m zone individual fractures are up to 12 mm wide. The borehole imaging logs performed between 2154–3106 m, show a dominance of open fracture sets oriented N–S, and some also NW–SE (Rosberg and Erlström 2021). Surprisingly though, both directions differ from the main NE–SW strike of the main faults in Scania (Badulescu and Ciuperca 2021).

From visual examination of intact samples, it is observed that the felsic samples from Dalby display a higher fracture frequency than the mafic, especially regarding fractures smaller than <0,2 mm (Table 6). The felsic samples also deviate by displaying more fracture types than the mafic ones. Almost half of the felsic samples display all three fracture types. This isn’t seen in any of the mafic samples. Approximately 70% of the felsic and the mafic samples display two types of fractures though. If a rock contains several fracture types, their ability to crosscut is enhanced (Tunemar 2006) which further increases the fracture system’s volume and interconnection and thus, beneficial for EGS. In this regard the felsic rock is the most beneficial.

Contraction, shown by longitudinal splitting is, together with shearing, the most characteristic fracture types seen in the Dalby rocks. Shearing fractures are represented in 71% of the felsic rocks and in 66% of the mafic rocks. The shearing processes are represented by several features and are of special interest for

EGS. The shear fractures can’t grow in their own plane, instead the propagate parallel to  $\sigma_1$ . For wing-crack fractures, for example, typical minor fractures are created on their edges, and as they break, a fractured zone around the main fracture is created (Fig. 15G). Not only does this result in great fracture zones, the zones also have been observed to be broaden by depth (Winter 2014). These deep and voluminous fracture systems have great prerequisites to respond to EGS-stimulation. According to Halling (2015) most fractures seem to originate from extension fractures. Almost 60% of the rocks in this study display extension fractures, which further strengthen the interpretation of an efficient fracture interconnection. The observed fracture types and fillings further correspond well with the fracture generations presented by Halling (2015).

In Table 18 volume estimations on the distribution of fractured rock in Dalby is displayed by rock type. The estimations give that 36% of the amphibolite and 6% of the gneiss is highly fractured. The volume estimation indicates the true fracture frequency and is not to be confused with the visual examination above, which only applies to intact cores and are therefore only fracture type representative. However, from these two examinations we get that the gneiss, even though fractured, holds together in a higher extent than the amphibolite. This can be a result of a higher bearing strength of gneiss than of amphibolite. The opposite is however also possible, and that the bedrock’s sliding on the amphibolite layers have caused parts of it to heavily fracture (Sydsten AB 2002).

The results in Table 18 from Dalby are further interpreted to reflect the conditions for the same rocks in FFC-1.

Table 18. Relative distribution of rocks in Dalby quarry. Volume estimation based on description performed by Sydsten 2002, of 15 cores, totally 898m.

Rock type	%
<b>Felsic Gneissic</b>	<b>63.3</b>
weathered and fractured	0.9
weathered	2.8
<b>Diabase</b>	<b>23.1</b>
fractured	1.1
<b>Amphibolite</b>	<b>9.9</b>
fractured	3.6

### 5.2.1 Interpretation and estimated ability to respond to EGS-stimulation

EGS aims to artificially increase the permeability of the rock and this process is either performed by fracking or shearing. In Sweden and in Finland the aim, so far, has been to apply the shearing technique

on pre-fractured rock with medium to high permeability. The Swedish DGE-1 and FFC-1 boreholes are both situated in fractured rock; the Romeleåsen Fault Zone, and south western Scania respectively. The Espoo-project in Finland is located just east of Fennia, one of the Fennoscandic shield's larger fracture zones (Rämö et al. 2005).

The prerequisites for a successful stimulation are based on a comprehensive survey where geophysical logging and cores play the main role. From the cores the angle of inclination for fractures and weakness zones can be estimated, together with the character of the rock (Lundegårdh 1963). Unfortunately no cores were obtained from FFC-1. However, geophysical logging can provide essential complementary information, just as the survey in the FFC-1 borehole. Here data from image logs and micro seismic tools have provided useful data that to some extent replace the absence of core data.

The potential to stimulate a rock mass depends on the existence of interconnected fractures and the fractures petrophysical properties. Efficient hydraulic communication is achieved by a high number of long and intersecting fractures (Sorkhabi 2014). The estimated fracture population in FFC-1 give a rather high average volumetric density of  $3.39 \text{ m}^2/\text{m}^3$ . No estimated fracture length was connected to these results though. In the context, fractures  $>20 \text{ m}$  are preferable. Fractures  $< 1 \text{ m}$  is regarded as low persistence and  $> 20 \text{ m}$  indicates high persistence (Sorkhabi 2014).

The fractures petrophysical properties include permeability and porosity (Sorkhabi 2014). According to Zhang et al. (2021) the permeability can be increased by 1–2 orders of magnitude in an efficient fracture system. This is further controlled by the degree of fracture filling and aperture (Zhang et al. 2021). As mentioned before, the maximum aperture in FFC-1 was estimated 12 mm. Average aperture is  $> 10 \text{ mm}$  for open fractures and  $< 0.25 \text{ mm}$  for closed fractures. The permeability is also dependent on asperities i.e., ruggedness of the fracture surfaces (Sorkhabi 2014). According to Dusseault (2016) the asperities are the keys to permanency of a sheared fracture system. The most rugged surfaces are further displayed by the steep cleavages (or fractures) that intersects the bottom cleavages (Lundegårdh 1963).

According to the image logging of FFC-1 closed fractures dominate over open, regardless of size.

Lundegårdh (1963) stated that rock mainly fracture along three planes i.e., cleavages which are zones of weakness, often invisible to the naked eye. When cleavages are exposed to pressure changes, or changed stress orientation, they can open into fractures. The cleavages are perpendicular to each other, which correlate with an intergrowth structure between the minerals. One of these planes; bottom cleavages run horizontal, parallel to the basement surface. Due to pressure release after the last glaciation, series of regularly recurrent bottom cleavages, so called cheeting, most likely developed in the Scanian bedrock. The shearing features in Dalby indicates that a high amount of rock cleavages was opened. The high frequency of shearing features in Dalby, and the likelihood of cheeting are interpreted as good prerequisites for EGS.

The shearing method applied on the FFC-1 target rock with its characteristics are, of what we know so far, beneficial. The ability to map the stress orientations and to evaluate the fractures system further is however required to estimate the response to an EGS-stimulation. This is more important in non-homogeneous bedrock, as the effect of the stimulation here is harder to assess (Ayling et al. 2016). Cores, of a substantial length needs to be obtained and also more data from geophysical logging, where stress orientations and fracture characteristics, such as length and asperities are estimated.

Complex surveys where the bedrocks prerequisites are evaluated is crucial, but even though, it should not be forgotten that these are pioneer-projects where lessons are continuously learnt. At the moment, a 1.5-year long revalidation of the Espoo project is in progress in Finland. According to M. Pentti (personal communication, august 29, 2021) the upper part of the well was sealed off after the stimulation of ONT-3 at 5000–6000 meters depth, with a 900-bar hydrostatic pressure at the well-head, and 400–500 bar by the open fractures. Since then, the flow has only amounted to a few litres/sec of what initially was estimated to be 50 litres/sec. In the writing moment a well-to-well pressurized cross flow test is prepared for, aiming to improve the permeability, and monitored by 12 geophones situated at 300–1000 meters depth 2–4 km from the well. Utilization of additives during the stimulation is also considered.

### 5.3 Stresses

Knowledge of current stress field have proven extremely useful when engineering geothermal systems (Zang et al. 2012). In the case of both fracking and shearing, the stress direction must be considered, and therefore determines where the production and injection wells should be placed. Both size and orientation of the stress can be measured by geophysical logging (Wirtén 2020). It can also be measured in-situ, through hydraulic fracturing, or be obtained from cores representing the current depth (Alm 2012). The size of the stress is of relevance, not least for the stimulation process, as the rock's compressive stress needs to be exceeded by stress created by a hydrostatic pressure in the borehole surroundings (Dusseault 2016).

For a general understanding and estimation of the stress regime World Stress Maps (WSM) have become of the utmost importance (Zang et al. 2012). WSM is a global compilation presenting the present-day crustal stress of the Earth regionally (WSM 2020) in the upper 40 km of the Earth's crust (Heidbach et al. 2016). According to WSM (2020) the stress indicators can be divided into four categories whereas one constitutes of well bore breakouts (BB), which is stress induced variations in bore hole cross sections, including DIF:s. These are important indicators of horizontal stress orientation, particularly at intermediate depths ( $<5 \text{ km}$ ). BB:s and DIF:s has determined approximately 19% of the stress orientation indicators in the WSM database. They also provide most stress orientation indicators in both geothermal and petroleum systems (Tingay et al. 2008).

According to the world stress map the southern parts of Sweden display a SW –NE stress orientation.

There is also a stress regime stretching in a WNW–ESE direction of the Tornquist Zone. Northern Germany displays a N–S orientation (Zang et al. 2012) which is like the characteristic NW–NNW stress orientation seen in western Europe (Zoback 1992). The stress orientations of Denmark and the Kattegat area seems to be an area where several stress orientations meet (Zang et al. 2012). Along fault in the Tornquist Zone, and especially in the Kattegat area, stress most likely are still being released along the main fault, as indicated by minor deep-seated earthquakes (Gregersen et al. 1996).

Local stress regimes have been estimated both in Forsmark and Laxemar, indicating a dominating NW–SE orientation (Nordén et al. 2008). Similar results have been estimated in Espoo borehole (A. Karjalainen, personal communication, august 30, 2021). Forsmark displays a rather high rock stress; at 500 m maximum stress are estimated 40 MPa. This is explained by SKB as a cause of low fracture frequency in the rock (SKB 2009-b). From GPS seismic measurements 1989–1998 south of the TZ has indicated NW–SE oriented stress related to rift movements in the North Atlantic of 2 mm/year strike-slip movements (Pan et al. 2001). No stress orientations have so far been successfully obtained from either FFC-1 or DGE-1.

## 5.4 Thermal properties

### 5.4.1 Geothermal gradient

Thermal properties such as temperature and temperature gradient determine the effective production of an EGS-plant and thereby forms the basis for assessing drilling depth (Jeanloz and Stone 2013). In Sweden the geothermal gradient varies from 15–20 °C/km in the north, to  $\leq 30$  °C/km in the southernmost parts (Erlström et al. 2016). The gradient in the sedimentary bedrock in SW Scania is between 27 and 33 °C/km while the corresponding gradient for the crystalline bedrock in DGE-1 and FFC-1 is c. 20 °C/km. Considering a target temperature of c. 140 °C this would mean a total depth of c. 6 km for EGS drilling.

In FFC-1 the bottom hole temperature (3113 m depth) was measured to 84.1 °C, with a geothermal gradient varying between 17.4 and 23.5 °C/km (Rosberg and Erlström 2021). Above 2610 meters the average gradient is 23.5 °C/km, and below 2880 m, the average has dropped to 17.4 °C/km (Rosberg and Erlström 2021). There is a geological difference between these two sections and the area between them displays a thermal disturbance, given by a drop in temperature, from 23.5°C to 7 °C/km (Rosberg and Erlström 2021). These types of local deviations can occur in adherence to larger water bearing fracture zones, such as in FFC-1. Similar gradients to both the FFC-1 highest and lowest are however found separately in deep boreholes in the Fennoscandian Shield and the two gradients have therefore been addressed in two different tables. In Table 19 sites with higher gradients are being compared and in Table 20, sites with lower gradients. Note though that the crystalline bedrock in both FFC-1 and DGE-1 present geothermal gradients around 20 °C/km. The DGE-1 borehole is situated in the Romeleåsen Fault Zone, approximately 15 kilometres WNW of FFC-1 (Fig. 2) and therefore holds

the most adequate data for comparison (Table 19). Thermal modelling of the Fennoscandian Shield shows that the Tornquist Zone excel by displaying gradients higher than the surroundings, between 20 and 24 °C/km in the upper crust, which also correlates with the gradient of 22 °C in DGE-1 (Balling 1995).

DGE-1 is 567 m deeper than FFC-1 and still the bottom temperature is only one degree higher than in FFC-1. When extrapolating the data in FFC-1 at corresponding depth, using the lower section's thermal gradient of 17 °C/km we get a bottom hole temperature of 94.3 °C (Rosberg and Erlström 2021). The 9 °C lower gradient displayed in the DGE-1 is explained by a deviant low average gradient of 14 °C/km in the overlying sedimentary succession (Table 19). The temperature deviation is most likely related to the DGE-1's localisation where the complex block-faulting might affect the bedrocks thermal conductivity negatively. Surrounding sedimentary bedrock display similar gradients as FFC-1, between 28 and 32 °C/km (Erlström et al. 2018).

Increased amounts of potassium, thorium and uranium in the bedrock favour the heat production. This is primarily the case for younger granites and pegmatites, where the heat production can be significantly higher than average crystalline rock of the Fennoscandian Shield (MIT 2006; Erlström et al. 2016). In Sweden elevated levels of the elements have been observed in the Bohus granite (Landström et al. 1980) and on Alnön, outside Sundsvall, the so called Rödö granite (Persson et al. 2014). The occurrence of the three radioactive elements in the bedrock in FFC-1 are rather low, as displayed in the Spectral Gamma Ray log. In the log we see that the heat production is, exempt for a few peaks, steady below 4  $\mu\text{W}/\text{m}^3$ . The heat production displayed in the DGE-1, on the other hand, is overall higher than 5.0  $\mu\text{W}/\text{m}^3$ . The average heat production is 5.8  $\mu\text{W}/\text{m}^3$  in DGE-1 and approximately 3.0  $\mu\text{W}/\text{m}^3$  in FFC-1, with exception for the amphibolite dominated intervals with an average of 1.5  $\mu\text{W}/\text{m}^3$  (Rosberg and Erlström 2021). Even though the occurrences of the radioactive elements are generally low in FFC-1, one can tell from the log that the elements are related to the granitic composition, as the signals disappears below 3030 m, where amphibolite dominates (Fig. 10). In Rosberg and Erlström (2021) the difference between DGE-1 and FFC-1 is explained by the different bedrock types. On the radiometric map of Sweden (SGU) there is a pronounced difference between the interior of the ES, with lower radiometric values, and the higher values at the eastern boundary and transition segments where DGE-1 is located (Rosberg and Erlström 2021). The high geothermal gradient in FFC-1 can by other words not be explained by elevated levels of radioactive elements.

Similar heat production value, as calculated by Rosberg and Erlström (2021) for the FFC-1 (3.0  $\mu\text{W}/\text{m}^3$ ) are though displayed at other places within the Fennoscandian Shield, such as Gravberg-1, Laxemar, and Outokumpu R-2500 (Juhlin et al. 1991; Sundberg et al. 2009; Kukkonen et al. 2011).

As can be seen in Table 19 and Table 20 the FFC-1 and DGE-1 are the only two deep boreholes in the Fennoscandian Shield that include a thick sedimentary rock succession on top of the crystalline

Table 19. Comparison of thermal data and bedrock type from the FFC-1 well with other deep boreholes displaying temperature gradient similar to the higher gradient measured in FFC-1. The data in the table is in parts the same information presented in Rosberg and Erlström (2021).

	FFC-1 <sup>a</sup> , Malmö	DGE-1 <sup>b</sup> , Lund	COSC-1 <sup>c</sup> , Åre	Hunt well <sup>d</sup> , CA	KTB <sup>e</sup> , DE
Total depth (m)	3133	3702	2496	2363	9101
Sedimentary bedrock (m)	2112	1946	*	500	-
Crystalline bedrock (m)	498	1754	<2496	1863	9101
Temperature, bottom hole (°C)	84.1	85.1	-	47	265
Geothermal gradient, crystalline rock (°C/km)	17.4 / 23.5	22	20	20	21 & 28
Geothermal gradient, sedimentary succession (°C/km)	29,5	14	-		
Bedrock	Fennoscandian shield	Fennoscandian shield	Fennoscandian shield	Canadian shield	central European crust
Geological unit	Svecokarelian province	Svecokarelian province	Caledonian bedrock	Precambrian basement	-
Crystalline rock types	orthogneiss, amphibolite	orthogneiss, granite, metabasite	gneiss, mylonite meta-sandstone, amphibolite	orthogneiss, granite, mylonite	paragneiss, amphibolite

<sup>a</sup> Rosberg and Erlström (2021)

<sup>b</sup> Rosberg and Erlström (2019)

<sup>c</sup> Wiersberg (2020)

<sup>d</sup> Majorowicz et al. (2014)

<sup>e</sup> Emmermann and Lauterjung (1997)

Table 20. Comparison of thermal data and bedrock type from the FFC-1 well with other deep boreholes displaying temperature gradient similar to the lower gradient measured in FFC-1.

	FFC-1 <sup>a</sup> , Malmö	Gravberg <sup>b</sup> , Siljan Ring	KLX02 <sup>c</sup> , Laxemar	Bh 32012 <sup>c</sup> , Lake Vättern	ONT 1-3 <sup>d</sup> , Espoo, FI	Outokumpu <sup>e</sup> R-2500, FI
Total depth (m)	3133	6957	1700	1820	2000 (ONT-1) <sup>f</sup> 6400 (ONT-2,3)	2516
Sedimentary bedrock (m)	2112	-	-	-	-	1835*
Crystalline bedrock (m)	498	6957	1700	1820	6400	681*
Temperature, bottom hole (°C)	84.1	116	-	37	38 (ONT-1) <sup>f</sup> , 120 (ONT-2,3)	38
Geothermal gradient, crystalline rock (°C/km)	17.4 / 23.5	14-18	14-17 (<1400m)	15 & 20	17	14-17
Geothermal gradient, sedimentary succession (°C/km)	29,5	-	-	-	-	-
Bedrock	Fennoscandic shield	Fennoscandic shield	Fennoscandic shield	Fennoscandic shield	Fennoscandic shield	Fennoscandic shield
Geological unit	Svecokarelian province	Transscandinavian magmatic belt (TBM)	Transscandinavian magmatic belt (TBM)	Transscandinavian magmatic belt (TBM)	Svecokarelian province	Svecokarelian province
Crystalline rock types	orthogneiss, amphibolite	granite <sup>g</sup> , dolerite	Monzodiorit <sup>h</sup> - granodiorit	diorite	granitoid, mafiska & intermediate metavolcanic	ophiolite rock, pegmatitic granite

<sup>a</sup> Rosberg and Erlström (2021)

<sup>b</sup> Aldahan et al. (1991)

<sup>c</sup> Sundberg (2009)

<sup>d</sup> Kukkonen and Pentti (2021)

<sup>e</sup> Kukkonen et al. (2011)

<sup>f</sup> Saarno, T., personal communication (2020)

<sup>g</sup> Juhlin (1990)

<sup>h</sup> SGU kartvisare (2021)

basement. These conditions favour higher temperatures at comparable depth with wells without sedimentary cover strata. This is due to the relatively lower thermal conductivity of the sedimentary strata, thus having an isolating effect (MIT 2016). The Hunt Well borehole is an example of this in the Canadian Shield, where orthogneiss is covered by Phanerozoic sedimentary rocks (Table 19).

In relatively cold and thick crust, such as the Fennoscandian Shield, anomalies in the crust become of great importance for EGS. High temperature gradient of  $\leq 28$  °C have been measured in the 9101 m deep borehole of KTB in Germany, located in a suture zone (Table 19). The ST1/Fortum EGS-project in Finnish Espoo, located in a fracture zone, has reached a depth of 6400 m and display a geothermal gradient of 17 °C (Table 20). Higher gradients are also likely to be encountered at impact structures. The area in the Swedish Caledonides, by the Lake Siljan where the 2496 m deep COSC borehole is located, is in fact an old crater affiliated to sedimentary bedrock (Wiersberg et al. 2020). The COSC display a geothermal gradient of 20 °C (Table 19). The FFC-1 on the other hand is located near fault structures where lateral resistivity layers more or less efficient covers rock fractured by faulting and isostatically related pressure release.

#### 5.4.2 Thermal conductivity and density

The temperature is dependent on how efficient the heat is transported through the rock i.e., the thermal conductivity  $\lambda$ , W/mK. A high thermal conductivity can simple be explained as high heat loss or good heat transport, whereas low conductivity amount to the opposite. The conductivity depends on heat capacity (capacity to store heat)  $C^1$ , kWh/ (m<sup>3</sup> °C) and heat diffusivity (equalization of temperature differences)  $\kappa$ , m<sup>2</sup>/s. According to Sundberg (1991) crystalline rock heat capacity is usually estimated to approximately 0.55 kWh/ (m °C). Heat diffusivity ranges between approximately 0.6 mm<sup>2</sup>/s for basic rocks and 1.9 mm<sup>2</sup>/s for quartz-bearing acidic rocks (Drury 1987) even though values up to 5.4 mm<sup>2</sup>/s have been noted in the pegmatitic granite of Outokumpu (Kukkonen et al. 2011). The relation between the three thermal parameters is given by:  $\kappa = \lambda/C^1$  (Sundberg 1991).

The conductivity is specific and affected by density, structure, texture, porosity, water content and mineralogy of the rock (Erlström et al. 2016). For the most minerals, the thermal conductivity increases by increased pressure, and decrease by increased temperature (Labus and Labus 2018). As mentioned before quartz is the most efficient conductor and quartzite, pure quartz, has a conductivity of 7.7 W/mK (Sundberg 1991).

Other minerals that excel as conductors are olivine (4.1 W/mK) and pyroxene (3.8 W/mK (Sundberg 1991)). Neither the Dalby or FFC-1 samples contain olivine, and pyroxene only rarely occurs as remnants of grains except for the diorite-sample D4A which constitutes of 40% pyroxene. Unfortunately, no conductivity analysis was performed on this sample.

The thermal conductivity ranges generally between 3 and 4.5 W/mK for granite and for gneiss between 1.5–5 W/mK (Erlström et al. 2016). Gneiss and metamorphic rocks tend to present a lower conductivi-

ty due to anisotropy and foliation (Sundberg 1991). This can be seen in the FFC-1 sample M3T which presents a conductivity 0.7–0.8 W/mK lower than the less foliated gneiss samples (Table 12). Metamorphic rocks can also present a lower conductivity due to mineralogical changes or because they have a basic origin. The lower conductivity is displayed in both the Dalby and FFC-1 samples, where the conductivity generally is 1 W/mK higher in the quartz-rich felsic than the basic samples (Table 8 and 12). The estimated bedrock composition of over 63% felsic rocks in FFC-1 (below 2970 m) thereby indicate rather favourable conductivity conditions in the EGS-context (Table 18), and so does the estimated SiO<sub>2</sub> content of 70% (Table 16). Furthermore, it is worth mentioning that the conductivity of quartz is strongly temperature dependent, and it's most efficient as conductor at  $T < 200$  °C (Robertson 1988). Against the FFC-1 background, EGS is today mainly relevant for plants with a production temperature of around 160 degrees. In this context the conductivity of quartz would then be utilized optimally. The higher quartz content in FFC-1 correlates well with an overall higher conductivity regarding felsic samples (Table 12).

A comparison of the thermal conductivity between different sites and rocks are being compared in Table 21. The Scanian gneiss, presented in FFC-1 and DGE-1 distinguish by presenting the highest conductivity among the compared felsic rocks. Hunts Well and Outokumpu both present values for granite. The 0.5 W/mK lower value in Hunt Well of 2.5 is interpreted as underestimated due to paleoclimatic effects (Majorowicz et al. 2014). The lowest conductivity values, for all rock types, are presented by the KTB bore hole (Table 21). The values have been proven related to foliation and microfractures. Highest thermal values in the KTB-hole has further been localized parallel to the foliation (Emmermann and Lauterjung 1997). The mafic rocks of FFC-1 (amphibolite) and Outokumpu (metasediment) present similar conductivity values around 2.5 W/mK. The highest conductivity of the mafic samples is 3.35 W/mK, presented by the ophiolite-derived altered ultra-mafic rock from Outokumpu.

When comparing the density data (Tables 7 and 11) with the conductivity data (Tables 8 and 12) from FFC-1 and Dalby, we can clearly see that there is a mineralogical relation between the two parameters. The felsic samples overall display a higher conductivity and a lower density, as opposed to the amphibolite, which are characterized by lower conductivity and higher density. This is also well displayed in the composite log (Fig. 10) by the spectral gamma ray, which indirect gives the quartz-frequency, and the density log which typically counteract the conductivity when prominent compositional fluctuations occur.

The average density values of the Dalby outcrops show good agreement with values from earlier performed analysis on Romeleåsen horst, conducted by the Geological Survey of Sweden. These samples present an average gneiss/granite density of 2.64 g/cm<sup>3</sup> and 3.01 g/cm<sup>3</sup> for metabasite/amphibolite.

The average density values from the two sites are consistent both regarding the granitoid and amphibolite samples (Table 7). The density analyse of

diabase gives a value of 3.00 g/cm<sup>3</sup>, which is like the average for amphibolite (Table 7). It is likely though, that the thermal conductivity of diabase is slightly better than for amphibolite, as pyroxene is a more efficient thermal conductor than mica and amphibole which are relatively more common in amphibolite (Jones 2003).

The measured densities are similar to the ones noted for amphibolite (2.89 g/cm<sup>3</sup>) and paragneiss (2.74 g/cm<sup>3</sup>) in the German KTB borehole (Emmermann and Lauterjung 1997). Similar densities are also presented for granite (2.65 g/cm<sup>3</sup>), and for fractured granite (2.63 g/cm<sup>3</sup>) in the Gravberg-1 borehole (Juhlin 1990). The diabase occurring in the Gravberg-1 borehole have density of 3.00 g/cm<sup>3</sup>, which is the same as the DGE-1 diabase (Table 7) (Juhlin 1990).

Table 21. Average measured thermal conductivity (W/m K), specified for each rock type in various boreholes.

Bore hole	Rock type	Conductivity W/mK
FFC-1	Gneiss	3.62
	Amphibolite	2.57
Romeleåsen Horst	Gneiss	3.47
	Amphibolite	2.27
	Diabase	-
Outokumpo <sup>a</sup>	Metasediment	2.50
	Ohpialite-derived altered ultra mafic	3.35
	Pegmatitic granite	3.00
Laxemar <sup>b</sup>	Monzodiorite, Garanodiorite	2.75
Hunt Well <sup>c</sup>	Granite	2.5
KTB <sup>d</sup>	Paragneiss	1.5
	Hornblende Gneiss	1.15
	Amphibolite/Metabasite	0.53

<sup>a</sup> Kukkonen et al. (2011)

<sup>b</sup> Sundberg (2009)

<sup>c</sup> Majorowicz et al. (2014)

<sup>d</sup> Emmermann and Lauterjung (1997)

## 5.5 Assessment of a one cubic kilometre rock block at 6 km depth in SW Scania

The feasibility to construct a deep geothermal plant in SW Scania has until recent investigations been attached with several uncertainties regarding the geological prerequisites. Based on the geological studies of the data from the FFC-1, DGE-1 and the Dalby quarry the knowledge on several of the important properties have been clarified. The following prediction is based on the geological conditions in an arbitrary located one-cubic-km large rock block at EGS-depth in SW Scania.

Based on the rock composition the block will most likely be composed of two fine-grained rock types; felsic gneiss and mafic amphibolite/metabasite in the proportion of 4:1 (Table 15). Both rock types are fine-grained, anisotropic and composed of interlocking crystals. The gneiss is composed of predominantly quartz (c. 37% by volume), plagioclase and K-feldspars. The gneiss is reddish and display a heterogenous texture. The black amphibolite is homogeneously composed of plagioclase, amphibole and biotite and

rather rich in small red garnets. The quartz-content is c. 3-4% by volume in the amphibolite. The gneiss will have a thermal conductivity of around 3.6 W/mK and the amphibolite of c. 2.6 W/mK. The average density of gneiss will be 2.64 g/cm<sup>3</sup>, and of amphibolite 3.01 g/cm<sup>3</sup>. The geothermal gradient is most likely <20.5 °C/km. This indicates temperatures <140 °C at depths of six kilometres depth in southwestern Scania. This is mainly because the top of the crystalline basement that starts at 2000 m, beneath the sedimentary bedrock, has a temperature of c. 60 °C.

Even at 6000 m depth the rock block is likely to contain a substantial fracture system, mainly constituting of shear fractures connected to the horizontal fracture planes. Most of the fractures are old and closed. At least four fracture generations are present, represented by at least 15 mineral groups of which carbonate, quartz, epidote and fluorite are the dominating. Open fractures are however also likely to be encountered due to the ongoing tectonic activity (Gregersen et al. 1996). The open fracture frequency is predicted to c. 1-3 fractures/meter and the block is also likely to contain larger conductive crush zones. The block is predicted to have a high potential of latent fracturing due to cleavages. The cleavages, together with fractures sealed by minerals of less hardness most likely correspond well to hydraulic stimulation.

For drilling in crystalline rock to be economically defensible drilling rates between 10-15 meter/hour needs to be achieved. Rotary drilling is by all means the most reliable method applied here. The technique however, has an average ROP of 1.5 m/hr in this rock type, which is not cost-efficient today. The hammer drilling technique, which was evaluated in the heterogenous gneiss-amphibolite rock of both FFC-1 and Espoo has shown great difficulties in handling fracture zones with high water inflows. It also cannot meet the drilling rate requirement hoped for. The cost of wear on drill bits and pipes is a further disadvantage if the rock has a high density or hardness (Erlström 2016). Deep drilling in our rock block is dependent on more efficient drilling. Development of the hammer drilling technique, as to handle high water inflows and enable efficient removing of cuttings while drilling, would be the best way of succeeding with these types of drillings. Possibly can today's hammer drilling technique be applied at less fractured sections where water inflows are less likely.

## 6 Conclusions

- The Precambrian crystalline basement in the FFC-1 well in Malmö has more or less the same composition as the rocks on the Romeleåsen horst. Diabase, was however, not encountered in the FFC-1 well
- The two localities present the same type and density of fractures and fracture filling minerals
- The uppermost part of the bedrock is heavily fractured, giving good indications of micro fractures existing at greater depths beneath Malmö.

- The temperature gradient is relatively high in comparison to central parts of the Fennoscandian Shield
- The thermal conductivity is relatively high for the gneiss due high quartz content
- Based on results given in this thesis the EGS-prerequisites in the Fennoscandian Shield Border Zone in SW Scania are favourable
- Future investigations need to be implemented for describing the deep fracture frequency. This is provided through seismic surveys i.e., rock strain data, and deep cores.

## 7 Acknowledgements

Much appreciation is given to my supervisors Mikael Erlström (Swedish Geological Survey and Department of Geology, LU) and Ulf Söderlund for guidance, encourage and support. Frans Lundberg for interest and assistance during preparatory work and SEM-EDX-analysis; Leif Johansson for feed-back during optical microscopy and help with interpretations of the SEM-EDX-analysis, as well as for providing useful inputs on the Dalby quarry bedrock; Paula Lindgren for meaningful discussions during the optical microscopy; Charlotte Möller for inputs during SEM-analysis; Sydsten AB for providing cores and enable visit to Dalby quarry, and a special recognition to Leo Kramér for providing useful information. I have also very much appreciated the contact with the helpful crew in Espoo, Finland, and especially the communication with Matti Pentti at St1 Oy. Further I would like to acknowledge Anders Lindskog for help with sample scanning, Carl Alwmark for availability during SEM-EDX and Britta Smångs for reference-guidance. I would like to thank my co-students Per Wahlquist and Märta Westberg for sharing knowledge during SEM-EDX. Finally, I would like to thank my family and my friends for their support during this project.

## 8 References

- Aldahan A. A., Castaño J., Collini B., Gorody T., Juhlin, C. & Sandstedt H., 1991: Scientific summary report of the deep gas drilling project in the Siljan ring impact structure. *Vattenfall Technical Report SV-UG-91-14*, 286 pp.
- Alm, P.-G., 1999: Long-time study of geothermal data from a low enthalpy geothermal heat plant, Twenty-Fourth Workshop on Geothermal Reservoir Engineering Stanford University, Stanford, California, January 25-27, 1999. *Report SGP-TR-162*, 6 pp.
- Alm, P. G., 2012: "Logging" Geofysisk borrhålmätning. Lund, Lunds tekniska högskola, Lunds Universitet 85 pp. [in Swedish].
- Andréasson, P.-G. & Rodhe, A., 1990: Geology of the Protogine Zone south of Lake Vättern, southern Sweden: A reinterpretation. *Geologiska Föreningens i Stockholm Förhandlingar* 112, 107–125. doi: 10.1080/11035899009453168
- Aldenius, E., 2017: *Lunds Geotermisystem, en utvärdering av 30 års drift*. Bachelor's thesis no 515, Lund University, Lund, Sweden, 24 pp. [in Swedish].
- Austin, W. H., 1977: Geothermal power emerging as an alternative energy source. *Canadian Mining Journal*, 98 pp.
- Ayling, B. F., Hogarth, R. A. & Rose, P. E., 2016: Tracer testing at the Habanero EGS site, central Australia. *Geothermics* 63, 15-26. doi: 10.1016/j.geothermics.2015.03.008
- Badulescu, C. & Ciuperca, C., 2021: FFC-1 data interpretation report IAES Weatherford, *Internal project report 12132020*, 61 pp.
- Baker Hughes, 2012: Hydraulic Fracturing: An Environmentally Responsible Technology for Ensuring Our Energy Future. *Report*, 10 pp.
- Balling, N., 1995: Heat flow and thermal structure of the lithosphere across the Baltic Shield and northern Tornquist Zone. *Tectonophysics* 244, 13-50. doi: 10.1016/0040-1951(94)00215-U
- Bergelin, I., Obst, K., Söderlund, U., Larsson, K., Johansson, L., 2011: Mesozoic rift magmatism in the North Sea region: 40 Ar/39 Ar geochronology of Scanian basalts and geochemical constraints. *International Journal of Earth Sciences* 100 (4) 787-804.
- Bergerat, F., Angelier, J. & Andréasson, P.-G., 2007: Evolution of paleostress fields and brittle deformation of the Tornquist Zone in Scania (Sweden) during Permo-Mesozoic and Cenozoic times. *Tectonophysics* 444, 93-110. doi: 10.1016/j.tecto.2007.08.005
- Best, M. G., 2002: *Igneous and Metamorphic Petrology* Wiley-Blackwell, 752 pp.
- Bingen, B., Nordgulen, Ø. & Viola, G., 2008: A four-phase model for the Sveconorwegian orogeny, SW Scandinavia. *Norwegian Journal of Geology / Norsk Geologisk Forening* 88, 43–72.
- Bingen, B., Andersson, J., Söderlund, U. & Möller, C., 2008: The Mesoproterozoic in the Nordic countries. *Episodes* 31, 29–34.
- Brander, L. & Söderlund, U., 2009: Mesoproterozoic (1.47-1.44 Ga) orogenic magmatism in Fennoscandia; Baddeleyite U-Pb dating of a suite of massif-type anorthosite in S. Sweden. *International Journal of Earth Sciences* 98, 499-516. doi: 10.1007/s00531-007-0281-0
- Breede, K., Dzebisashvili, K., Liu, X. & Falcone, G., 2013: A systematic review of enhanced (or engineered) geothermal systems; past, present and future. *Geothermal Energy (Heidelberg)* 1.
- Cederberg, J., 2011: *U-Pb baddelyit datering av basiska gångar längs Romeleåsen i Skåne och deras påverkan av plastisk deformation i Protoginjonen*. Bachelor's thesis no 289, Lund University, Lund, Sweden. 17 pp. [in Swedish].
- Ciuperca, C-L., Camil, B., Erlström, M., Hammar, A., Egard, M., 2021: An integrated formation evaluation approach evaluated the basement tem-

- perature anomaly. EAGE 82nd conference and exhibition, Amsterdam, extended abstract: 4 pp.
- Destress, 2020: *Rittershoffen, France*. Retrieved 2021-06-21, from <http://www.destress-h2020.eu/en/demonstration-sites/rittershoffen-france/>
- Drury, M. J., 1987: Thermal diffusivity of some crystalline rocks. *Geothermics* 16, 105-115. doi: [https://doi.org/10.1016/0375-6505\(87\)90059-9](https://doi.org/10.1016/0375-6505(87)90059-9)
- Dusseault, M. B., 2016: Fracking vs hydroshearing. Retrieved 2021-04-13, from <https://www.cangea.ca/fracking-vs-hydroshearing.html>
- Eden Geothermal, 2021: *News*. Retrieved 2021-06-21, from <https://www.edengeothermal.com/news/>
- Egerton, R. F. & Springerlink, 2016: *Physical Principles of Electron Microscopy. An Introduction to TEM, SEM, and AEM*. Springer International Publishing, 211 pp.
- EGS Energy, 2021: *The Eden Deep Geothermal Plant*. Retrieved 2021-06-21, from <https://www.egs-energy.com/eden-deep-geothermal-plant/>
- Emmermann, R. & Lauterjung, J., 1997: The German Continental Deep Drilling Program KTB; overview and major results. *Journal of Geophysical Research* 102, 179. doi: 10.1029/96JB03945
- Energimyndigheten, 2018: Vägen till ett 100 procent förnybart elsystem. Delrapport 1: Framtidens elsystem och Sveriges förutsättningar, Energimyndigheten.se, 56 pp. [in Swedish].
- Erlström, M., 2009: Tectonic evolution and geological framework of Scania - A review of interpretations and geological models. Sveriges geologiska undersökning. *Report 2009:10*, Lund, 36 pp.
- Erlström, M., 2016: Anticipated and verified bedrock composition to 5 km depth at the FFC-1 site in Malmö -description of the c. 2100 m thick sedimentary bedrock succession in the FFC-1 well in Malmö. *Sveriges geologiska undersökning unpublished report*, 5 pp.
- Erlström, M., 2020: Carboniferous-Neogene tectonic evolution of the Fennoscandian transition zone, southern Sweden. In M-B. Stephens & J. Bergman Weihed (eds.): *Sweden Lithotectonic Framework, Tectonic Evolution and Mineral Resources*, 603-620. Geological Society of London, London, Memoirs 50.
- Erlström, M., Thomas, S. A., Deeks, N. & Sivhed, U., 1997: Structure and tectonic evolution of the Tornquist Zone and adjacent sedimentary basins in Scania and the southern Baltic Sea area. *Tectonophysics* 271, 191-215. Elsevier Scientific Pub. Co., Amsterdam.
- Erlström, M., Sivhed, U., Wikman, H. & Kornfält, K-A., 2004: *Beskrivning till berggrundskartorna 2D Tomelilla NV, NO, SV, SO 2E Simrishamn NV, SV 1D Ystad NV, NO 1E Örnahusen NV*. Sveriges geologiska undersökning, Ser Af 212-214. 141 pp. [in Swedish].
- Erlström, M., Mellqvist, C., Schwarz, G., Gustafsson, M. & Dahlqvist, P., 2016: Geologisk information för geoenergianläggningar – en översikt. Sveriges geologiska undersökning. Rapport 2016:16, 56 pp. [in Swedish].
- Erlström, M., Boldreel, L. O., Lindström, S., Andersen, M. S., Kristensen, L., Mathiesen, A., Kamla, E. & Nielsen, L. H., 2018: Stratigraphy and geothermal assessment of mesozoic sandstone reservoirs in the Øresund basin – Exemplified by well data and seismic profiles. *Bulletin of the Geological Society of Denmark* 66, 123-150.
- Fossen, H., 2010: *Structural Geology*. Cambridge University Press, Cambridge, 463 pp. doi: [org/10.1017/CBO9780511777806](https://doi.org/10.1017/CBO9780511777806)
- Gregersen, S., Leth, J., Lind, G. & Lykke-Andersen, H., 1996: Earthquake activity and its relationship with geologically recent motion in Denmark. *Tectonophysics* 257, 265–273.
- Halling, J., 2015: *Inventering av sprickmineraliseringar i en del av Sorgenfrei-Tornquistzonen, Dalby stensbrott, Skåne*. Bachelor's thesis no 448, Lund University, Lund, Sweden. 24 pp [in Swedish].
- Heidbach, O., Rajabi, M., Reiter, K., Ziegler, M. & VSM Team, 2016: *World Stress Map Database Release 2016*. Retrieved 2020-05-01 V. 1.1, from <http://dataservices.gfz-potsdam.de/wsm/showshort.php?id=escidoc:1680890>.
- Hippertt, J. F. & Hongn, F. D., 1998: Deformation mechanisms in the mylonite/ultramylonite transition. *Journal of Structural Geology* 20, 1435–1448.
- Hubbard, F. H., 1975: The Precambrian crystalline complex of south-western Sweden. The geology and petrogenetic development of the Varberg Region. *Geologiska Föreningen i Stockholm Förhandlingar* 97:3, 223–236. doi: 10.1080/11035897509454305
- Japsen, P., 1993: Influence of Lithology and Neogene Uplift on Seismic Velocities in Denmark: Implications for Depth Conversion of Maps1. *AAPG Bulletin* 77, 194-211. doi: 10.1306/bdff8bc8-1718-11d7-8645000102c1865d
- Jeanloz, R. & Stone, H., 2013: Enhanced Geothermal Systems. Office of Scientific and Technical Information (OSTI) *Report JSR-13-320*, Virginia, 147 pp.
- Jensen, K. D., Beier, C., Michelsen, A. & Emmett, B. A., 2003: Effects of experimental drought on microbial processes in two temperate heathlands at contrasting water conditions. *Applied Soil Ecology*, 165-176.
- Ji, S., Jiang, Z., Rybacki, E., Wirth, R., Prior, D. & Xia, B., 2004: Strain softening and microstructural evolution of anorthite aggregates and quartz-anorthite layered composites deformed in torsion. *Earth and Planetary Science Letters* 222, 377-390.
- Jones, M., 2003: Thermal properties of stratified rocks from Witwatersrand gold mining areas. *Journal of The South African Institute of Mining and Metallurgy* 103, 173-185.
- Juhlin, C., 1990: Interpretation of the reflections in the Siljan Ring area based on results from the Gravberg-1 borehole. *Tectonophysics* 173, 345-360
- Juhlin, C., Wallroth, T., Smellie, J., Eliasson, T., Ljunggren, C., Leijon, B. & Beswick, J., 1998: The very deep hole concept: geoscientific appraisal of conditions at great depth. *Svensk*

- kärnbränslehantering AB, *Technical Report 98:05*, 128 pp.
- Jung, R. 2013: EGS-Goodbye or Back to the Future 95. In A. P. Bungler, J. McLennan, & R. Jeffrey, (eds.): *Effective and Sustainable Hydraulic Fracturing*, 95-121. IntechOpen. doi: 10.5772/56458
- Kervall, H., 2020: Geologiska undersökningar FFC-1. *E.ON rapport*, 20 pp. [in Swedish].
- Klein, C. & Philpotts, A. R., 2012: *Earth materials: introduction to mineralogy and petrology*. Cambridge University Press, 1254 pp.
- Klingspor, I., 1976: Radiometric age-determination of basalts, dolerites and related syenite in Skåne, southern Sweden. *GFF* 98, 195–216
- Klitzsch, N. & Ahrensmeier, C., 2021: Thermal matrix properties measured on cuttings from the Malmö well. RWTH Aachen University. *Unpublished report*.
- Kukkonen, I. T. & Pentti, M., 2021: St1 Deep Heat Project: Geothermal energy to the district heating network in Espoo. 2021 IOP Conference Series: *Earth and Environmental Science*. 703 012035. doi: 10.1088/1755-1315/703/1/012035
- Kukkonen, I. T., Rath, V., Kivekäs, L., Šafanda, J. & Čermak, V., 2011: Geothermal studies of the Outokumpu Deep Drill Hole, Finland: Vertical variation in heat flow and palaeoclimatic implications. *Physics of the Earth and Planetary Interiors* 188, 9-25. doi: 10.1016/j.pepi.2011.06.002
- La Pointe, P., Fox, A., Hermanson, J. & Öhman, J., 2008: Geological discrete fracture network model for the Laxemar site—site descriptive modelling SDM-Site Laxemar. *Svensk kärnbränslehantering AB Report R-08-55*, 260 pp.
- Labus, M. & Labus, K., 2018: Thermal conductivity and diffusivity of fine-grained sedimentary rocks. *Journal of Thermal Analysis and Calorimetry* 132, 1669-1676. doi: 10.1007/s10973-018-7090-5
- Landström, O., Larson, S. A., Lind, G. & Malmqvist, D., 1980: Geothermal investigations in the Bohus Granite area in southwestern Sweden. *Tectonophysics* 64, 131-162.
- Lundegårdh, P., H., 1963: Projektering av rum och tunnlar i berg. *Sveriges geologiska undersökning Rapport 76* pp. [in Swedish].
- Majorowicz, J., Chan, J., Crowell, J., Gosnold, W., Heaman, L. M., Kück, J., Nieuwenhuis, G., Schmitt, D. R., Unsworth, M., Walsh, N. & Weides, S., 2014: The first deep heat flow determination in crystalline basement rocks beneath the Western Canadian Sedimentary Basin. *Geophysical Journal International* 197, 731-747. doi: 10.1093/gji/ggu065
- Malehmir, A., Bergman, B., Andersson, B., Sturk, R. & Johansson, M., 2018: Seismic imaging of dyke swarms within the Sorgenfrei–Tornquist Zone (Sweden) and implications for thermal energy storage. *Solid Earth* 9, 1469-1485. doi: 10.5194/se-9-1469-2018
- MEET Multi-sites EGS Demonstrations, 2020: Deliverable D3.2. 1D/2D DFN models of borehole fractures and hydraulic circulation simulations, 27 pp.
- Massachusetts Institute of Technology, 2006: *The Future of Geothermal Energy -Impact of Enhanced Geothermal Systems (EGS) on the United States in the 21st Century: An Assessment*. Massachusetts Institute of Technology, 372 pp.
- Mitra, G., 1978: Ductile deformation zones and mylonites; the mechanical processes involved in the deformation of crystalline basement rocks. *American Journal of Science American Journal of Science* 278, 1057-1084.
- Mogensen, T. E., & Korstgård, J. A., 2003: Triassic and Jurassic transtension along part of the Sorgenfrei-Tornquist Zone in the Danish Kattegat. In: *The Jurassic of Denmark and Greenland* (Ed. by J. Ineson & F. Surlyk), Geol. Surv. Denm. Greenl. Bull. 1. 439–458.
- Möller, C., Andersson, J., Lundqvist, I. & Hellström, F., 2007: Linking deformation, migmatite formation and zircon U-Pb geochronology in polymetamorphic orthogneisses, Sveconorwegian Province, Sweden. *Journal of Metamorphic Geology* 25, 727-750. doi: 10.1111/j.1525-1314.2007.00726.x
- Nordén, M., Toverud, Ö., Wallberg, P., Strömberg, B., Wiebert, A., Dverstorp, B., Kautsky, F., Simic, E. & Xu, S., 2008: Myndigheternas granskning av SKB:s preliminära säkerhetsbedömningar för Forsmark och Laxemar. *Statens Kärnkraftsinspektion Rapport 2008:03*, 32 pp. [in Swedish].
- Pan, M., Sjöberg, L. E. & Talbot, C. J., 2001: Crustal movements in Skåne, Sweden, between 1992 and 1998 as observed by GPS: *Journal of Geodynamics* 31, 311-322.
- Persson, K., Johansson, R., Mellqvist, C. & Bergman, T., 2014: Beskrivning till berggrundskartan Sundsvall–Timrå–Härnösand. *Sveriges geologiska undersökning K456*, 28 pp. [in Swedish].
- Persson, L. & Göransson, M., 2010: *Beskrivning till bergkvalitetskartan Romeleåsen. Sveriges geologiska undersökning K229*, Uppsala. 28 pp. [in Swedish].
- Pfalzwerke, 2019: *Insheim*. Retrieved 2021-06-21, from <https://www.geothermie-insheim.de/index.php/das-kraftwerk>.
- Popov, Y. A., Pribnow, D. F. C., Sass, J. H., Williams, C. F. & Burkhardt, H., 1999: Characterization of rock thermal conductivity by high-resolution optical scanning. *Geothermics* 28, 253-276. doi: 10.1016/S0375-6505(99)00007-3
- Potter, R., Robinson, E. & Smith, M., 1974: Method of extracting heat from dry geothermal reservoirs. *Report Number: US 3786858*, Google Patents, United States, 6 pp.
- Robertson, E. C., 1988: Thermal properties of rocks. *Open-File Report 88-441*, U.S. Geological Survey, Virginia, United States, 110 pp.
- Rosberg, J.-E. & Erlström, M., 2019: Evaluation of the Lund deep geothermal exploration project in the Romeleåsen Fault Zone, South Sweden: a case study. *Geothermal Energy* 7, 1-30. doi: org/10.1186/s40517-019-0126-7
- Rosberg, J.-E. & Erlström, M., 2021: Evaluation of

- Deep Geothermal Exploration Drillings in the Crystalline Basement of the Fennoscandian Shield Border Zone in South Sweden. *Geothermal Energy* 9, 1-25, doi: 10.21203/rs.3.rs-579919/v1
- Russ, J. C., 1984: Energy Dispersive Spectrometers. In *Fundamentals of Energy Dispersive X-ray Analysis*, 17-41. Butterworth-Heinemann.
- Rämö, O. T., Lehtinen, M. & Nurmi, P., A., 2005: *Precambrian Geology of Finland: Key to the Evolution of the Fennoscandian Shield (Developments in Precambrian geology, 0166-2635; 14)*. Elsevier Science Limited.
- Sivhed, U., Wikman, H. & Erlström, M., 1999: Beskrivning till berggrundskartorna 1C Trelleborg NV och NO samt 2C Malmö SV, SO, NV och NO. *Sveriges geologiska undersökning 191-194, 196, 198*, 148 pp. [in Swedish].
- Svensk Kärnbränslehantering AB, 2009-a: Berättelsen om Forsmark. *Svensk kärnbränslehantering AB. Rapport*, 116 pp. [in Swedish].
- Svensk Kärnbränslehantering AB, 2009-b: Site description of Forsmark at completion of the site investigation phase: SDM-Site Forsmark. *Svensk kärnbränslehantering AB. Technical Report TR-08-05*, Stockholm, 545 pp.
- Svensk Kärnbränslehantering AB, 2009-c: Site description of Laxemar at completion of the site investigation phase SDM-Site Laxemar. *Svensk kärnbränslehantering AB. Technical Report TR-09-01*, Bromma, 637 pp.
- Sveriges geologiska undersökning, 2016: Normbrunn-16 Vägledning för att borra brunn. Rapport, 34 pp. [in Swedish].
- Sorkhabi, R., 2014: Fracture, Fracture Everywhere Part I. *Geoexpo Vol. 11, No. 3*, 103pp. 86-88
- Statens Offentliga Utredningar, 2020: Vägen till en klimatpositiv framtid. Statens Offentliga Utredningar, *Rapport 2020:4*, Stockholm, 850 pp. [in Swedish].
- Stephens, M. B. & Wahlgren, C.-H., 2020: Polyphase (1.91.8, 1.51.4 and 1.00.9 Ga) deformation and metamorphism of Proterozoic (1.91.2 Ga) continental crust, Eastern Segment, Sveconorwegian orogen. In M. B. Stephens, & J. Bergman Wehded, (eds.): *Sweden Lithotectonic Framework, Tectonic Evolution and Mineral Resources*, 351-396. Geological Society of London, London, Memoirs 50.
- Sundberg, J., Back, P.-E., Ländell, M. & Sundberg, A., 2009: *Modelling of temperature in deep boreholes and evaluation of geothermal heat flow at Forsmark and Laxemar. Svensk kärnbränslehantering AB. Report SKB-TR-09-14*, 87 pp.
- Sundberg, J., 1991: *Termiska egenskaper i jord och berg*. Statens geotekniska institut (SGI), Linköping, 32 pp. [in Swedish].
- Sydsten AB, n.d.-a: *Historia*. Retrieved 2021-04-28, from <https://www.sydsten.se/om-oss/historia/> [in Swedish].
- Sydsten AB, n.d.-b: *Täkter*. Retrieved 2021-05-01, from <https://www.sydsten.se/har-finns-vi/takter/> [in Swedish].
- Sydsten AB, 2002: Undersökning av bergkvaliteten för vidare brytning för AB Sydstens bergtäkt i Dalby. 2 pp. [in Swedish].
- Söderlund, U. & Ask, R., 2006: Mesoproterozoic bimodal magmatism along the Protogine Zone, S Sweden: three magmatic pulses at 1.56, 1.22 and 1.205 Ga, and regional implications. *GFF* 128, 303-310. doi: org/10.1080/11035890601284303
- Thermophysical Instruments Geothermal Investigation, 2021: Determining the Thermal Conductivity of Fragments and Powder. Retrieved 2021-05-30, from <https://www.te-ka.de/en/testing-services/fragments-and-powder>.
- Thybo, H., 2000: Crustal structure and tectonic evolution of the Tornquist Fan region as revealed by geophysical methods. *Bulletin of the Geological Society of Denmark* 46, 145-160. doi: 10.37570/bgsd-1999-46-12
- Tingay, M., Reinecker, J. & Müller, B., 2008: Borehole breakout and drilling-induced fracture analysis from image logs. World Stress Map Project 2008, 9 pp.
- Tunemar, L., 2006: Grundvatten i berg, metodik för övervakning av vattenkvalitet samt undersökningsresultat 1981 och 2004. *Länsstyrelsen i Stockholms län Rapport*, Stockholm. [in Swedish].
- Ulmius, J., Möller, C., Page, L., Johansson, L. & Ganerød, M., 2018: The eastern boundary of Sveconorwegian reworking in the Baltic Shield, defined by <sup>40</sup>Ar/<sup>39</sup>Ar geochronology across the southernmost Sveconorwegian Province. *Precambrian research* 307, 201-217. doi: 10.1016/j.precamres.2018.01.008
- U.S. Department of Energy, 2016: What is an Enhanced Geothermal System (EGS)? In: U. S. Department of Energy (ed.), *Geothermal technology office*. 2 pp.
- U.S. Department of Energy, n.d.-a: *Geothermal basics*. Retrieved 2021-05-24, from <https://www.energy.gov/eere/geothermal/geothermal-basics>
- U.S. Department of Energy, n.d.-b: *What is FORGE?* Retrieved 2021-06-22, from <https://www.energy.gov/eere/geothermal/what-forge>
- Van Der Pluijm, B. A. & Marshak, S., 2004: *Earth structure: an introduction to structural geology and tectonics*. W.W. Norton, 673 pp.
- Vattenfall, 2020: *How we will phase out our carbon dioxide emissions*. Retrieved 2021-05-25, from <https://group.vattenfall.com/press-and-media/newsroom/2020/how-we-will-phase-out-our-carbon-dioxide-emissions>.
- Wallroth, T., 1994: Geotermisk energiutvinning ur kristallint berg, hot dry rock. Geologiska Institutionen Rapport 1993/94, Göteborg, 73 pp. [in Swedish].
- White, S. H., Burrows, S. E., Carreras, J., Shaw, N. D. & Humphreys, F. J., 1980: On mylonites in ductile shear zones. *Journal of Structural Geology* 2, 175-187.
- Wiersberg, T., Pierdominici, S., Lorenz, H., Almqvist,

- B. & Klonowska, I., 2020: Identification of gas inflow zones in the COSC-1 borehole (Jämtland, central Sweden) by drilling mud gas monitoring, downhole geophysical logging and drill core analysis. *Applied Geochemistry* 114, 104513. doi: org/10.1016/j.apgeochem.2019.104513
- Wikman, H., Bergström, J., Sivhed, U., 1993: Beskrivning till berggrundskartan Helsingborg SO, *Sveviges geologiska undersökning Af 180*, 114 pp. [in Swedish with an English summary].
- Winter, J. D., 2014: *Principles of Igneous and Metamorphic Petrology: Pearson New International Edition*. Pearson Education, Inc.
- Wirtén, L., 2020: Spänningstrailern ger säkra analyser. *Svensk Geoenergi* 2, 10. [in Swedish].
- Wirtén, L., 2016: Lund får värme från djupet. *Svensk Geoenergi* 1, 16–17. [in Swedish].
- World Stress Map, 2020: *Stress Indicators in the WSM Database*. Retrieved 29-04-2020, from <http://www.world-stress-map.org/data/>.
- Zang, A., Stephansson, O., Heidbach, O., Janouschko-wetz, S., 2012: World Stress Map Database as a Resource for Rock Mechanics and Rock Engineering. *Geotechnical and Applied Geological Engineering* 30, 625-646.
- Zhang, R.-H., Wang, K., Zeng, Q.-L., Yu, C.-F. & Wang, J.-P., 2021: Effectiveness and petroleum geological significance of tectonic fractures in the ultra-deep zone of the Kuqa foreland thrust belt: a case study of the Cretaceous Bashijiqi Formation in the Keshen gas field. *Petroleum Science* 18, 728-741. doi: 10.1007/s12182-021-00567-w
- Zimmermann, G., Korner, A. & Burkhardt, H., 2000: Hydraulic pathways in the crystalline rock of the KTB. *Geophysical Journal International* 142, 4-14.
- Zoback, M. L., 1992: In Situ Stress, causes and nature of in situ stress. First- and second-order patterns of stress in the lithosphere: The World Stress Map Project. *Journal of Geophysical Research* 97, 11703 pp.



**Tidigare skrifter i serien  
”Examensarbeten i Geologi vid Lunds  
universitet”:**

576. Gustafsson, Jon, 2019: Petrology of platinum-group element mineralization in the Koillismaa intrusion, Finland. (45 hp)
577. Wahlquist, Per, 2019: Undersökning av mindre förkastningar för vattenuttag i sedimentärt berg kring Kingelstad och Tjutebro. (15 hp)
578. Gaitan Valencia, Camilo Esteban, 2019: Unravelling the timing and distribution of Paleoproterozoic dyke swarms in the eastern Kaapvaal Craton, South Africa. (45 hp)
579. Eggert, David, 2019: Using Very-Low-Frequency Electromagnetics (VLF-EM) for geophysical exploration at the Albertine Graben, Uganda - A new CAD approach for 3D data blending. (45 hp)
580. Plan, Anders, 2020: Resolving temporal links between the Högberget granite and the Wigström tungsten skarn deposit in Bergslagen (Sweden) using trace elements and U-Pb LA-ICPMS on complex zircons. (45 hp)
581. Pilser, Hannes, 2020: A geophysical survey in the Chocaya Basin in the central Valley of Cochabamba, Bolivia, using ERT and TEM. (45 hp)
582. Leopardi, Dino, 2020: Temporal and genetical constraints of the Cu-Co Vena-Dampetorp deposit, Bergslagen, Sweden. (45 hp)
583. Lagerstam Lorien, Clarence, 2020: Neck mobility versus mode of locomotion – in what way did neck length affect swimming performance among Mesozoic plesiosaurs (Reptilia, Sauropterygia)? (45 hp)
584. Davies, James, 2020: Geochronology of gneisses adjacent to the Mylonite Zone in southwestern Sweden: evidence of a tectonic window? (45 hp)
585. Foyn, Alex, 2020: Foreland evolution of Blåisen, Norway, over the course of an ablation season. (45 hp)
586. van Wees, Roos, 2020: Combining luminescence dating and sedimentary analysis to derive the landscape dynamics of the Velická Valley in the High Tatra Mountains, Slovakia. (45 hp)
587. Rettig, Lukas, 2020: Implications of a rapidly thinning ice-margin for annual moraine formation at Gornergletscher, Switzerland. (45 hp)
588. Bejarano Arias, Ingrid, 2020: Determination of depositional environment and luminescence dating of Pleistocene deposits in the Biely Váh valley, southern foothills of the Tatra Mountains, Slovakia. (45 hp)
589. Olla, Daniel, 2020: Petrografisk beskrivning av Prekambriska ortognejser i den undre delen av Särsvskollan, mellersta delen av Skollenheten, Kaledonska orogenen. (15 hp)
590. Friberg, Nils, 2020: Är den sydatlantiska magnetiska anomalin ett återkommande fenomen? (15 hp)
591. Brakebusch, Linus, 2020: Klimat och väder i Nordatlanten-regionen under det senaste årtusendet. (15 hp)
592. Boestam, Max, 2020: Stränder med erosion och ackumulation längs kuststräckan Trelleborg - Abbekås under perioden 2007-2018. (15 hp)
593. Agudelo Motta, Laura Catalina, 2020: Methods for rockfall risk assessment and estimation of runout zones: A case study in Gothenburg, SW Sweden. (45 hp)
594. Johansson, Jonna, 2020: Potentiella nedslagskratrar i Sverige med fokus på Östersjön och östkusten. (15 hp)
595. Haag, Vendela, 2020: Studying magmatic systems through chemical analyses on clinopyroxene - a look into the history of the Teno ankaramites, Tenerife. (45 hp)
596. Kryffin, Isidora, 2020: Kan benceller bevaras över miljontals år? (15 hp)
597. Halvarsson, Ellinor, 2020: Sökande efter nedslagskratrar i Sverige, med fokus på avtryck i berggrunden. (15 hp)
598. Jirdén, Elin, 2020: Kustprocesser i Arktis – med en fallstudie på Prins Karls Forland, Svalbard. (15 hp)
599. Chonewicz, Julia, 2020: The Eemian Baltic Sea hydrography and paleoenvironment based on foraminiferal geochemistry. (45 hp)
600. Paradeisis-Stathis, Savvas, 2020: Holocene lake-level changes in the Siljan Lake District – Towards validation of von Post's drainage scenario. (45 hp)
601. Johansson, Adam, 2020: Groundwater flow modelling to address hydrogeological response of a contaminated site to remediation measures at Hjortsberga, southern Sweden. (15 hp)
602. Barrett, Aodhan, 2020: Major and trace element geochemical analysis of norites in the Hakefjorden Complex to constrain magma source and magma plumbing systems. (45 hp)
603. Lundqvist, Jennie, 2020: ”Man fyller det med information helt enkelt”: en fenomenografisk studie om studenters upplevelse av geologisk tid. (45 hp)
604. Zachén, Gabriel, 2020: Classification of four mesosiderites and implications for their formation. (45 hp)
605. Viðarsdóttir, Halla Margrét, 2020: Assessing the biodiversity crisis within the

- Triassic-Jurassic boundary interval using redox sensitive trace metals and stable carbon isotope geochemistry. (45 hp)
606. Tan, Brian, 2020: Nordvästra Skånes prekambriiska geologiska utveckling. (15 hp)
607. Taxopoulou, Maria Eleni, 2020: Metamorphic micro-textures and mineral assemblages in orthogneisses in NW Skåne – how do they correlate with technical properties? (45 hp)
608. Damber, Maja, 2020: A palaeoecological study of the establishment of beech forest in Söderåsen National Park, southern Sweden. (45 hp)
609. Karastergios, Stylianos, 2020: Characterization of mineral parageneses and metamorphic textures in eclogite- to high-pressure granulite-facies marble at Allmenningen, Roan, western Norway. (45 hp)
610. Lindberg Skutsjö, Love, 2021: Geologiska och hydrogeologiska tolkningar av SkyTEM-data från Vombsänkan, Sjöbo kommun, Skåne. (15 hp)
611. Hertzman, Hanna, 2021: Odensjön - A new varved lake sediment record from southern Sweden. (45 hp)
612. Molin, Emmy, 2021: Rare terrestrial vertebrate remains from the Pliensbachian (Lower Jurassic) Hasle Formation on the Island of Bornholm, Denmark. (45 hp)
613. Højbert, Karl, 2021: Dendrokronologi - en nyckelmetod för att förstå klimat- och miljöförändringar i Jämtland under holoцен. (15 hp)
614. Lundgren Sassner, Lykke, 2021: A Method for Evaluating and Mapping Terrestrial Deposition and Preservation Potential for Palaeostorm Surge Traces. Remote Mapping of the Coast of Scania, Blekinge and Halland, in Southern Sweden, with a Field Study at Dalköpinge Ängar, Trelleborg. (45 hp)
615. Granbom, Johanna, 2021: En detaljerad undersökning av den mellanordoviciska "furudalkalkstenen" i Dalarna. (15 hp)
616. Greiff, Johannes, 2021: Oolites from the Arabian platform: Archives for the aftermath of the end-Triassic mass extinction. (45 hp)
617. Ekström, Christian, 2021: Rödfärgade utfällningar i dammanläggningar orsakade av *G. ferruginea* och *L. ochracea* - Problemstatistik och mikrobiella levnadsförutsättningar. (15 hp)
618. Östsjö, Martina, 2021: Geologins betydelse i samhället och ett första steg mot en geopark på Gotland. (15 hp)
619. Westberg, Märta, 2021: The preservation of cells in biomineralized vertebrate tissues of Mesozoic age – examples from a Cretaceous mosasaur (Reptilia, Mosasauridae). (45 hp)
620. Gleisner, Lovisa, 2021: En detaljerad undersökning av kalkstenslager i den mellanordoviciska gullhögenformationen på Billingen i Västergötland. (15 hp)
621. Bonnevier Wallstedt, Ida, 2021: Origin and early evolution of isopods - exploring morphology, ecology and systematics. (15 hp)
622. Selezeneva, Natalia, 2021: Indications for solar storms during the Last Glacial Maximum in the NGRIP ice core. (45 hp)
623. Bakker, Aron, 2021: Geological characterisation of geophysical lineaments as part of the expanded site descriptive model around the planned repository site for high-level nuclear waste, Forsmark, Sweden. (45 hp)
624. Sundberg, Oskar, 2021: Jordlagerföljden i Højeådal utifrån nya borrhningar. (15 hp)
625. Sartell, Anna, 2021: The igneous complex of Ekmanfjorden, Svalbard: an integrated field, petrological and geochemical study. (45 hp)
626. Juliusson, Oscar, 2021: Implications of ice-bedrock dynamics at Ullstorp, Scania, southern Sweden. (45 hp)
627. Eng, Simon, 2021: Rödslam i svenska kraftdammar - Problematik och potentiella lösningar. (15 hp)
628. Kervall, Hanna, 2021: Feasibility of Enhanced Geothermal Systems in the Precambrian crystalline basement in SW Scania, Sweden. (45 hp)



# LUNDS UNIVERSITET

Geologiska institutionen  
Lunds universitet  
Sölvegatan 12, 223 62 Lund